Uncovering the Mechanical Properties of *Drosophila's* Wing Disc

---

Dissertation

zur

Erlangung der naturwissenschaftlichen Doktorwürde (Dr. sc. nat.)

vorgelegt der

Mathematisch-naturwissenschaftlichen Fakultät

der

Universität Zürich

von

FLAVIO LANFRANCONI

von

WINTERTHUR ZH

Promotionskommission:

Prof. Dr. Christof Aegerter (Vorsitz und Leitung)

Prof. Dr. Damian Brunner

Dr. Richard Smith

Zürich, 2017

Acknowledgements

First I would like to express my gratitude towards my supervisor, Christof Aegerter, for the possibility to undertake this explorative journey of scientific uncovering in his research group. The freedom to change the mode of inquiry when curiosity demands and possibilities exist was greatly appreciated. Likewise, the not-this-common possibility to work part-time, which allowed me to start and enjoy a family in parallel to this intriguing work, evokes a feeling of great content.
I also thank my kind committee members, Damian Brunner and Richard Smith for the pleasant collaboration.
I am in debt to Dominik Eder and Amarendra Badugu for explaining a lot of the biology and answering all my questions about *Drosophila*, as well as providing me with stocks, fly-food, Wing Medium and many more things.
I would like to thank Sahil, Francesco, Arne, Mirco, Archana, Paule, Jale, David, Lara, Severine, as well as, Ulrike, Giulia and Daniel for having been a wonderful research group even if I couldn't join all the social gatherings, I very much enjoyed being part of this group.
A special thanks goes to Sahil and to Cédric for the many hours of interesting and stimulating discussions and for the correction of this report.

Also I will include some words of gratefulness for Masa's continuous support and supervision concerning the Shin Aiki training I was partially trusted with during the same period of time. His unshatterable belief in ceaseless development, especially in the face of problems, led me to find strength to always keep going. I owe a lot to his teachings.
I would also like to include Claude, Glenn, Dinah, Karl, Werner, Cornelia, Joachim, Basil, Neil and Sibylle in my acknowledgments, since they have been very reliable training partners that allowed me to grow as a trainer and as human. My deep affection also goes out to Willi whom unfortunately I can not thank in person anymore for the recognition he gave me.

By far my biggest thanks go to my amazing wife, Angela who made this whole endeavor possible by being always by my side and enabling me to fulfill my ambitions. I thank my lovely daughter Enya who is basically as old as this thesis and my precious son, Nio, who accompanied in his arrival the closure of this work.
I am deeply grateful for the love and trust from my parents, Aldo and Edith, and the confidence of my dear sisters Lucia and Romana.

The three pillars of science, budo and family have proven to provide a stable balance, also in some demanding times. I am deeply honored to be in the place I am today.

Abstract

The aim of this thesis is the characterization of the mechanical properties of the wing imaginal disc of the fruit fly *Drosophila melanogaster* late third instar larvae.
These properties should be formulated in terms of a rheological model that gives a descriptive account of the time-dependent force-displacement characteristic of the wing disc under external load.
The wing imaginal disc, or wing disc for short, is a model system for embryonic tissues, wherein cells have to make complex decisions on growth and cell-division which will heavily impact size and shape of the adult. To answer the open question of how the cells are collectively able to orchestrate these decisions, it has been proposed that feedback of mechanical stress is used as a regulator. However, while strain, even in tissues in-vivo, can be measured by imaging, stress can not. Therefore most models simply assume a linear (Hookean) elasticity of the tissue.
This assumption can be tested experimentally by measuring the force-displacement behavior of the tissue as a whole. This is what the objective of the here presented work will be.
In addition, the time dependence of this behavior is usually completely ignored, but shall also be determined in the course of this work.

Zusammenfassung

Das Ziel dieser Dissertation ist die Charakterisierung der Materialeigenschaften der Flügelimaginalscheibe von *Drosophila melanogaster* im späten dritten Larvenstadium.
Diese Eigeschaften sollen in Bezug auf ein rheologisches Model formuliert werden, welches eine deskriptive Beschreibung der zeitlich veränderlichen Kraft-Verlängerungs Charakteristik der Flügelscheibe unter äusserlicher Kraftanwendung gibt.
Die Flügelimaginalscheibe, oder kurz, die Flügelscheibe, ist ein Modelsystem für embrionales Gewebe, in denen Zellen komplexe Entscheidungen bezüglich Wachstum und Zeillteilung fällen müssen, die die Form und Grösse des adulten Tieres massgeblich bestimmen. Um die offene Frage, wie die Zellen fähig sind diese Entscheidungen im Kollektiv zu orchestrieren, zu beantworten, wurde vorgeschlagen, dass sie Feedback von mechanischer Spannung zur Regulierung nutzen. Jedoch kann Dehnung, sogar *in vivo*, durch Abbilden gemessen werden, Spannung aber nicht. Deswegen nehmen die meisten Modelle einfach eine lineare (Hooksche) Elastizität des Gewebes an.
Diese Annahme kann jedoch experimentell getestet werden indem das Kraft-Verlängerungs Verhalten des Gewebes als Ganzes gemessen wird. Dies wird die Zielsezung dieser Arbeit sein.
Das zeitliche Verhalten dieser Eigenschaften wird normalerweise komplett vernachlässigt. Es soll im Laufe dieser Arbeit aber ebenfalls bestimmt werden.

Outline

This thesis will be split into nine sections, organized into three main parts.

I: Section 1 will introduce the problems faced by biologists working on morphogenesis and the used model-system: the wing disc.
Section 3 will present the language of rheology and its constituent parts.
And Section 2 will critically review some of the work that has been done in the context of forces in developing tissue.

II: Section 4 will present the structural principle of "tensegrity" and my initial work on implementing it into a "3-d vertex-model".
Section 5 constitutes the main body of this work, describing in detail the experimental set-up that was built.
And Section 6 will discuss the different measurements made with the set-up.

III: Section 7 will present the mechanical model that was constructed to describe the time-dependent force-displacement behavior of the wing imaginal disc.
Section 8 will summarize the work.
And Section 9 will give an outlook how the presented findings could contribute further work.

Contents

Part I.

1. Introduction: Biology and Mechanical Forces

It is an old but prevailing open question in developmental biology how the process of morphogenesis, the appearance of form, is happening.
In this section I will first introduce what morphogenesis is and how the appearance of what we call "living" compared to "non-living" forms differ. Next I will briefly talk about the history of the subject, followed by a short remark about the ontological status of forces.
In Section 1.1 I will introduce the object under investigation: the wing imaginal disc of the *Drosophila melanogaster* late third instar larva, subsequently called the wing disc.

Morphogenesis

In structures of "non-living materials", see Figure 1.1 for examples, the question of morphogenesis is often solved by locating one source of external physical force or a relevant internal force-organization. To explain the shape of crystals or snowflakes, for example, one looks at the spatial orientation of the atomic or molecular bonds. To understand why pebbles are smooth, valleys come in distinct forms (v- or u- shaped...) or sandstone rock formations can take on their impressive shapes the one concept of erosion is needed. A fluid, such as water, a glacier or wind, continuously removes material from the structure in question. In the case of sandstone formations additionally to this external cause of morphogenesis one needs to understand the internal packing of sand by force chains in the granular material, making it less prone to erosion along those chains, to get a complete picture. Yet another form of morphogenetic process is at work in forming mountains, here the inertia of the moving tectonic plates is the driving force for the plastic deformation of the ground.

(a) (b) (c)

Figure 1.1: Examples of "non-living" forms, shaped by different morphogenetic processes.

While the full understanding of these processes is undoubtedly highly non-trivial and many of these are still under active scientific investigation, the problem becomes obviously vastly more complex in the "living" realm.

(a) (b) (c) (d) (e)

Figure 1.2: To understand the morphogenesis in the diverse multitude of living things becomes a vastly more complicated task.

So while they are undoubtedly bound by the same fundamental laws of nature, there are a few quite distinctive differences between the morphogenesis of forms we call "alive" and such we do not.
For one: No single cause for a final shape is expected to suffice as an explanation for its emergence since also the external as well as the internal environment is constantly changing during the development of the form in question.
Second: While all forms of life pass through an often quasi spherical symmetrical single celled stage, built by their mother (and often some addition by a father) they then proceed to "grow by themselves". There is a breaking of the spherical symmetry, that seems to happen on its own. Polarity and body parts seem to appear out of nowhere, not shaped by an apparent external agent.
Thirdly: There are flows of matter and flows of entropy through the organism, from outside to inside and vice-versa. Obviously, complex chemical processes are constantly active within.
These differences lead to a fourth fundamental difference between the explanation for the shape of living versus non-living entities: While in the non-living there is not much debate about the questions of: "What is meant by "explaining" the appearance of the form?" There seems to be quite clear consensus: An explanation for a shape lies in a list of the forces that produced it.
For organisms the answer still depends strongly on who you ask and basically includes all four Aristotelian causes: *causa materialis*, or a list of the material that is involved and how this material interacts in the body in question (molecular life sciences), *causa finalis*, *causa formalis*, or the twofold aspect of what form serves which purpose and the assertion of the reciprocal causation of the two (evolutionary developmental biology, "evo-devo") as well as, as was the case in the "non-living", the *causa efficiens*, or the location of the moving agent(s) that formed the body (biophysics)[1].
In my own eyes the question clearly begs for an answer in all four aspects, and should not be considered solvable by any one of the above mentioned fields, or mindsets.
Still the work presented here focuses exclusively on the interplay between the *causa efficiens* and the *causa materialis*, or how the material of the body in question reacts to external perturbation by the agent of mechanical pull. It does not, therefore, directly contribute to a answer to the question of morphogenesis, but hopes to lay groundwork for future interdisciplinary research in the field by providing a bridging element between the material aspect and the search for causing agents.

In conclusion, what I believe can be clearly stated, regardless of mindset, is: when looking at the morphogenesis of living things as opposed to non-living things, the focus has to shift from primarily locating a source of physical force acting on the object to talking about mechanisms at work during the formation of the subject, and trying to locate lawful behavior within them.

[1] This coarse and somewhat flippant allocation of huge and broad fields of science is not meant to be irrevocable. Rather the intent of it is to provoke perspective and to question personal predispositions of the reader.

So next let us look at the history of the search for such lawful behavior for morphogenesis in biology and what this has taught us about the difference between "living" and "non-living".

History

D'Arcy Thompson is often cited as the first to systematically address the shaping of biological entities and to try and locate the physical forces necessary for the emergence of their form. He published a book "on growth and form" [1] in 1917 and expanded it in a second edition, published in 1942. The question was investigated by philosophers and scholars before that time but his work remains as a corner stone for the field because of his mathematical and systematic approach. Notably his work focused heavily on correlations between biological forms and mechanical phenomena (*causa efficiens*) and was situated as an opposition to natural selection as the driving force for the appearance of form of living things.[2]

However, as noted above, the processes at work are also of chemical nature and a lot of work was needed to understand the chemical basis for life. And especially after the discovery of the structure of DNA in 1953 [3], the hope grew strong that a broader understanding of the molecular structures and their interplay and dynamics would explain all peculiarities of living things. And so the field shifted further towards pure materialism, into the examination of the molecules of life.

But while biochemistry and gene regulation considerations can give a detailed descriptive analysis of development, they do not touch upon the explanatory aspect of mechanisms and general principles, which in turn would also yield deterministic power.

An example[2]: Big animals have big bones. But also their bones are thicker than just a scaled up version of the same bone of a smaller animal. Now a fairly simple scaling argument, made already by Galileo Galilei in 1638 [5] shows that this is a necessity in order for the bones to withstand the increased load of heavier animals if one assumes a constant yield stress σ_Y for bone: Load is proportional to weight, which is proportional to volume l^3. And the strength of a bone is proportional to its cross sectional area d^2 times the yield stress σ_Y. Therefore to sustain the animal:

$$\begin{aligned} l^3 &\propto d^2 \cdot \sigma_Y \\ \Rightarrow d &\propto l^{3/2} \quad . \end{aligned} \tag{1}$$

So larger animals need bones that are thicker than a scaled up version of a similar but smaller animal would be. (King Kong could not have the same proportions as a real gorilla has, his legs would break.)

Now this principle can be used to predict bone thickness for animals.

Later on, at the end of the 19th century, Carl Culmann, working at ETH, developed a graphical approach to statics [6], and Julius Wolff formulated what has become known as Wolff's law: that bone in a healthy person or animal will adapt to the loads under which it is placed [7]. And their work was prominently featured in Thompson's book mentioned at the beginning of this paragraph, showing that also internally bone-mass is added along stress-lines and removed in places under little mechanical load. Essentially showing how the above mentioned principle is also directly applicable in the individual and formulating it into a law.

Since then a lot of work has been done on the meachone regulation of bone growth, especially looking at tennis players, astronauts and people with prolonged bed rest [8], [9], [10]. And it has been shown, that also microscopical bone remodelling correlates linearly with tissue loading

[2] This example was taken from a lecture about Biology for Physicists by Christof Aegerter [4].

[11]. In bone also the cell-type playing the key role in load-dependent bone remodeling has been identified: the osteocytes [12]. And some of the potential molecular players and their signaling pathways have now been suggested as well as how the signal, mechanical loading, gets transmitted from the macroscopic to the microscopic [13].
The point of this examination of the history of understanding bone growth was to highlight on which level lawful behavior in biology needs to be expected.
While the microscopic description is needed to understand the implementation of the law, the law itself is a macroscopic one. And while it is possible to move the ladder down and find implementations of macroscopic phenomena in the microscopic, the reverse is not true. This is due to the symmetries that get broken when moving from the microscopic to the macroscopic where quantitative differences become qualitative. A point famously made in 1972 by P.A. Anderson: "More is different" [14].
This, I believe, captures the essence of what makes living things different from non-living ones: They are (vastly) more complex. They are at the same time the same and completely distinct. By being more of the same, they become profoundly different.
So now that we have looked at the biology part of the introduction, let's have a short look at forces.

Ontology of forces

Nowadays we take it for granted to know what is meant by "a force". A lot of us will probably jump to thoughts about Galilei and his correction to the Aristotelian theory of motion, which allowed Newton to formulate his three laws of motion, when pressed about it. However I find it noteworthy to take a step further back and acknowledge the somewhat mystical nature of the word. It is generally taken to mean "[the] capacity of exercising an influence or producing an effect" [15]. But it is distinct from "the cause": "that which produces or effects a result" [16].
An example will clarify the simple point I intend to make: When considering two billiard balls clashing together, we could call the first ball the cause for the motion of the second. And we can clearly see the balls, measure their masses and velocities and determine that the final speed of the second causally depends on the velocity of the first. [3]
So while we can see cause and effect, the force at work is unseen. It is of completely different ontological status and by its very nature, not directly measurable or observable. It is an abstraction as the interacting agent between cause and effect and can only be inferred from them. Of course the fact that this interaction can take place over large distances, as can be seen with gravitation, makes this construct highly useful.
Credit must be given to Sir Isaac Newton for the precise and adequate formulation of this abstraction $F = m \cdot a$ which then allows us to focus exclusively on the second ball and talk about the force that produced its acceleration.[4]
therefore the abstract concept of a force acting on an object allows one to make meaningful statements about conceptually isolated objects. But it can never be measured directly.
The usual way to deal with this is to take a spring and hang an object of known mass at its end. Since we know the acceleration of gravity on the earth surface g [5], we can infer the force with which the spring is being pulled. By making springs that react with expansions that are nicely

[3] One step further and we find that the total momentum is conserved and part or all of it is transferred from one ball to the other.

[4] At this point care has to be taken how to deal with the fact that in reality there are two balls, which is why we need Newtons third law of equal reaction.

[5] Or we can measure it by letting the object fall and measure the time of flight.

linear proportional to the mass that is been hanged on them we have successfully shifted the problem of measurement from force to expansion and stiffness of the spring using:

$$m \cdot g = F = k \cdot \Delta x \quad . \tag{2}$$

Now this spring with known stiffness k can be used to measure Δx and infer the force with which it has been pulled.
This, of course, becomes more difficult at places where you can not put a spring inside. You need knowledge about the mechanical properties of the medium in which you observe displacements in order to make statements about forces. In tissues, see [17] for a review, the relationship between observed extensions and the forces that produced them are largely unknown. To be able to meaningfully talk about forces acting inside tissues, these mechanical properties need to be uncovered before one can take the next step and ask how these forces influence morphogenesis.
I will review more of what has been done in this field in Section 2.

1.1. The Wing imaginal Disc of *Drosophila melanogaster*

Because of the historical significance of the *Drosophila* as a model organism in genetics as well as many other areas of biology, also developmental processes are often studied in this insect. The ease of culturing and fast life cycle are of course important factors for this. Figure 1.3 shows the different stages of the life cycle. The development time depends strongly on temperature, ranging from ca. 50 days at 12 °C to 7 days at 28 °C, above this temperature development time increases again to 11 days at 30 °C. At 25 °C embryos will hatch from the egg after ca. 24 hours, as 1st instar larvae. These will feed for one day before molting into 2nd instar, which will molt again after one day of feeding. The larvae will then continue to feed as 3rd instar larvae for 2 to 3 days at which time they will begin to wander out of the food ("wandering stage") to search for a place for metamorphosis, which takes place over a period of about four days inside the pupa. The pupa has a characteristic opaque, brown color and the transition phase from larva to pupa is called prepupa. After the adult fly emerge from the pupa they take one more day before they become fertile for sexual reproduction and continue to live for about 70 days [18][19][20].

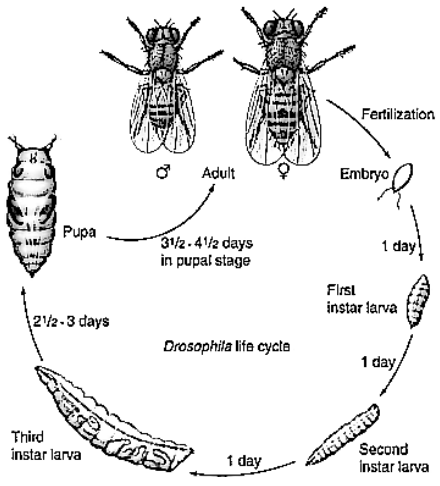

Figure 1.3: Life cycle of *Drosophila melanogaster*, completion of the cycle takes on the order of one week, with a strong temperature dependence [21].

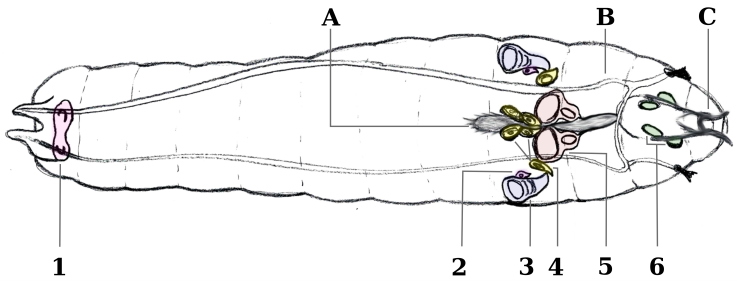

Figure 1.4: Larval structures: **A**: Brain, **B**: Trachea and **C**: Feeding hooks.
Imaginal discs: **1**: Genitalia, **2**: Haltere discs, **3**: Wing discs, **4**: Three pairs of leg discs, **5**: Eye- and antenna discs and **6**: Mouth parts.

In *Drosophila*, it is especially the wing imaginal disc that received a lot of attention for studying the appearance of definite size and form. Figure 1.4 shows the outline of a larva of *Drosophila melanogaster* with all its imaginal discs. As can be seen, the wing discs are fairly easily distinguishable from the other discs exactly by their size and form.
The imaginal discs are the precursors for the organs of the adult fly, so called proto-organs. They grow during larval development and stop their growth before pupation. During metamorphosis there is extensional remodeling, but no further cell divisions.
When artificially changing cell division rates in the wing disc, cell sizes change accordingly, with growth arrest at the appropriate time, leaving the global tissue unchanged in size. So the regulatory mechanisms that control organ size seem to act on tissue level rather than at cell level [22] [23] [24] [17]. The investigation of what these mechanisms are and how they work is the primary context for this thesis and some important work that has been done in this regard will be highlighted in Section 2.
The wing disc itself is mostly studied at or near the end of its completion, in the late third instar larvae in the wandering stage. This has multiple reasons. One, when studying growth arrest, this is of course the time it occurs. Second, here the disc reached its full form. But also it should not be underestimated that the disc starts as a sac of only 20-30 cells, measuring on the order of 10 µm by 10 µm by 10 µm in the newly hatched larva. Over the course of the four days of larval development cells multiply about a 2000-fold ending up with 30 - 50'000 cells [25].
During development the cells shrink in volume and organize into a distinct folded monolayer of epithelial tissue. Figure 1.5(a) shows a cartoon cross section of the epithelial organization, while Figure 1.5(b) shows a slightly more realistic drawing of the shape of the cells based on [26] and [27]. Topologically speaking they are still forming a closed sac, with extracellular matrix (ECM) on the outside and liquid in the inside. The inside is called the lumen. Cells in the top layer, the peripodial membrane (PM), are extremely thin and flat while the ones in the lower layer, the disc proper, are narrow and long. The side of the cells which faces the ECM is called the basal side and the side which faces the lumen is called the apical side. On this side the cells have an actin-enhanced region, called the actin ring, which gives mechanical stability to the cells on this side. Cells are anchored in the ECM with focal adhesion proteins and to each other via cadherin proteins which connect the actin rings on the apical side with one another to a actual actin network. Just below the actin ring sit lateral domain proteins (LDP) [6].

[6] These lateral domain proteins and proteins in the ECM were fluorescently labeled for confocal imaging, see Section 5.3.

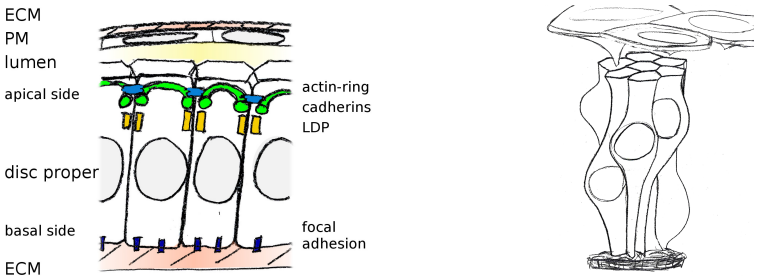

(a) (b)

Figure 1.5: The epithelial organization in the wing disc with: extracellular matrix (ECM), peripodial membrane (PM), disc proper, showing the actin ring, cadherin proteins, lateral domain proteins (LDP) and focal adhesion proteins. (a) shows a schematic of the situation and (b) a slightly more realistic drawing, based on [26] and [27].

Finally Figure 1.6 shows the wing disc itself. [7] Figure 1.6(a) shows a top view of a right wing disc, where three areas are clearly distinguishable. They are called: the wing pouch, the hinge- and the notum region. Figure 1.6(b) shows a cross sectional view, highlighting the same regions in the disc proper and where one can see strong curvature of the pouch and deep folds in the hinge region. Additionally the region below the notum is indicated. This is where muscle cells migrate into a 3-d mesh of ECM and is sometimes not considered to be part of the wing disc, but experimentally it is inseparable from it. The final size of the wing disc is approximately $500\,\mu m \times 300\,\mu m \times 100\,\mu m$. During metamorphosis the wing pouch will elongate upwards and form the two cell-layer thick wing. All the folds around it in the hinge region will constrict and form the hinge of the wing, while the notum region will integrate into the back body wall, see Figure 1.7 [27].

It is imperative for the organism that growth arrest happens at this precise size and form, since it defines size and form of the adult wing. If there is any deviation, this could have drastic effects on the flying capabilities and therefore Darwinian fitness of the organism.

[7] These drawings are based on many observed discs and it is believed that they are more accurate than most representations found in the literature.

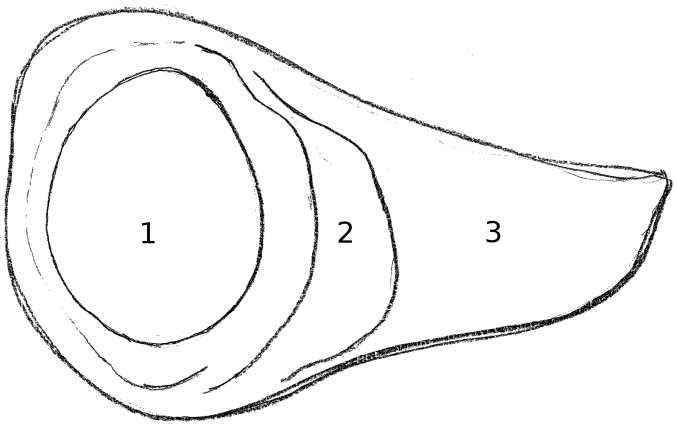

(a)

(b)

Figure 1.6: The right wing disc of a late third instar larva.
Dimensions ca. 500 µm × 300 µm × 100 µm.
1: Wing pouch, **2**: Hinge region, **3**: Notum region and **4**: ECM mesh, populated with muscle cells.

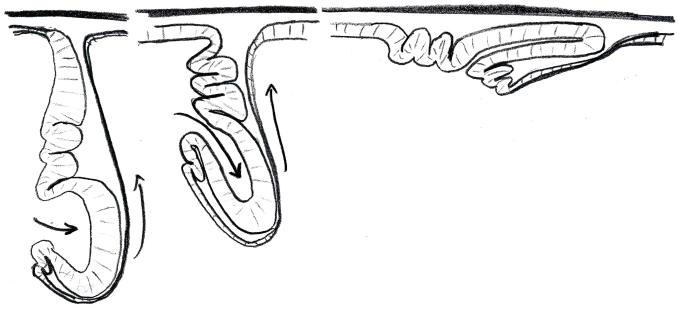

Figure 1.7: Wing disc eversion, happening during metamorphosis. Drawing after [27]

2. Context: Forces and Morphogenesis in the wing disc

As explained in the introduction, while this work purely concerns itself with the wing disc as a material of unknown properties, the context is the search for lawful mechanisms at work in the morphogenesis of living things. And within this field, the complementary aspect to biochemistry, mechanical forces and their role in such laws, constitutes the background for this work.
So here I will shortly introduce five endeavors to tackle this question and will try to identify possible shortcomings for each approach. The first two are concerned with the theoretical modeling of the situation, while the later three discuss different experimental approaches to infer stresses from different observables. More experimental approaches are available and a very good summary, including pros and cons for each was published in 2016 [28].
For a broader overview of the field it is recommended to look at the Philosophical Transactions of the Royal Society B, volume 372, issue 1720 [29].
Experimental approaches can be grouped as *in vivo*, where measuring takes place inside the animal or *ex vivo*, where measurement takes place after dissection. In analog to this nomenclature computational simulations of biological processes are referred to as *in silico*.
An important observation, which led to many of the here described efforts, was the uniformity of growth in the wing imaginal discs despite a gradient in growth-inducing morphogens which should stimulate growth more strongly in the center than at the periphery [30].

2.1. Basic Model

In 2005 it was proposed [31] that: "dependence of the rate of cell division on local stress could provide an “integral-feedback” mechanism stabilizing uniform growth." So the proposed mechanism is inverse to the one observed in bone, described in Section 1, a negative-feedback of stress on growth.
In 2007 it was shown [32] that already a simple model, integrating biochemical morphogen gradients and negative-stress-feedback, could account also for global size dependent growth arrest. A feat that is notoriously difficult for purely chemically regulated models.
In 2013 experimental evidence was presented [33] that supported this proposal by observing increased numbers of dividing cells in externally stretched wing discs than in unstretched ones.
And by 2016 it was concluded in a review of the role of mechanical forces in the growth of animal tissues [34] that: "A general rule of thumb of how mechanics influence growth is that the more cells are compressed, the slower they grow."

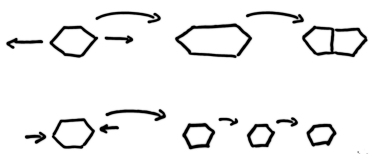

Figure 2.1: Mechanical stretch seems to promote cell division.

2.2. Vertex Model

To make the above described simple model more closely resemble real biological tissue its cellular composition was strived to accommodate. In 2007 a vertex model was introduced that described the apical actin ring network of the wing disc as a set of polygons [35]. At each vertex i, i.e. the edges of the polygons, see Figure 2.2, force-balance between an internal pressure (represented in the model by a departure from a fixed target area $(A - A^{(0)})$ of the apical cell area) and the constrictive force from the actin ring of length L plus external pull from the neighboring vertices j needs to be established. This can be described as local minimum of the following energy function:

$$E(R_i) = \sum_{\alpha} \frac{K_\alpha}{2}(A_\alpha - A_\alpha^{(0)})^2 + \sum_{<i,j>} \Lambda_{i,j} l_{i,j} + \sum_{\alpha} \frac{\Gamma_\alpha}{2} L_\alpha^2 \ , \tag{3}$$

where $F_i = -\frac{\mathrm{d}E}{\mathrm{d}R_i}$ gives the forces. α counts through the polygons/cells, $l_{i,j}$ denotes the length from vertex i to j and K, Λ and Γ are the coefficients of the area elasticity, line tension and circumferential contractility respectively.
Until 2012 this model was expanded to incorporate growth, cell divisions, rearrangements and apoptosis, as well as multiple, interacting chemical morphogen gradient adaptations and force feedback [36]. This led to reproduction of many experimentally observable findings like cell-packing statistics, the distribution of cell shape and size throughout the wing pouch and throughout development with growth termination at an appropriate size.
But such models need many input parameters and make many assumptions which experiments still need to provide and support. Another limitation of the vertex models described so far is the restriction to flat 2-d geometries. And it is non-trivial to adapt or expand them to 3-d tissues and to question whether the findings from 2-d will still hold true in 3-d. See [37] for a recent review.

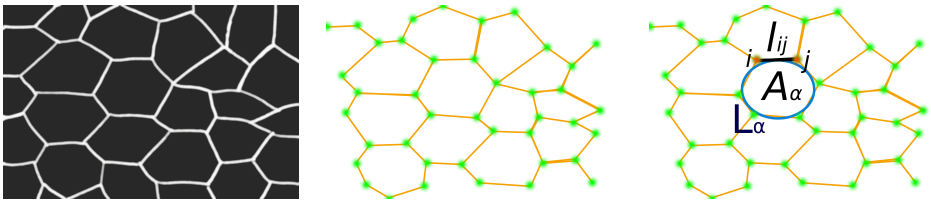

(a) (b) (c)

Figure 2.2: The idea of vertex models is to approximate apical cell shapes by polygons. Green dots signify the vertices, counted by i and j, separated by length $l_{i,j}$, polygons, in orange, have areas A_α and circumference L_α .

2.3. Photoelasticity

An interesting and sophisticated approach to visualize internal stress in a homogeneous and optically isotrop, flat material is to use photoelasticity. This is commonly used with Poly(methyl methacrylate) (PMMA), also known as Plexiglas, to test mechanical weak points of complex geometries under load.

[8] This is a bad and outdated colormap which should be avoided.

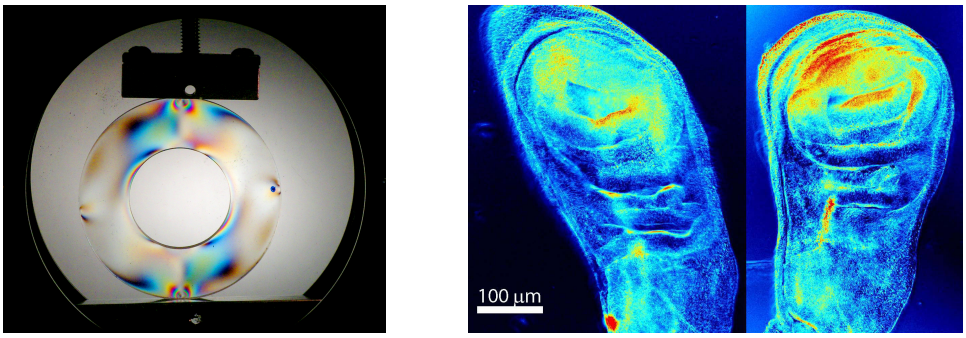

(a) (b)

Figure 2.3: Photoelasticity (a) in plastic where colors are due to actual wavelength dependence of polarization and (b) in living tissue where colors encode digitally recorded retardation time in a "jet"-colormap.[8]

The method makes use of the stress-induced birefringence of the plastic which means that the polarization of traversing light gets turned proportional to the integrated stress along the traveled path through the material. By analyzing the polarization, regions of higher stress can be identified, see Figure 2.3(a). Microscopically this is due to the fibrous nature of the material. The long proteins get oriented by the applied force and thereby introduce optical unisotropy, this leads to retardation of the light and birefringence.
In 2009 this technique was applied to the wing disc (*ex vivo*) and an inhomogenious retardation map was recorded for freshly dissected and undisturbed discs [38]. These inhomogeneities vanished after cutting the area or pulling on the disc. Therefore they were associated with internal stress distributions. Figure 2.3(b) shows such an image, taken from [39] [9], displaying the vanishing of retardance by stretching.
While these images look spectacular and convincing, I allow myself a remark of caution regarding their interpretation. Compared with the ones in plastic the differences in retardance are very small and the set-up needs to be extremely well calibrated to be able to pick them up. Anything that has the slightest influence on the signal might interfere with the interpretation. With this in mind: comparing Figure 2.3(b) with Figure 1.6(b) it can be seen, that there is some correlation between the retardance signal and the thickness of the disc, in other words the amount of tissue the light had to travel through. Since, as will be discussed in Section 6.3, the geometry changes upon stretching, leaving to a flatter topography, interpretation of the signal as a measure of thickness could be interfering with with the interpretation of stress induced birefringence.

2.4. Force Inference

Another intriguing approach, very near to the above introduced vertex models, is to employ Bayesian statistics to estimate the pressure of each cell and the tension along each cell to cell contact. It was introduced in 2012 [40] and takes an image of the apical actin network as input, segments the cells, identifies positions of the vertices and then solves the inverse problem as the

[9] This publication has a number of shortcomings, especially on the subject of the described mechanical forcing setup and the deduced acting forces, as well therefore on the described "spring constant of wing disc tissue". Which gave the starting point for the work presented in this thesis

above mentioned vertex model: given these positions, how do the coefficients for line tension and area pressure need to be in order for this observed configuration to be the local minimum of the energy function and therefore to be in force equilibrium?
As stated, this is a very intriguing approach. It does however suffer any limitations that the underlying vertex model has in terms of assumptions about the real biological force-bearing structures and mechanisms, as well as it being limited to 2-d [10] . And of course this method can only yield relative force distributions, never absolute measures. Important to note is the non-invasive nature of the method which means it can be applied where- and whenever cellular resolution imaging is possible, possibly *in vivo* [41], and the evolution of the tissue over time can be followed. Also, it can be applied to images not initially recorded with this goal in mind, given that the image quality is sufficient for cell segmentation.

2.5. Laser Ablation

One important tool to access and measure tension in the apical actin network is to cut the actin cables and record the initial recoil velocity v_{init}. Assuming viscous damping η the tension T is proportional to the product $T \propto v_{init} \cdot \eta$. The cut can be done using near-infrared lasers in a two-photon configuration, or with a pulsed UV-laser.
This can be applied to single cell-cell junctions [42] or on the tissue level [43].
Again this can give information about relative tension distribution, not absolute values. Also the time resolution of the imaging microscope needs to be sub second with good enough resolution and contrast to resolve the relevant structures. A feat which modern, more expensive microscopes are able to accomplish, but older ones tend not to.
This method could potentially also be applied *in vivo*, especially using the two-photon approach. But to my knowledge only *ex vivo* has been so far. And of course it is very invasive and can only yield local tension information at the specific time of cutting.

[10] While, for example, there seems to be no correlation between 2-d area and 3-d volume for cells in the wing disc [26].

3. Theory: Basics of Rheology

In this section I will briefly outline relevant concepts and models from rheology, the study of the flow of matter.
Most biological matter is characterized as soft matter (with exceptions such as bone or horn etc.). This means that the energy needed for deformation is comparable to the thermal energy scale. As a consequence observed deformations are big compared to what is assumed in classical, linear elasticity theory. Therefore for the description of the force-displacement behavior of the wing disc, the language of rheology was adopted which does not share this limitation.
I will first introduce Hookean springs, daspots and sliding frictional elements that give rise to elastic, viscous and plastic behavior respectively, see Figure 3.1 and will then proceed to discuss some well-known rheological models comprising of combinations of these basic elements. I will conclude by pointing out some of the boundaries of these models.

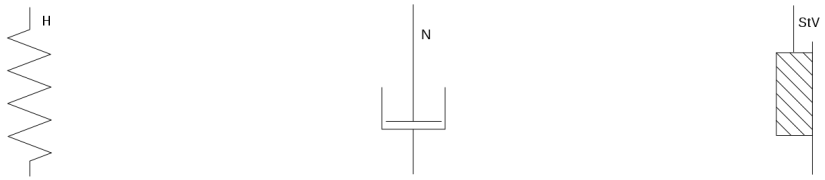

Figure 3.1: The base-elements of rheological models: (a) spring, (b) dashpot and (c) sliding-friction-element, describing elasticity, viscosity and plasticity of a material.

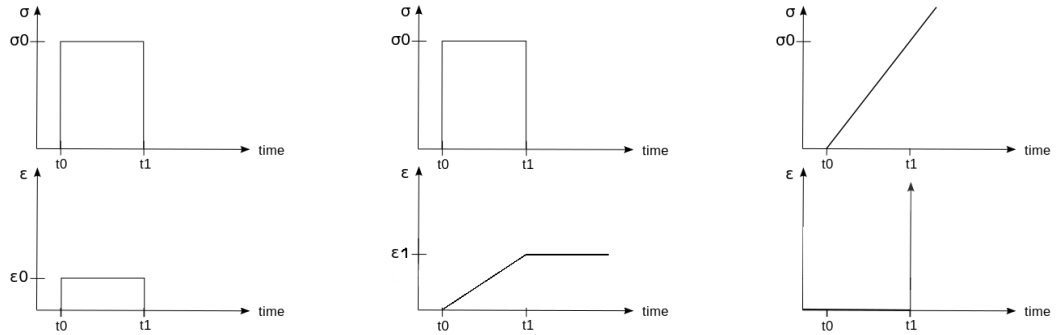

Figure 3.2: How the elements from Figure 3.1 respond to stress (a) Hookean elastic response, (b) Newtonian fluid response (c) ideal plastic rupture.

In the simplest case one associates solid matter with a Hookean spring, obeying:

$$\sigma_H = E \cdot \varepsilon_H \ , \tag{4}$$

where σ_H is the stress, E is the elastic modulus or Young's modulus of the material and ε_H is the strain. And liquids are preferably treated as Newtonian fluids obeying:

$$\sigma_N = \eta \cdot \dot{\varepsilon_N} \ , \tag{5}$$

where σ_N is the applied stress, η is the viscosity and $\dot{\varepsilon_N}$ is the linear flow speed.
A single sliding friction element, or Saint Venant element on its own describes rupture of a in-

finitely rigid material at a critical stress σ_0:

$$\varepsilon_{StV} = \begin{cases} 0 & \text{for } \sigma_{StV} < \sigma_0, \\ \infty & \text{for } \sigma_{StV} \geq \sigma_0. \end{cases} \quad . \tag{6}$$

Note, that the sliding-friction element introduces a non-differentiable non-linearity if included in a model.
The behavior of all elements can be easily visualized by Figure 3.2, plotting a strain-response to a sudden and constant or linearly increasing stress over time.
Additionally I will introduce an element corresponding to the inverse of the St. Venant element: the "stop-element" or "end-stop", see Figure 3.3.

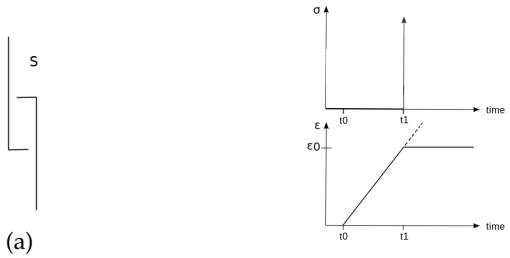

(a) (b)

Figure 3.3: Introducing the "stop-element" or "end-stop". While it is not presented in usual discussions on rheology it offers a simple way to approximate things like hardening of real springs etc. It can also easily be generalized to an exponential rather than a infinitely hard stop.

The stop-element obeys the non-differentiable definition:

$$\sigma_S = \begin{cases} 0 & \text{for } \varepsilon_S < \varepsilon_0, \\ \infty & \text{for } \varepsilon_S \geq \varepsilon_0. \end{cases} \quad . \tag{7}$$

But it can easily be generalized to an exponential form, allowing for a continuously differentiable non-linearity with sharpness c:

$$\sigma_{eS} = e^{c\cdot(\varepsilon_{eS}-\varepsilon_0)} \quad . \tag{8}$$

3.1. Simplest Models for Visco-Elasticity

The most common extensions to pure elasticity is the Kelvin-Voight model, see Figure 3.4(a), describing a visco-elastic solid, or in other words a damped spring. And to linear flow the common extension is the Maxwell model, see Figure 3.4(b), describing a visco-elastic fluid.
The respective equations look as follows:

$$\sigma_K = E_1\varepsilon_K + \eta_1\dot{\varepsilon}_K \quad , \tag{9}$$

$$\sigma_M + \frac{\eta_2}{E_2}\dot{\sigma}_M = \eta_2\dot{\varepsilon}_M \quad . \tag{10}$$

Where (9) describes the Kelvin-Voigt model, where the stress on the two elements add to give the total stress $\sigma_K = \sigma_H + \sigma_N$, while the strain on both elements is equal $\varepsilon_K = \varepsilon_H = \varepsilon_N$.

(a) (b)

Figure 3.4: The two possibilities to combine viscous and elastic behavior: (a) the Kelvin-Voigt model, describing a visco-elastic solid and (b) the Maxwell model that captures the characteristics of a visco-elastic fluid.

Equation (10) describes the Maxwell model, where the stress on both elements is equal $\sigma_M = \sigma_H = \sigma_N$ and the strains add $\varepsilon_M = \varepsilon_H + \varepsilon_N$.
Again the behavior can easily be visualized, see Figure 3.5.

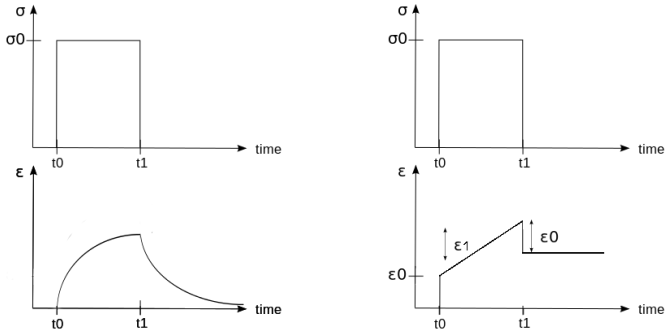

(a) (b)

Figure 3.5: The response of: (a) the Kelvin-Voigt solid and (b) the Maxwell fluid to sudden, constant stress.

To describe the exponential behavior of the damped spring in the Kelvin model seen in Figure 3.5(a), one often introduces the time constant $\tau_1 = \frac{\eta_1}{E_1}$, such that:

$$\varepsilon_K(t) = \frac{\sigma_K(t)}{E_1}\left(1 - e^{-\frac{t}{\tau_1}}\right) \quad . \tag{11}$$

To measure E_1 and τ_1 of a Kelvin-Voigt material one would measure $\varepsilon_K(\sigma_K, t)$ and fit (11) to the data. For a Maxwell material instead of exponential strain release as answer to a constant stress, there would be exponential stress release as answer to a constant strain (also with characteristic time $\tau_2 = \frac{\eta_2}{E_2}$). Therefore for measurements, fixing $\varepsilon_M(t)$ and measuring $\sigma_M(\varepsilon_M, t)$ would be conceptually simpler.

3.2. Burgers Model

The logical next step is the combination of the Kelvin and Maxwell models, see Figure 3.6. This is known as Burgers model [44]. It was proposed in 1935 to describe the behavior of asphalt and was later adopted to describe the rheological behavior of things like concentrated polymer solutions. By incorporating visco-elastic flow as well as -elasticity it is a very versatile model. Still, visualization of the strain reaction to constant stress is quite simple, since the stains of (9) and (10)

simply add, see Figure 3.7.

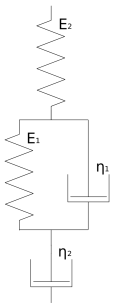

Figure 3.6: Burgers model; incorporating Kelvin-Voignt and Maxwell model and thereby creating a very versatile framework to describe visco-elasticity.

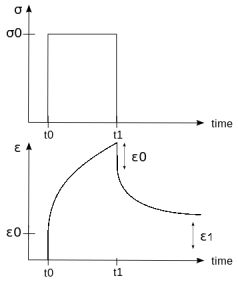

Figure 3.7: Visually the strain response to sudden-constant stress can be found by addition of the responses of Kelvin- and Maxwell materials.

However the full analytic solution now takes a slightly more complicated form, due to the necessity of carrying higher order time derivatives. Burgers model is a serial connection of Kelvin and Maxwell, so it can be derived from: $\sigma = \sigma_K = \sigma_M$ and $\varepsilon = \varepsilon_K + \varepsilon_M$. Using the first and differentiating the second of these equations with respect to time gets one to:

$$\dot{\varepsilon} = \frac{\dot{\sigma}}{E_2} + \dot{\varepsilon}_K + \frac{\sigma}{\eta_2} \quad , \tag{12}$$

$\dot{\varepsilon}_K$ can be taken from (9) as $\frac{\sigma}{\eta_1} - \frac{E_1}{\eta_1}\varepsilon_K$. This gives:

$$\left(\frac{1}{\eta_1} + \frac{1}{\eta_2}\right) \cdot \sigma + \frac{\dot{\sigma}}{E_2} = \dot{\varepsilon} + \frac{E_1}{\eta_1}\varepsilon_K \quad . \tag{13}$$

After solving for ε_K and taking another time derivative, this can be entered again into (12) and cleaned up to finally have the equation for the model using only rheological constants of the base elements:

$$\sigma \;+\; \left(\frac{E_1\eta_2 + E_2\eta_1 + E_2\eta_2}{E_1E_2}\right) \cdot \dot{\sigma} \;+\; \frac{\eta_1\eta_2}{E_1E_2} \cdot \ddot{\sigma} \;=\; \eta_2 \cdot \dot{\varepsilon} \;+\; \frac{\eta_1\eta_2}{E_1} \cdot \ddot{\varepsilon} \quad . \tag{14}$$

Like in the Kelvin-Voigt and Maxwell models the equation might be easier to read when writing it in terms of the time constants $\tau = \frac{\eta}{E}$:

$$\sigma \;+\; \left(\tau_1 + \tau_2 + \frac{\eta_2}{E_1}\right) \cdot \dot{\sigma} \;+\; \tau_1\tau_2 \cdot \ddot{\sigma} \;=\; \eta_2 \cdot \dot{\varepsilon} \;+\; \tau_1\eta_2 \cdot \ddot{\varepsilon} \quad . \tag{15}$$

Note that there is no term proportional to ε. This means there is no distinct rest configuration per se and the model, due to the lower dashpot with viscosity η_2, fundamentally describes liquid-like behavior.
Also note, that a-priory one does not know which model is appropriate to describe a new material. This has to be read out of the forms of the measured $\varepsilon(t)$ and $\sigma(t)$.
To find or construct a fitting material model for the wing disc was a major part of this work. Because only then can mechanical properties be assigned as quantitative parameters, see Section 7 for the results.

Part II.

4. Inception: Tensegrity

As touched upon in the end of the previous part, in Section 2 , many of the common approaches to tackle forces in the wing disc are limited to a model of a two-dimensional cable network under tension balanced by area pressure.
Here I will interpose a rivaling inherently 3-dimensional concept which produced some interesting predictions concerning force-displacement behavior.

4.1. Tensegrity in Biology

In 1993 D. E. Ingber suggested to look at the cell from an architectural point of view [45] and formulated the hypothesis that cells fundamentally follow design rules of "tensegrity" [46]. The term was constructed by Buckminster Fuller in the 1960s from "tensional integrity" to describe the structural principle that stability can be achieved through a balance of continuous tension and discontinuous compression. This is in contrast to the typical way buildings are constructed, where loads are continuously passed through compression elements, such as walls or beams, from the roof down to the earth. Also modern suspension bridges are not tensegrity structures. The cables are tension elements but they are localized and still the total load of the bridge is carried compressively by the towers. Figure 4.1 shows a simple 3-prism tensegrity structure composed of three non-touching compressional struts and nine tension bearing cables spanning the whole structure. Note, that at each edge always one strut and three cables meet.[11]

Figure 4.1: Simple 3-prim tensegrity structure, from [47].

[11] Tensegrity structures are probably best known as children's toys, as which the tensegrity cube is often sold.

4.2. MATLAB simulation

This design principle can be generalized to a prism with an n-sided polygonal base as follows: Let A_i be the vertices of the upper (say, apical) side with i going from 1 to n and B_i the ones on the lower (basal) side. For any i the strut will go from A_i to B_{i+2} and cables will go to A_{i-1}, A_{i+1} and B_{i+1}. This rule will generate stable tensegrity prisms of any number of vertices. Figure 4.2(a) shows a hexagonal prism built from this rule, showing a screenshot from a matlab simulation of the structure.

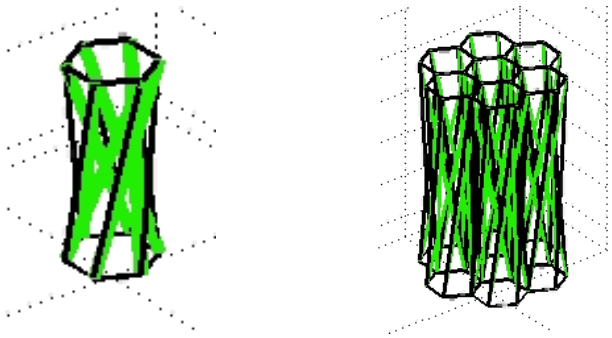

(a) (b)

Figure 4.2: (a) Design principle of 3-prism, generalized to hexagonal prism. Struts are in green, cables in black. (b) Seven hexagonal prism joined to form a small patch of "epithelium".

Of course such prisms could now be joined to form something that could start to resemble a 3-dimensional cellular epithelium. Figure 4.2(b) shows seven hexagonal prisms joined to a small "tissue-patch".
It might be noteworthy, that Ingber himself continues to advocate tensegrity as the right way to look at cellular architecture and also developed concepts how it could help explain mechanotransduction through the hierarchical structure from cell to the nucleus and influence cellular information processing [48] [49]. There are also advocates for the use of tensegrity as the primary structural principle in biology in general, using the term biotensegrity, even though these usually seem to have a medical background and particularly mean body mechanics [50], [51] [12]. But to my knowledge there is no one who adopted this standpoint for epithelia. In my eye the tensegrity prism would be the logical simplest form to extend a 2-d vertex model to a 3-d one. It offers many interesting options in the continuous tension of looped cables, that couple the individual cells together to a whole tissue in a very intelligible way. Also it offers obvious possibilities to include the nucleus and interpret struts as microtubules, that could connect to the nucleus and shorten to pull it up for cell division while an additional polygon of tension cables could be added in the middle of the cells to pull the cell together and push the nucleus upward [53], etc.
Another important feature of tensegrity structures, due to the possibility of slippage of the cables and therefore gradual distribution of a pulling force on the tension and compression bearing parts, is a "linear stiffening" response to applied stress [54]. This is especially clearly observable if there is no prestress in the looped cables. Figure 4.3 shows the force-displacement curve for the patch of "tensegrity-cells" shown in Figure 4.2(b), when subjected to harmonic pulling at the sides. In this simulation some noise on the rest lengths and viscous drag have been implemented.

[12] Tensegrity is of course pursued also outside of biology. It is used in architecture and notably also for deployable structures for space applications [52].

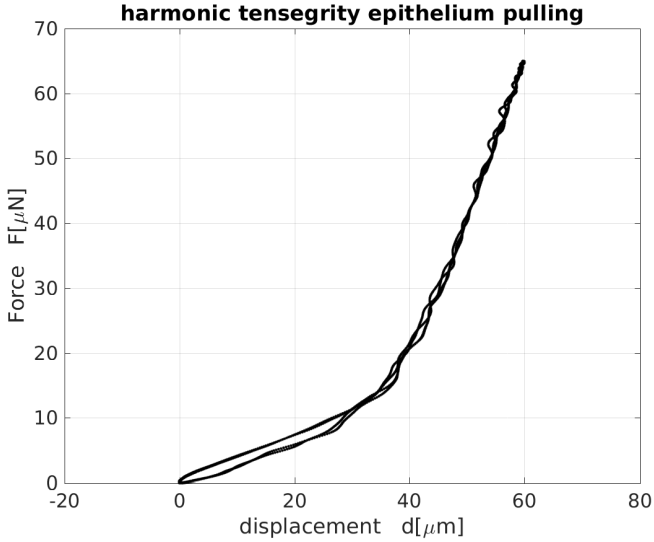

Figure 4.3: Reaction to pull on the outer cells of the patch shown in Figure 4.2(b).

Remarkably the experimental results presented in Section 6.1 show high qualitative similarity to these simulations.

5. Experimental Approach: Extensometer

The wing disc as a living tissue is an extremely soft and therefore highly vulnerable proto-organ. The measurement of its mechanical properties requires it to be alive yet accessible to physical contact and controlled manipulation. Therefore it must firstly be dissected from the larva and transferred to a suitable medium. Secondly the disc must be attached on both sides while otherwise free, one side must be movable with very high precision in position, force and time. Additionally it was required that the wing disc should be observable with a confocal microscope throughout the whole experiment in order to observe the 3-d geometry of the disc during extension.
Here I will describe the general set-up in Section 5.1, Section 5.1.1 will go into detail about the construction of the experiment and the used items, while Section 5.1.2 will describe the software that was written to control the measurements. Section 5.2 will discuss the preparation protocol, full details of which can be found in appendix A detailing dissection of the larvae and mounting of the wing disc. Section 5.3 will outline the imaging process and -possibilities during measurements.

5.1. Set-up

As outlined above, the experimental set-up had to fulfill a number of requirements. First and foremost it had to be able to measure force and displacement with high precision and temporal resolution in order to extract time-dependent force-displacement characteristics from which the mechanical properties could be derived. Next it had to accommodate the physiologically relevant medium required for the cells of the wing disc to survive. We used the optimized wing disc culture medium, WM1 [55].
In order to stretch the wing disc in one direction, it had to be attached on one side while the opposing side had to be precisely movable. Finally the whole set-up had to be mounted on-top of a confocal microscope to ensure imaging capability.

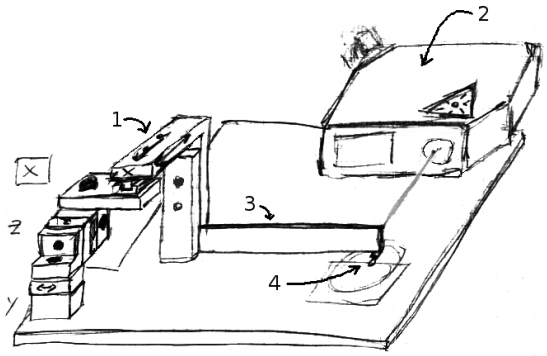

Figure 5.1: This sketch illustrates the general measuring set-up. **1**: 1-d positioner, **2**: laser displacement sensor, **3**: spring steel cantilever, **4**: wing disc.
By monitoring the end position of the cantilever with the displacement sensor while moving the positioner, the time-dependent force-displacement relationship of the wing disc can be observed.

Figure 5.1 shows the central components of the experiment. Simply stated it consists of a spring **3** with known stiffness k which is used to pull on the wing disc **4**.

Since one side of the wing disc is fixed, the extension of the wing disc and the displacement d of the end of the cantilever can be equated. It is measured with a laser displacement sensor **2** from micro-epsilon using optical triangulation [56]. Additionally only the position p of the other end of the cantilever, controlled using a 1-d positioner **1** from SmarAct [57], needs to be known at any time to compute the force F acting on the wing disc using Equation (16).

$$\Delta x = (p - d)$$
$$F = k \cdot \Delta x \tag{16}$$

The stiffness k of the spring sheet can be estimated using Euler–Bernoulli beam theory:

$$q(y) = \frac{\mathrm{d}^2}{\mathrm{d}y^2}\left(EI\frac{\mathrm{d}^2 w}{\mathrm{d}y^2}\right) \ , \tag{17}$$

y .. position along the beam
q .. distributed load
w .. deflection of the beam at position y
E .. elastic modulus
I .. second moment of inertia.

In our case force is only applied at the free end of a uniform cantilever-beam at $y = L$, where $w(L) = \Delta x$, so:

$$q = \begin{cases} 0 & \text{for } y \neq L \ , \\ F & \text{at } y = L \ . \end{cases}$$

This simplifies Equation (17) to (18). And since for a rectangular beam also I is known, given by Equation (19), k is just a function of the dimensions of the cantilever and its elastic modulus, see Equation (20).

$$F = \frac{3EI}{L^3} \cdot \Delta x \ , \tag{18}$$

$$I = \frac{a^3 \cdot b}{12} \ , \tag{19}$$

$$k = \frac{E \cdot a^3 \cdot b}{4 \cdot L^3} \ , \tag{20}$$

a .. width,
b .. height
L .. and length of the cantilever.

However, to have a greater degree of accuracy, the stiffness k was also measured in a calibration experiment using a microforce sensing load cell. These revealed a somewhat lower stiffness than calculated, see Section 5.1.1, Figure 5.12. This is attributed to torsion of the cantilever, not taken into account by the simple 1-d version of Euler-Bernoulli beam theory given in Equation (17).
As can be seen from Equation (20) and (16) the accessible force range of the experiment in this set-up can be easily changed by replacing the used spring sheet with one of altered thickness a without changing anything else in the set-up. As described below in Section 5.1.1 the dimensions of the spring sheet were chosen to be sensitive to forces in the low micro-Newton range. This

opened up the possibility to measure the previously inaccessible domains of the very low end of the force-displacement curve. As a result the set-up became extremely sensitive and susceptible to external influences. The most prominent disturbances came from air-movements, tugging the cantilever and leaving it swinging. However these could be greatly reduced by placement of a simple box over the set-up, as will be described in Section 5.1.1.
As will be discussed in detail in Section 5.1.2, a feedback loop was used to adjust position p dynamically. This way it was possible to either control F and measure d, or control d and measure F. In both cases the input could be set to be an arbitrary function of time.

5.1.1. Hardware

Overview
The whole set-up was built to be easily movable and essentially portable. It fit onto different microscopes, even though in the end it was mostly used on a Leica DM IRBE TCS SP. Figure 5.2 shows the experiment set up on said microscope. And Figure 5.3 shows a rendering of all the designed and machined parts, including the laser displacement sensor, and the condenser Lens from the microscope to ensure proper fit and alignment of all components.

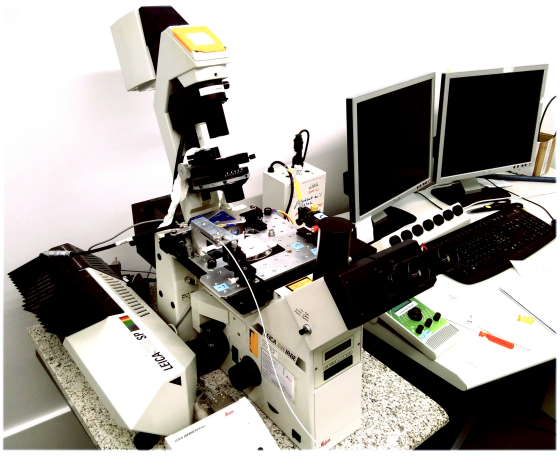

Figure 5.2: Experiment set up on the DM IRBE TCS SP1 from Leica.

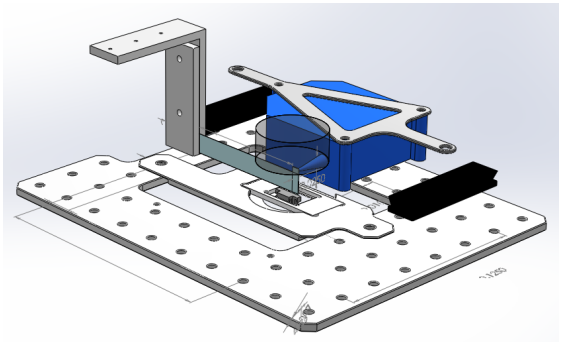

Figure 5.3: Rendering of most of the set-up, including displacement sensor and condenser lens from the microscope to ensure everything will fit.

Base plate

A base plate out of hi-quality aluminum with regular bore holes which conform to the standard of optical set-ups was made by the workshop, see Figure 5.3. The central opening allows for the movement of the revolver of the microscope objectives. In addition the opening allowed the placement of different sample holders. The one used and shown in Figure 5.3 was made to accept 60 mm $\times$ 26 mm slides or 55 mm glass bottom dishes.
The z-stage of the microscope was removed before placement of the baseplate since the weight of the experiment would have exceeded the critical load. z-stacks were recorded by movement the objective of the microscope.

Sample placement

For confocal imaging the wing disc should be as close to the objective as possible. This is usually achieved by gently pushing it flat against the glass cover slip through which the image is acquired, see Figure 6.18. However, for accurate force-displacement measurements the wing disc should not be in physical contact with the cover slip (to avoid friction). The solution to this problem is illustrated in Figure 5.4. The wing disc is attached to the underside of two glass slides. One glass slide was fixed to a small stainless steel block (subsequently called "disc inverter") into which a step of 300 µm was cut, see Figure 5.5. Both glass slides had a thickness of 150 µm. This left another 150 µm of space, enough for the wing disc to fit in while not touching the lower cover slip. Choosing a cover slip of No. 0 with a thickness of 100 µm in combination with a 20x water immersion objective with a focal length of 260 µm (Leica HC PL APO 20x/0.7 IMM CORR) [58] allowed to get good confocal images almost through the whole wing disc and well up to the fixed glass slide. More details on the imaging process will be given in Section 5.3.
After starting experiments it was quickly noted that the disc often ruptured, right at the edge of one of the glass slides to which it was attached. It was suspected that this was not caused by the applied force, but rather by the sharp edges of the glass slides. To test and prevent this the glass slide edges were heated with a butane torch to round them. This turned out to prevent any further rupturing of the discs. But it also made it more difficult to know up to exactly where the disc was attached.
Since the wing disc needed to be immersed in medium throughout the experiment a small rectangular pool was glued onto the cover slip. The mini pool was fabricated from zip tie, 1 mm $\times$ 3 mm. To get the corners right it was held against the disc inverter and lightly pinched with a side cutter. This allowed for precise and easy bending. It was glued at the last corner using loctite super glue and with araldit, a two component epoxy resin, to the cover slip. Epoxy was used since it turned out to be easier to get a watertight splice and to insure biocompatibility for the tissue.
The cover slip then could be placed in a 60 mm $\times$ 26 mm aluminium frame for easy handling. Figure 5.6 shows the disc inverter, highlighted in green, inside the pool, highlighted in yellow, on the cover slip, in blue, inside the aluminium frame. Here one can see the "handles" of the disc inverter holding on to the pool. These were later cut off, see A, item VII:.

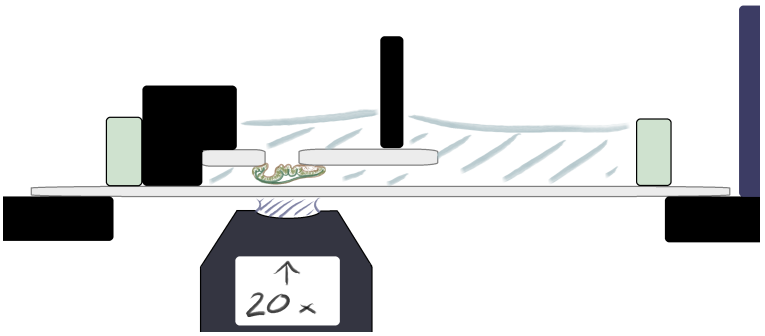

Figure 5.4: Vertical cross section view of the set-up, showing the wing disc attached to the underside of two glass slides, the left one fixed, the right one movable, immersed in wing medium 1 (WM1) [55], while accessible to imaging from the bottom.

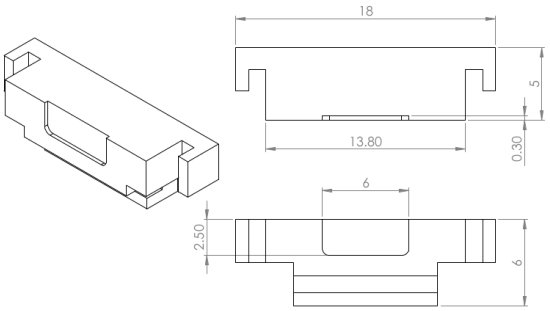

Figure 5.5: This disc inverter was made from stainless steel. Into the 300 µm deep step a 150 µm thick glass slide was glued. The wing disc was then attached to this glass slide and could be turned upside-down with it. The "handles" were later cut off, see Section A.

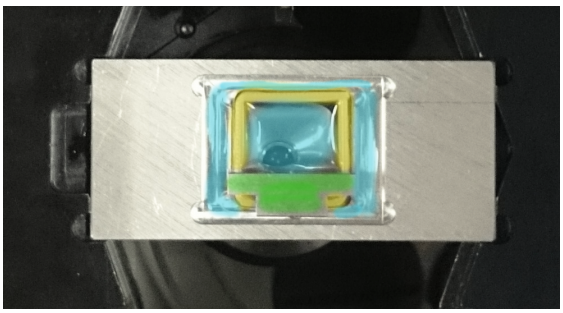

Figure 5.6: This image shows the used sample-holder (custom-built aluminium plate) containing a mini pool (yellow) together with a disc inverter (green) mounted onto a cover slip (blue).

Cantilever

The second glass slide to which the wing disc was attached was fixed to the end of the cantilever. The cantilever, see Figure 5.7, was laser-cut from hardened spring steel W.-No. 1.1274 [59] from h+s Präzisionsfolien GmbH. This was done in order to avoid leaving residual strain in the material as would be the case after conventional cutting and drilling. This material was chosen to maximize linearity of the cantilever as a spring.

Figure 5.7: The chosen shape for the cantilever: The holes were made to ensure precise horizontal orientation. They fit onto two pins embedded in one of the two pieces of aluminum that clamp around the cantilever.

On the right side one can see a thicker stripe of steel, which was spot-welded to the cantilever-beam. This flag-like extension served the purpose to ensure the laser-beam from the displacement sensor (see Figure 5.1) would hit it, even if the lower end was lowered into the medium. The lower extension was intended to directly support the second glass slide to which the wing disc would be attached. However, as Figure 5.10(a) illustrates, a substantial temporal drift in the measured force could be observed with this configuration. This drift could be correlated to evaporation of the medium. Presumably what had happened was that the surface of the medium formed a meniscus in-between the extension of the cantilever and the disc inverter, exerting tension onto the cantilever, see Figure 5.8. Then the evaporating medium changed the geometry of the meniscus and therefore the tension. To reduce the effect of the surface tension, the end of the cantilever was modified and the surface breaking part was flipped by 90°, see Figure 5.9.

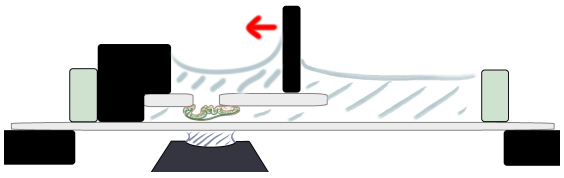

Figure 5.8: The chosen shape for the cantilever. The holes are to ensure precise horizontal orientation. They fit onto two pins embedded in one of the two pieces of aluminum that clamp around the cantilever.

With this modification the observed drift in force could be reduced by over a factor of two as shown in Figure 5.10(b). The drift could be further reduced by placing wet tissues onto the baseplate around the set-up and covering it under a cardboard box, reducing evaporation of the medium.

The clamps, used to hold the cantilever and connect it to the linear positioner, were mounted to a 2-axis translation stage for y- and z-axis control. They also ensured a clear point of beginning of bending for the cantilever. The therefore active dimensions of the cantilever are given in table 5.1. Using Equation (20) this amounts to a spring constant k_{calc} of $0.151(5)\,\mathrm{N/m}$.

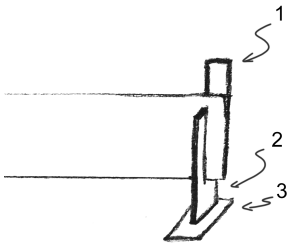

Figure 5.9: Modified cantilever end on the new spring. **1**: White-painted position indicator, **2**: lower extension that breaks through the surface of the medium, flipped by 90°in order to reduce surface tension, **3**: glass slide to which underside the wing disc was attached.

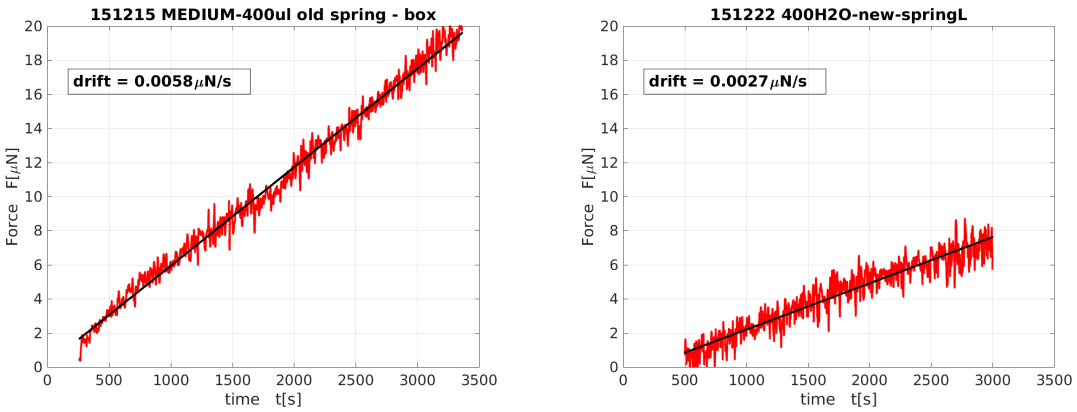

(a) (b)

Figure 5.10: These plots show the linear change in measured force as a function of time, associated to a change in surface tension. (a) shows the situation using a lower extension of the cantilever parallel to the disc inverter as depicted in Figure 5.7, (b) shows it with the lower extension flipped by 90°, as depicted in Figure 5.9.

	Variable		Value (Uncertainty)	Unit
	E	$=$	$2.10(1) \cdot 10^{11}$	Pa [59]
	a	$=$	$0.050(1)$	mm
	b	$=$	$12.70(1)$	mm
	L	$=$	$82.0(1)$	mm
$\overset{(20)}{\Longrightarrow}$	k_{calc}	$=$	$0.151(5)$	N/m

Table 5.1: The measured dimensions of the cantilever-spring.

Calibration

As stated in Section 5.1 the cantilever-spring was also calibrated against a commercially available force sensor from FemtoTools [60], (S540) shown in Figure 5.11(a). For this calibration the device with ID nr. 1613 was used. Its corresponding calibration was provided by FemtoTools, see page 65 in the appendix. Figure 5.11(b) shows the calibration configuration, the cantilever and glass slide are highlighted in green. Figure 5.11(c) shows the view from the microscope, that was used to ensure the tip of the FemtoTools force sensor touches the glass slide at the place where the wing disc would otherwise be attached.

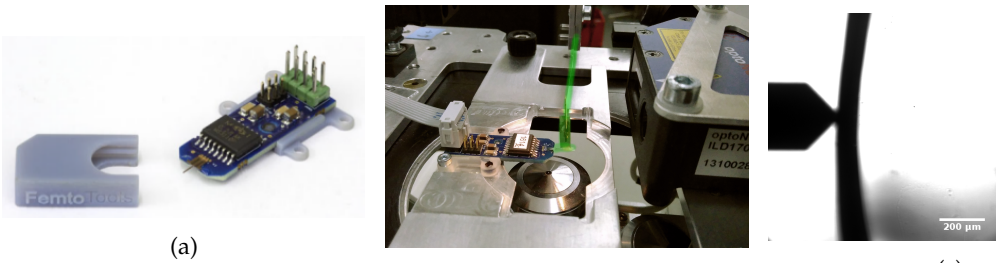

(a) (b) (c)

Figure 5.11: These images document the calibration process. (a) shows the commercial force sensor [60], (b) shows it installed on the set-up, with the cantilever highlighted in green and (c) shows the view through the microscope, left the tip of the FemtoTool, right the curved glass attached to the cantilever, ensuring correct placement

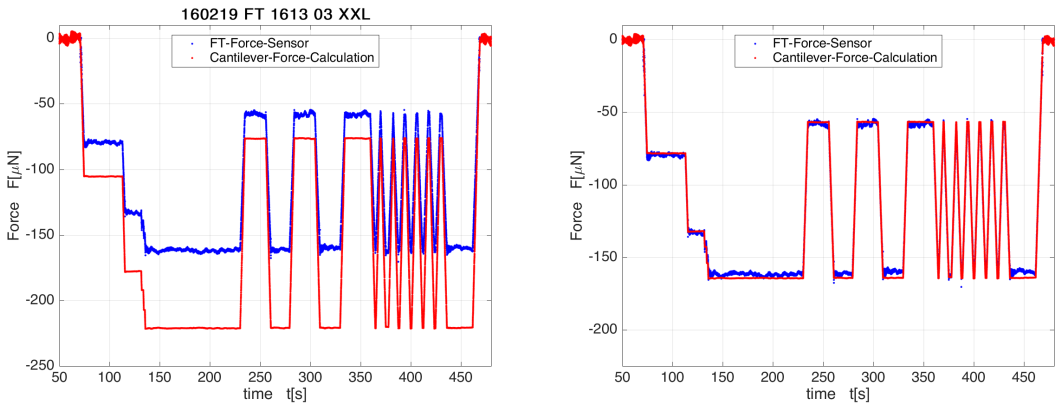

(a) (b)

Figure 5.12: These plots show the force measurements as a function of time used for calibration. The FemtoTools force sensor data is in blue and those from the cantilever in red. (a) shows the data using k_{calc} as calculated using Equation (20). (b) shows the same data re-scaled after calibration resulting in good agreement. Only a slight non-linearity might be detected. Stability of the cantilever data under load is very good, but at low force noise increases.

FemtoTools also provided a controller and software [61] to read-out and save the force measurements. The results are shown in Figure 5.12(a). The obtained data were then used in Equation (16) to compute the calibrated spring constant:

$$k = 0.112(2)\,\mathrm{N/m}.$$

This 0.74-fold deviation from the calculated value is well out of the estimated uncertainty and has to be attributed to deviation of the bending of the real cantilever from the ideal situation of Equation (20). Most likely torsion happens in the cantilever beam, amplified by the attached elongation in z-direction. Figure 5.12(b) shows the calibrated data. A slight non-linearity can be detected, which could be stemming both from the FemtoTools sensor (see calibration sheet on page 65) or from a non-linearity in the cantilever. Stability of the cantilever data under load is better than from the commercial sensor, but at very low forces this is inverted. The reason for this is investigated further below in paragraph noise reduction.

SmarAct positioner

As described above, the left end of the cantilever was fixed in-between two clamps, rigidly connecting it to the SmarAct positioner (**1** in Figure 5.1). Here we used one of type SLC-1750-M [57], a linear crossed-roller slide with a width of 17 mm, a length of 50 mm and an integrated microsensor. It uses a friction-based Stick-Slip principle of motion, illustrated in Figure 5.13, reproduced from [57]. A piezo element is fixed, the movable slide rests on it (I). A slowly changing voltage, applied to the piezo element elongates it and moves the sticking slide (II). An abrupt drop in the applied voltage lets the piezo element shrink and the inertial force of the macroscopic slide is higher than the friction force between piezo element and slide, leading to slipping and sticking at a new position of the slide (III). The frequency of repetition and height of this step can be controlled by a physical controller or via LabVIEW code.

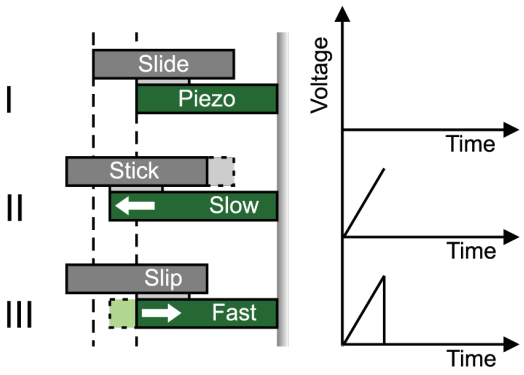

Figure 5.13: The friction-based Stick-Slip principle of motion of the SmarAct positioner, copied from [57]. **I**: piezo element and slide stick. **II**: Slow voltage change elongates the piezo element, and slide follows. **III**: Quick voltage drop shortens the piezo element, and slide slips. One step is completed.

This principle of motion offers comparatively huge travel distance of over 30 mm, while still taking advantage of the fine precision of the piezo element. However the frictional Stick-Slip does not yield perfectly reproducible step length. The positioner is therefore equipped with a closed-loop optical positioning sensor of type microsensor (-M). This gives it a reclaimed position resolution of 100 nm on our position p. Options with 1 nm resolution are available, accessing the full precision of the piezo element, but this was not needed for this work.

Micro-epsilon laser displacement sensor

As outlined in Section 5.1, in addition to position p of the beginning of the cantilever, we need to

know the displacement d of the end of the cantilever from its rest-position, in order to calculate the acting force F on the wing disc, see Equation (16). To do this with minimal interference the optical displacement sensor optoNCDT ILD1700-2 from micro-epsilon was chosen [56]. It offers a measuring range of 2 mm at a distance of 25 mm with a resolution of 100 nm, placing it in the same range and sensitivity as the SmarAct positioner. The measuring rate can be set from 312.5 Hz up to 2.5 kHz. It projects a red laser point onto the backside of the cantilever and records its reflection as seen through a fixed lens. As can be seen from Figure 5.14, this position information can be translated into angle information, which in turn yields distance information.

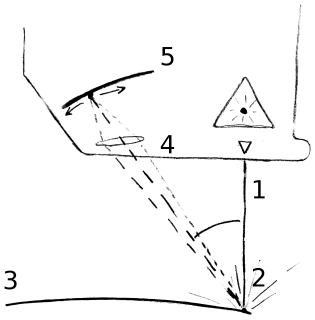

Figure 5.14: Displacement measurement principle. **1**: Laser beam, **2**: diffuse reflection from **3**: cantilever, through **4**: lens projected on **5**: 1-d-CCD-strip.
If **5** registers the point further to the right, the angle between outgoing beam and reflected light got smaller. This means **2** moved further away.

The ILD displacement sensor was attached to a mounting, movable in x- and y-direction, in order to be able to position the reflection of the laser beam at the end of the cantilever, in the appropriate measuring distance, before each measurement, if needed. After some practice in sample preparation and placement this became superfluous.

Noise reduction

As was mentioned before and could be seen for example in Figure 5.10(b), there was a substantial amount of noise in the low force regime. As described earlier this was due to air flow in the near vicinity of the cantilever. A simple shielding box, put over the set-up, reduced these significantly. Figure 5.15(a) shows the used box over the experiment. Figure 5.15(b) shows the effect of the addition of the cardboard box on the noise on the measured force. Calculating the standard deviation in the light green section and the light red section of same duration shows a reduction of the noise by a factor of 3.85 in air. This resulted in a standard deviation of 0.08 µN under the box in air.

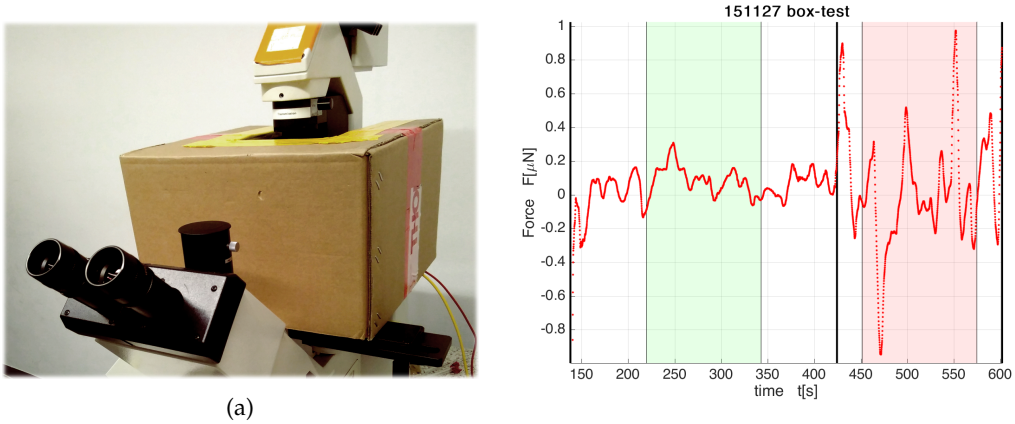

(a) (b)

Figure 5.15: Addition of cardboard box over the set-up reduced noise on the force measurement. (a) shows the box on the microscope. (b) highlights the effect. Standard deviation of the measured force in equal time intervals, green with and red without box, were calculated, revealing a reduction of fluctuations by a factor of more than 3.8.

5.1.2. Software

In order to control the experiment a Virtual Instrument (VI) was constructed, using National Instruments' LabVIEW 2014 [62]. Its essential purpose was simply to read the displacement $d(t)$ of the cantilever end as a function of the position of its beginning $p(t)$.
However: Firstly position p was not the relevant quantity, the force $F \propto (p - d)$ was. Secondly to be able to extract meaningful mechanical quantities one wanted to tightly control either $F(t)$ or $d(t)$. The behavior of both of these will depend on the mechanical properties of the wing disc. So there is no a priory knowledge of the movement on $p(t)$ to produce a desired behavior in $F(t)$ or $d(t)$.

PID controller

To solve these problems a PID controller (proportional–integral–derivative controller) was used in the heart of the software to continuously monitor $F(t)$ or $d(t)$ and adapt $p(t)$ accordingly. PID controllers are built to mimic the process by which one steers a ship, adding together knowledge (proportional) how the control value (steering wheel position) influences the process value (ships course), (integral) how the integrated past (speed) effects the needed output and (derivative) how the momentary change (acceleration) influences it. Figure 5.16 shows the scheme with the formula. The three parameters K_P, K_I and K_D need to be adapted to the specifics of the set-up and there are no general easy rules on how to find the right combination. In this thesis a combination of educated guessing and trial-and-error based varying was used to arrive at a satisfactory behavior, meaning noise reduction by activation of the PID controller.
During the course of this thesis both possible variants of the software were implemented: to require a varying setpoint for the force $F_{set}(t)$ and measure the corresponding displacement response $d(t)$, or vice-versa. In both cases $p(t)$ is the process value the computer can control and the measured $F(t)$ or $d(t)$ form the process value. There is no difference in principle. So in this section I will focus on the description of the first variant where $F_{set}(t)$ is given.

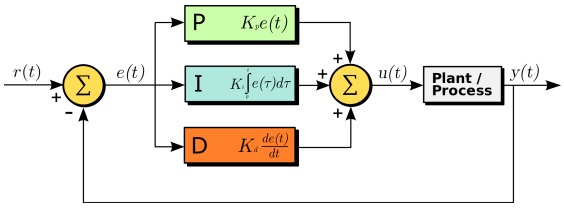

Figure 5.16: PID scheme: the difference of the desired setpoint $r(t)$ and measured process value $y(t)$, $e(t)$, is passed to the PID controller. It produces the new control value $u(t)$ as the sum of three components: one proportional to $e(t)$, one proportional to the integrated value of $e(t)$ and one proportional to the change in $e(t)$ [63].

User interface

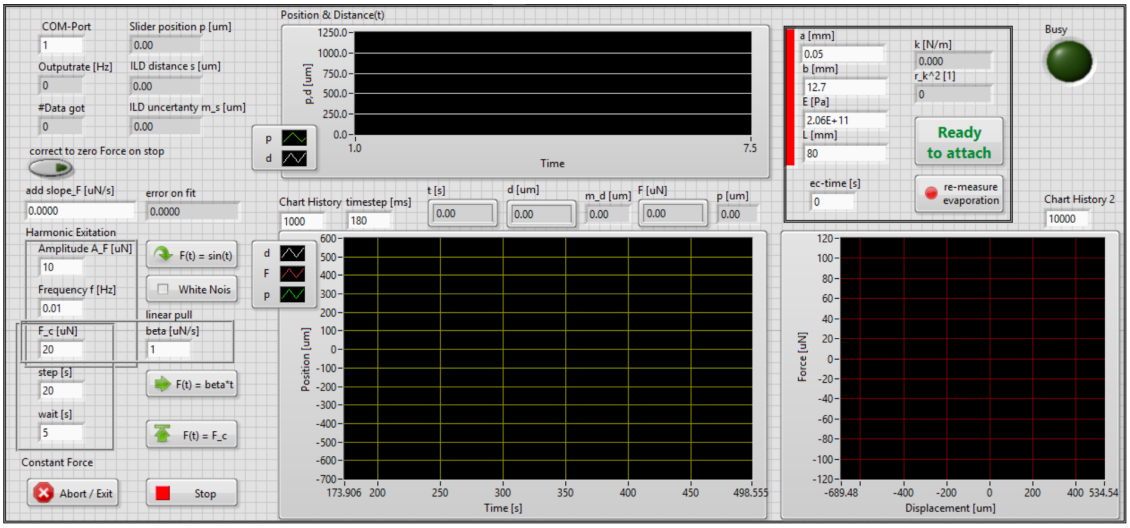

Figure 5.17: The LabVIEW user interface of the measurement software.

Figure 5.17 shows the user interface of the measurement software written in LabVIEW. The workflow leads from the upper left corner to the upper right and then to the lower left corner. After setting the COM-port for the ILD-sensor, its readings are displayed in the upper, center graph. This can be used to reposition the whole sensor until the cantilever is in optimal measuring distance. Next the Dimensions of the cantilever can be entered in order to calculate the spring constant or enter the spring constant manually. When everything is ready to start the measurement, "Ready to attach" is pressed. This measures 8000 position and force values and sets the mean as zero force and zero displacement. At this time a a ".dat"-file is generated and data is appended on the go. This way data can not get lost.
If desired the change of the measured force over time due to evaporation can be measured before attachment and actively corrected for during the measurement. However it was found that for accurate correction the evaporation needs to be measured over about 30 to 60 s. And, as to be discussed in Section A, the time before attachment should be minimized. Therefore for almost all measurements it was decided to correct for the change in measured force in data analysis.
After the sample is attached four types of measurements are programmed into the software.
1. Harmonic measurement: with amplitude A_F, frequency f, and offset F_c.

2. White Noise: This was used to measure the eigenfrequency of the cantilever which was filtered out during data analysis.
3. Linear increase over time with slope β up to the set maximum F_c at which it was kept constant.
4. Step function: Jump to fixed value F_c. Difficult for the PID.

The entered time step Δt determined the rate of cycling through the PID controller and saving of data points. It was found that a time step of 180 ms worked well in combination with the previously discussed PID constants. The ILD sensor was set to measure at a rate of 2.5 kHz. During one time step data would be collected and the mean would be passed on as displacement $d(t_i)$. From the position $p(t_i)$ of the SmarAct positioner the acting force $F(t_i)$ was calculated using Equation (16) and the spring constant k found from the calibration. This $F(t_i)$ was then compared to the value set for F_{set} by the PID controller which moved the positioner to a new position $p(t_{i+1})$ and after 180 ms the whole process repeated. $d(t)$, $F(t)$ and $p(t)$ were continuously displayed in the lower central chart and the lower right chart plotted $F(d)$.

When starting one of the four measurement types, a new data file was created, extending the name by **H**, **N**, **L** or **C**.

At each time step the time t [s], displacement d [µm], force F [µN] and slider position p [µm] were appended to the data file. As well as uncertainties for each of those but p, since it was constant $m_p = 0.1\,\mu\text{m}$.

The uncertainty in time was measured as the difference in the CPU timer.

The uncertainty in the displacement was given by the standard deviation of the measurements from the ILD-sensor during the time step.

And the uncertainty in the force is calculated by error propagation as:

$$m_F = \left| \sqrt{\frac{(m_d^2 + m_p^2)}{(p-d)^2} + \left(\frac{m_k}{k}\right)^2} \cdot F \right| \quad , \tag{21}$$

where k and m_k from the calibration on page 28 were used.

The continuous live display of the acquired data on the same charts, regardless of measurement type, made the use of global variables necessary. This is usually avoided when using LabVIEW, for good reasons. The primary appeal of LabVIEW as a programming language is its linear and local data-flow, which allows for its characteristic visual approach, akin to cables and wires. The use of global variables undermines this approach and made the whole programming effort much grater than would otherwise have been necessary.

5.2. Preparation Protocol

Here I will describe the final preparation protocol as a step-by-step list. A detailed description can be found in appendix A.

I. start PCs, microscope, laser, ILD-sensor, positioner and Leica- and LabVIEW-software

II. treat glass slides with PLL

III. dissect wing disc from late 3rd instar larva in WM1

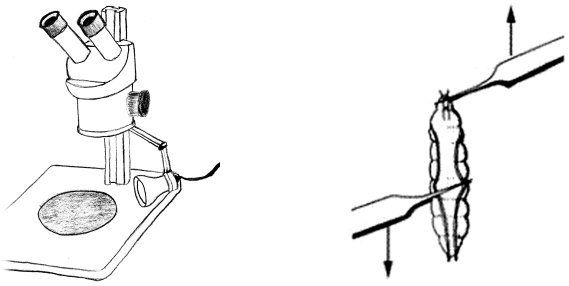

(a) (b)

Figure 5.18: (a) This position of the light source on the dissection scope results in dark-field image with higher contrast, (b) from [64], placement of tweezers to open larva for dissection.

IV. transfer wing disc to PBS

V. attach first side to glass slide of disc inverter in PBS

VI. turn disc inverter and place onto cover slip in pool (still under PBS)

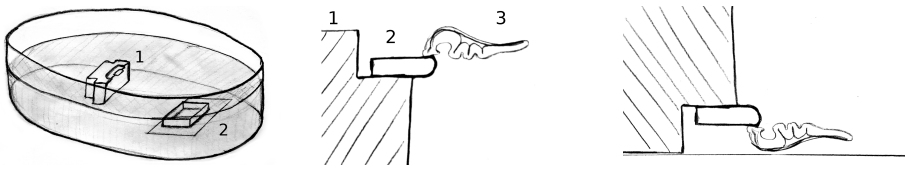

(a) (b) (c)

Figure 5.19: Attachment in PBS: (a) PBS basin. **1**: disc inverter and **2**: cover slip with glued on mini pool. (b) cut trough attached disc on glass slide. **1**: disc inverter, **2**: PLL treated glass slide and **3**: wing disc. (c) inverted.

VII. transfer cover slip to aluminium frame

VIII. exchange PBS for WM1

IX. transfer to microscope

X. lower glass slide at cantilever end into WM1, just over wing disc

XI. start measuring software (sets current displacement and force as zero)

XII. attach second side by gently pressing down to cover slip

XIII. adjust height, such that glass slides are on same height

XIV. put wet tissues next to the set-up and cover set-up with cardboard box

XV. start imaging and measurement

5.3. Confocal Imaging

As described above the set-up was specifically built to enable laser confocal imaging of the wing disc during experiments. The laser that was used had a wavelength of 473 nm at nominally 100 mW which had reduced to 50 nW over time. At the object plane considerably less power is expected but good alignment of the optical components allowed approximately 300 µW to reach the fluorophores.
After some initial experiments with *DE-Cad::GFP* flies [65] most images were taken using *Trol::GFP/Lac::YFP* (PPTT-un1trol-GFP[G00022] ; PBac769.FSVS-1Lac-YFP[CPTI002601]) [66][67], crossed for me by Amarendra Badugu. In these flies green fluorescent protein (GFP) was expressed in the extracellular matrix (ECM) located at the basal side of the epithelial cells of the wing disc. [13] Additionally these flies incorporated yellow fluorescent protein (YPF) in lachesin (lac) in the septate junctions, which locate most strongly just beneath the adhesion belt along the cell membranes, like the lateral domain proteins (LDP). This meant that it could serve as a bright cell outline marker at the apical side, as well as a general cell marker since it also turned out to faintly label the cell membrane in general.

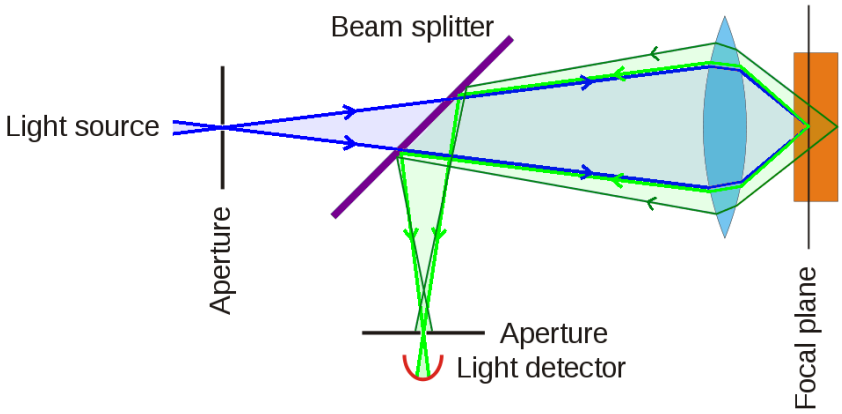

Figure 5.20: The simplified working principle of a confocal microscope.

Figure 5.20 shows a simplified version of the working principle of a confocal microscope. Light of one color is focused into a sample from where light of a different color is emitted, collected through the same lens, separated off the light path by use of a beam splitter, usually a dichroic mirror, and focused, usually by a different lens onto a pinhole behind which the light from this point on the sample is collected. Then the laser is scanned across the sample and the collected intensity is shown as the corresponding pixel brightness on the constructed image.
Figure 5.21 shows a cross section through a laser focus. It can be seen that the focal volume of the

[13] An overview of the parts of the wing disc has been given above in Section 1.1, see Figure 1.5.

laser is extended in z-direction and there are two big cone volumes above and beyond the focus that also have a high intensity of light. This will excite fluorophores outside of the focal plane. But by focusing onto the pinhole, light not coming from the focal plane will not pass through onto the detector.

Fluorescence imaging works by exiting a fluorescent protein, or rather an electron in the protein by the energy from the laser photon. The excited electron then loses some of its energy to vibrational modes before emitting another photon of longer wavelength and thereby returning to an energy near its initial state. This is illustrated in Figure 5.22.

The wavelength λ and therefore the color of the excitation light and the emitted light differ proportionally to the energy difference ΔE illustrated by the difference in length of the violet and green arrow in the Jablonski diagram in Figure 5.22, since: $E = h \cdot \nu$ and $\lambda = \frac{c}{\nu}$, with Planck's constant h, frequency ν, and the speed of light in vacuum c.

Figure 5.23 shows the excitation and emission spectra of the two used fluorophores GFP and YFP. For excitation of both fluorophores a 473 nm laser was used. Despite the low excitation probabilities, fairly good images could be acquired thanks to the high density of the used proteins and good quantum yield of GFP and YFP.

Separation of signals from two different fluorophores is usually done by spectral separation, see Figure 5.24. But since the two emission spectra have a lot of overlap, see Figure 5.25, complete spectral separation into two disjunct channels was not possible in this case.

Instead one pure GFP channel was set up in the Leica software, and one mixed channel. Resulting average intensity projections can be seen in Figure 5.26, Figure 5.26(b) clearly also contains 5.26(a).

After recording, the images were exported to Fiji [71] an open source image processing software used for post processing of microscopy data. In Fiji the images were normalized and slightly blurred and then the first channel (pure GFP) could simply be subtracted from the second channel (GFP-YFP-mixed). That this resulted in a good second image (pure YFP signal), was only possible due to the extreme brightness of the *Trol::GFP* in the ECM and actual, known-off, spacial separation of GFP and YFP.

Figure 5.27 shows the result of this subtraction. Now the overlay images, see Figure 5.28, could be used to study the apical cell areas seen in the YFP-images, see Section 6.4, as well as the overall geometry of the whole disc, see Section 6.3.

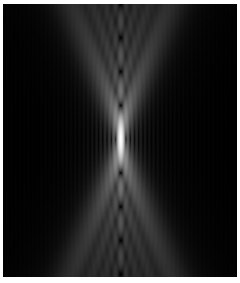

Figure 5.21: Simulation of a cross section of a laser beam focus [68].

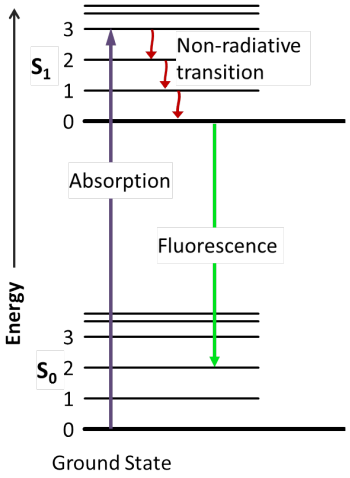

Figure 5.22: Jablonski diagram of fluorescence: energy states as lines, transitions as arrows [69].

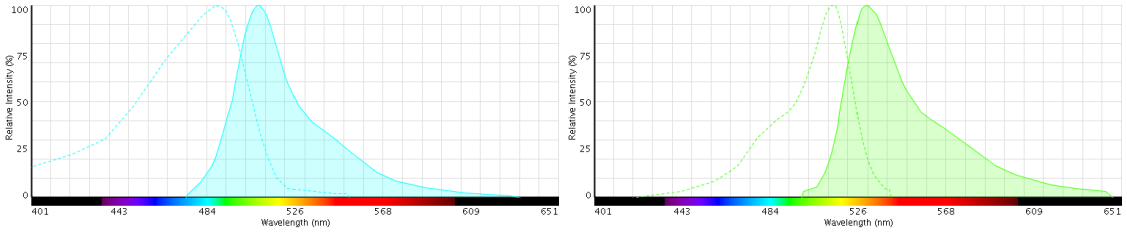

(a) (b)

Figure 5.23: Spectral plots of excitation and emission spectra of (a) GFP and (b) YFP [70].

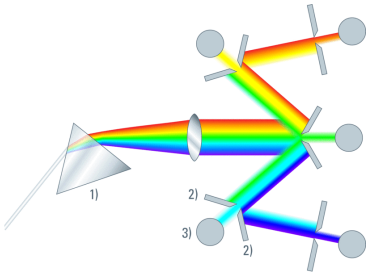

Figure 5.24: After passing through the pinhole the emission light from the fluorophores is usually spectrally separated first by using **1)** a prism and **2)** movable mirror sliders. These allow the spectrum to be split into sub spectra which are then recorded by **3)** photo-multiplier tubes.

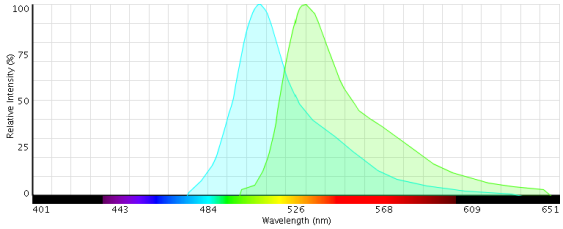

Figure 5.25: The emission spectra of GFP and YFP are overlapping. This makes separating the two usually difficult [70].

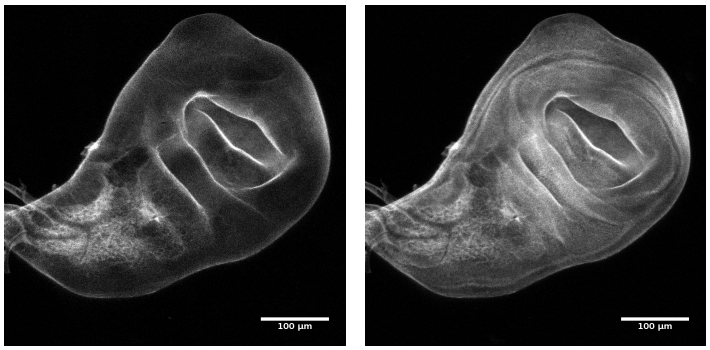

(a) (b)

Figure 5.26: Wing disc from a *TROL::GFP/LAC::YFP*-fly: average intensity projections from the signals of (a) channel 0, containing only signal from GFP and (b) channel 1, containing signal from GFP as well as from YFP.

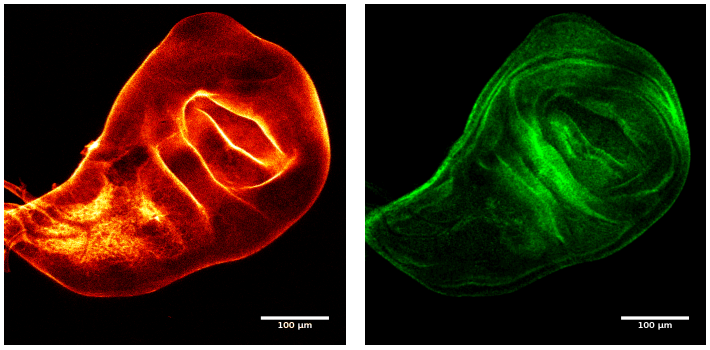

(a) (b)

Figure 5.27: False color images after filtering and subtraction (channel 1 - channel 0). (a) The *TROL::GFP* is colored bright red and (b) *LAC::YFP* is colored green.

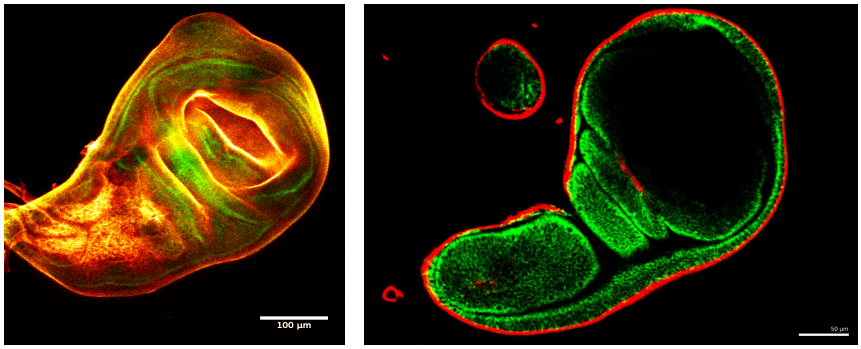

(a) (b)

Figure 5.28: This subtraction procedure results in good separation of the GFP- and YFP-signal. (a) shows the overlay from Figure 5.27(a) and 5.27(b), (b) shows a z-slice of a similar data set, where the spatial separation between green and red can be seen even more clearly. (Up left, a slice through the haltere disc can be seen.)

6. Measurements

Using the extensometer described in the previous section, different measurements were undertaken, yielding different observations. They can be categorized into four distinct categories, described in the following four sections: observations on the form of the force-displacement curve, Section 6.1, observations on the time dependence of the force-displacement characteristic, Section 6.2, observations on the 3-dimensional deformation of the tissue under load, Section 6.3 and observations on how this load might be transmitted through this 3-d geometry, Section 6.4.
The calculation of errors on displacement, force and time are described in Section 5.1.2. Typical uncertainties during measurements lay in the order of 1 µm to 10 µm for m_d and 0.1 µN to 1 µN for m_F. m_t was mostly negligible. The uncertainties are not presented in the plots shown in this section but are taken into account for all calculations that were done.
Also keep in mind when looking at the plots, that the last letter in the filename gives the mode of measurement. **H** stands for "harmonic excitation" and **L** for "linear increase with time".

6.1. On Non-linearity

Already the first few measurements, after debugging, testing and calibration of the new set-up, made it clear that the wing disc could not be described as a simple Hookean spring with fixed Young's modulus. This was contrary to what was previously reported in [39], but is deducible from measurements of Poisson's ratio made and described by the same author later on, in [72].

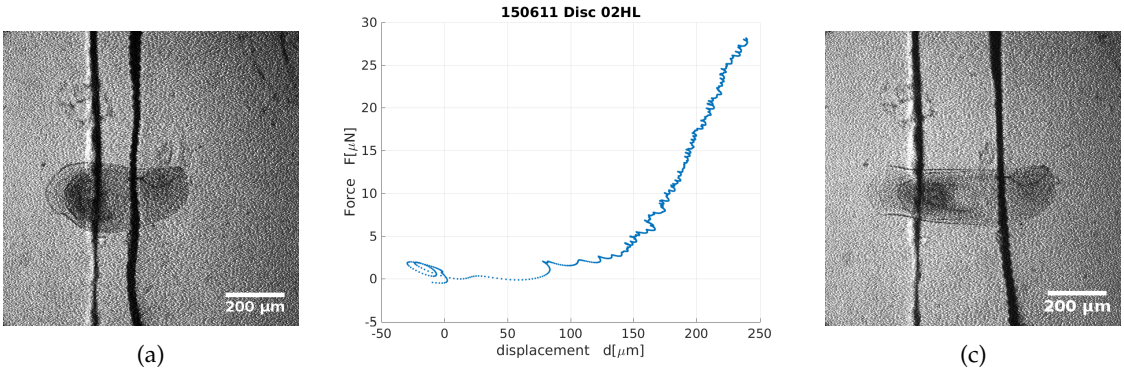

(a) (b) (c)

Figure 6.1: Disc stretched on 11.06.2015 using linear increasing force over time (a) shows the disc in a the state at $d \approx 0\,\mu m$, (b) shows the force-displacement curve and (c) shows the disc in the stretched state at $d \approx 200\,\mu m$.

Figure 6.1 shows a measurement using linearly increasing force over time with a gradient $\beta = \frac{F}{t} = 0.1\,\mu N/s$. 6.1(a) shows the transmission channel image from the inverted Leica SP1 where $d \approx 0\,\mu m$. 6.1(b) shows the recorded force-displacement curve. It is evident that the recorded curve can not be described by a straight line. On the contrary this measurement looks like the initial slope at the relaxed state is vanishing. This would mean a vanishing Young's modulus at the rest configuration.
6.1(c) shows the stretched disc at $d \approx 200\,\mu m$, notice that the disc is now almost exactly 150% of its initial total length, while the two glass slides have moved apart almost 500%. Careful examina-

tion of Figure 6.1(c) shows that the point of attachment does not exactly coincide with the end of the glass slide, meaning that the actual elongated material is more than what is between the glass slides, but still less than the total disc, therefore this equates to a material elongation somewhere between 150% and 500%. An observation to which we will come back.

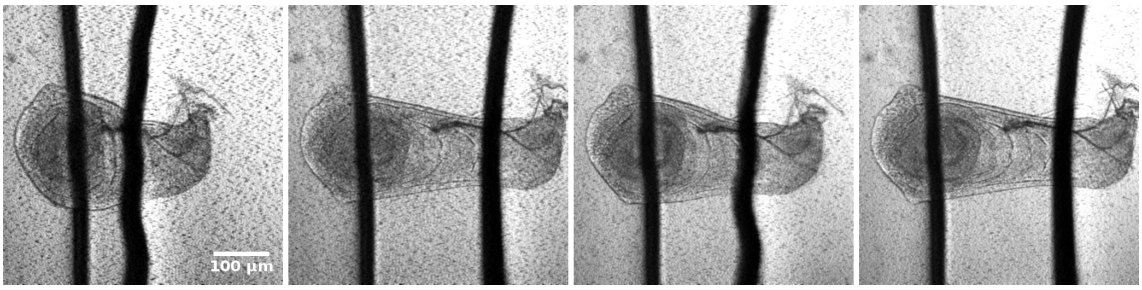

Figure 6.2: Montage showing the wing disc in the relaxed state at $F \approx 0\,\mu N$, at $F \approx 25\,\mu N$ again at $F \approx 0\,\mu N$ and $F \approx 25\,\mu N$, showing no full recovery to $d = 0\,\mu m$.

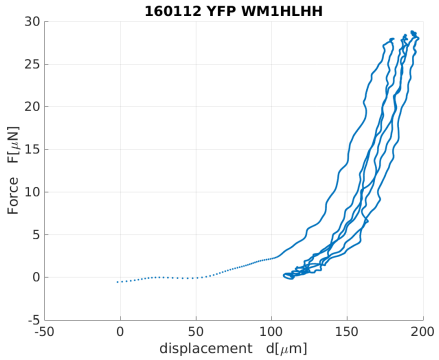

Figure 6.3: Amplitude $A_F = 20\,\mu N$, frequency $f = 0.005\,Hz$, offset $F_c = 20\,\mu N$

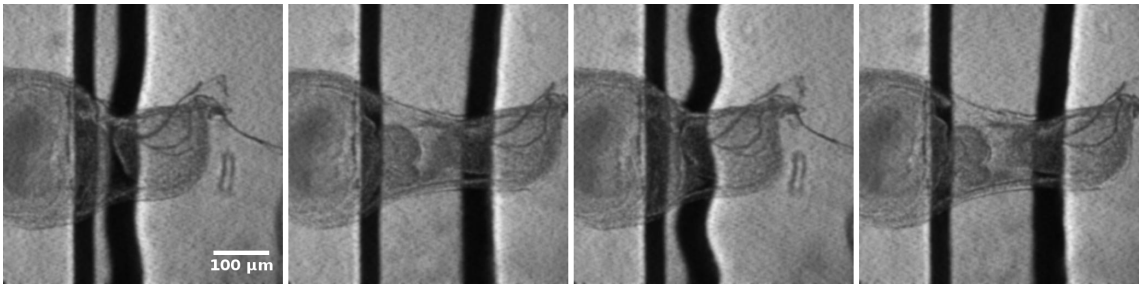

Figure 6.4: Montage showing the wing disc in the relaxed state at $d \approx 0\,\mu m$, at $d \approx 125\,\mu m$ again at $d \approx 0\,\mu m$ and $d \approx 125\,\mu m$, showing full recovery.

To probe whether the initial slope is really zero, harmonic excitation was used, first with control of F while measuring d, see Figure 6.3, but given the convex nature of the curve, it was much easier to access this lower part of it using control of d while measuring F [14]. Figure 6.5 shows such a measurement revealing a tiny slope of about $0.02\,N/m$.

[14] As described in Section 5.1.2 both modes of operation were implemented but after this point in time only d-control and force measurement was used.

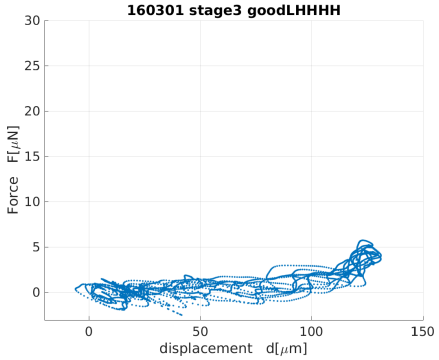

Figure 6.5: Amplitude $A_d = 62.5\,\mu\text{m}$, frequency $f = 0.01\,\text{Hz}$, offset $d_{fix} = 72.5\,\mu\text{m}$

Given the uncertainty in placement and attachment of different discs, absolute displacement values are not comparable 1-to-1. So when using multiple samples and measurements, a scaling length d_0 needs to be ascribed to each measurement, such that relative displacements d/d_0 can be compared. Since the real-world length of actually stretched material is hard to estimate, this parameter was adjusted in the reasonable range between $80\,\mu\text{m} \lesssim d_0 \gtrsim 180\,\mu\text{m}$ such that the different measurements fell on top of each other.

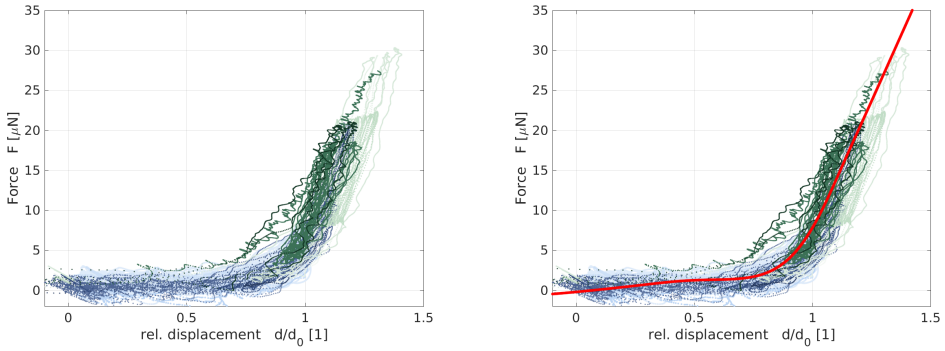

(a) (b)

Figure 6.6: 15 individually scaled measurements, collapsing nicely to a part-wise affine function, as can be seen from the shown spline fit. $d_0 \approx 140\,\mu\text{m}$.

Figure 6.6(a) shows 14 harmonically driven measurements and one with linear increase in force over time, from seven different discs. As can be seen the data nicely collapse when scaled properly. Figure 6.6(b) shows a spline fit through these data.
The scaling with d_0 effectively turned the displacements d into dimensionless strains ε. Now to transform the measured forces F into stress σ, they have to be scaled with the cross sectional area S_{WD}. Again this is hard to estimate individually. But to get an idea of the order of magnitude, the generic wing disc dimensions given in Section 1.1 were used with $S = 100\,\mu\text{m} \times 300\,\mu\text{m} = 3 \cdot 10^{-8}\,\text{m}^2$.
Since the slope of the curve in Figure 6.6(b) obviously changes quite dramatically, technically the slope of the stress-strain curve is not Young's modulus but is called the tangent modulus. This is plotted in Figure 6.7(a) as a function of strain and in 6.7(b) as a function of stress. Clearly two affine parts with tangent moduli around $E_a \approx 100\,\text{Pa}$ and $E_b \approx 2200\,\text{Pa}$ can be distinguished. The affine increase in E as a function of σ in the transitional part indicates exponential behavior $\sigma \propto e^{\varepsilon}$

in this region.

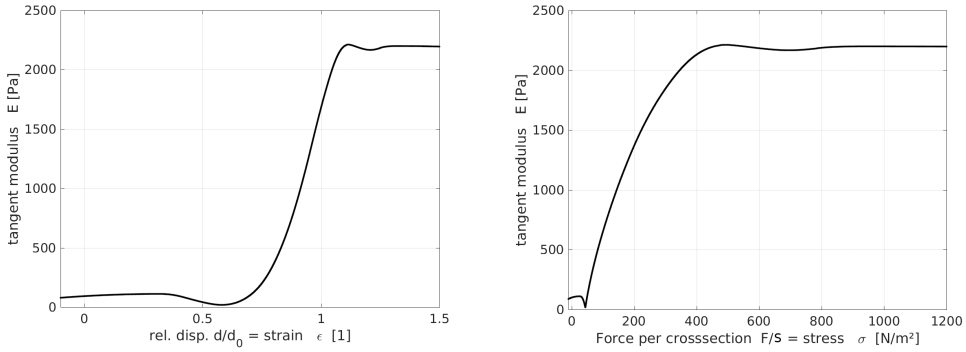

(a) (b)

Figure 6.7: Plotting the scaled slope of the fit from 6.6(b) reveals two affine parts of constant tangent modulus and an exponential crossing, as can be deduced from the affine behavior of $E(\sigma)$.

Measured	moduli
$E_a \approx$	100 Pa
$E_b \approx$	2200 Pa

Table 6.1: The measured values for the two parts of constant tangent modulus.

In the language of force and displacement these moduli would be interpreted as regions with different stiffness a and b in N/m and would correspond to the following values:

Measured	stiffness
$a \approx$	0.02 N/m
$b \approx$	0.5 N/m

Table 6.2: The measured values for the two parts of constant stiffness.

6.2. On Rheology

In addition to the observations described in the preceding section, the evolution of ε and σ over time are needed in order to uncover the fitting descriptive rheological model, see Section 3. For this different approaches were tried.
First, since it is a fairly complete visco-elastic model, it was attempted to fit Burgers model to the data. For this, measurements with harmonic excitation in F were chosen, since the instantaneous jump from $F = 0$ N to some constant value F_c, as used in the theoretical discussion in Section 3, is infeasible experimentally. Therefore the model had to be solved for harmonic excitation [15].

[15]For scaling the generic values $S = 3 \cdot 10^{-8}$ m^2 for the cross section and $d_0 = 140$ µm for the rest length were used.

Starting from a simplified notation for Equation (15), Burgers model is described by:

$$\sigma + a_1 \ \dot{\sigma} + a_2 \ \ddot{\sigma} \ = \ b_1 \ \dot{\varepsilon} + b_2 \ \ddot{\varepsilon} \ , \tag{22}$$

where $a_1 = \tau_1 + \tau_2 + \frac{\eta_2}{E_1}$, $a_2 = \tau_1\tau_2$, $b_1 = \eta_2$ and $b_2 = \tau_1\eta_2$.
Now

$$\sigma(t) = A_\sigma \ e^{i\omega t} + C \ , \tag{23}$$

with amplitude $A_\sigma = \frac{A_F}{S}$, $\omega = 2\pi f$, $C = \frac{F_c}{S}$ and $t = t_{exp} + \frac{\pi}{\omega}$ to account for the fact that the measurements start with $F(t = 0) = 0\,\text{N}$.
One can solve the homogeneous part

$$\begin{aligned} \ddot{\varepsilon} &= -\frac{b_1}{b_2}\dot{\varepsilon} \\ \varepsilon &= \varepsilon_0 \cdot e^{-\frac{b_1}{b_2}t} \ , \end{aligned} \tag{24}$$

where ε_0 is a fit parameter, as explained in Section 3.1.
For the inhomogeneous part the following ansatz was used:

$$\varepsilon(t) = B \ e^{i\omega t} + Dt + \varepsilon_{free} \ , \tag{25}$$

where ε_{free} is free and represents the fact, described in Section 3.2, that Burgers model does not have a fixed rest configuration, since it inherently describes liquid-like materials.
Inserting (23) and (25) into (22) one can find:

$$D = \frac{C}{b_1}$$

and

$$B = \alpha - i\omega\beta$$

with

$$\alpha = \frac{A_\sigma(a_1b_1 + a_2b_2\omega^2 - b_2)}{b_1^2 + b_2^2\omega^2}$$

and

$$\beta = \frac{A_\sigma}{\omega^2}\left(\frac{b_1(1 - a_2\omega^2) + a_1b_2\omega^2}{b_1^2 + b_2^2\omega^2}\right)$$

adding the homogeneous part and only looking at the real part one arrives at

$$\mathfrak{Re}(\varepsilon(t)) \ = \ \varepsilon_0 e^{-\frac{b_1}{b_2}t} \ + \ \alpha\cos(\omega t) \ + \ \omega\beta\sin(\omega t) \ + \ \frac{C}{b_1}t \ + \ \varepsilon_{free} \ . \tag{26}$$

From this one can substitute a_1, a_2, b_1, b_2 to arrive at a formula of $\varepsilon(t) = \frac{d(t)}{d_0}$ which can be passed to the computer to fit E_1, τ_1, E_2, η_2, ε_0 and ε_{free}.

$$\begin{aligned} \varepsilon(t) \ = \ & \varepsilon_0 \cdot e^{\frac{-t}{\tau_1}} \ + \ A_\sigma \cdot \left(\frac{1}{E_2} + \frac{1}{E_1 \cdot (1 + \tau_1^2 \cdot \omega^2)}\right) \cdot \cos(\omega \cdot t) \ + \ ... \\ & \frac{A_\sigma \cdot \omega}{\eta_2} \cdot \left(\frac{\eta_2}{E_1} \cdot \frac{\tau_1}{1 + \tau_1^2 \cdot \omega^2} + \frac{1}{\omega^2}\right) \cdot \sin(\omega \cdot t) \ + \ ... \\ & \frac{C}{\eta_2} \cdot t \ + \ \left(\frac{C}{E_2} + \varepsilon_{free}\right) \end{aligned} \tag{27}$$

Note that here the substitution for A_σ, C, ω and t were not made. These were carried out separately from the fit.
Figure 6.8(a) shows such a fit. It shows as functions of time: in red the measured force data in µN that was PID-controlled to produce a sinusoidal excitation with amplitude $A_F = 10\,\mu N$ at a constant offset $F_c = 20\,\mu N$ at a frequency $f = 0.05\,Hz$, in blue the measured displacement response. The black line shows a fit for the sine. This was done because the PID sometimes could not produce exactly what was desired, especially the real amplitude would often be less than the desired one. Here the fit found: $A_{fit} = 6.7\,\mu N$, frequency $f_{fit} = 0.05\,Hz$, offset $F_{c,fit} = 14.2\,\mu N$. The red line shows the fit of Equation (27) to the displacement data, using the results from the fitted sine as input.
Note that, while the measurement starts at zero force, the fitted sine does not. This can be seen more clearly when looking at Figure 6.8(b), where the measured force is plotted against the displacement in black and the blue line shows the harmonic fit. So this is not a shortcoming of Burgers model.

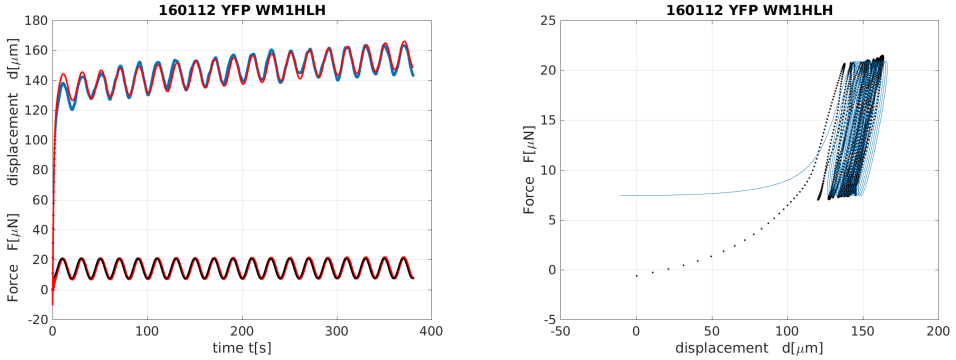

(a) (b)

Figure 6.8: Amplitude $A_F = 6.6\,\mu N$, frequency $f = 0.05\,Hz$, offset $F_c = 14.2\,\mu N$.
Fitted parameter: $E_2 = 4800\,Pa$, $\eta_2 = 1 \cdot 10^6\,Pa\,s$, $E_1 = 1 \cdot 10^4\,Pa$, $\tau_1 = 1.7\,s$, $\varepsilon_0 = -100$ and $\varepsilon_{free} = 0.83$.

Here the fit follows the data, yielding the following mechanical parameters:

Burgers		model	Parameter
E_1	=	$1 \cdot 10^4$	Pa
η_1	=	$1.7 \cdot 10^4$	Pa s
E_2	=	4800	Pa
η_2	=	$1 \cdot 10^6$	Pa s
ε_0	=	-100	
ε_{free}	=	0.83	

Table 6.3: The fitted mechanical parameters of Burgers model to the harmonically stretched wing disc.

So the two Young moduli seem reasonable and the viscosity η_2 is close to the one from pitch, measured in the famous experiment at the University of Queensland [73], meaning the material behaves manly as solid. The negative ε_0 simulates the exponential creep before the first stretch,

but this will not work when strain returns to zero. Therefore the model is expected not to be able to follow the non-linear stress-strain curve back to the lower part after the first extension.

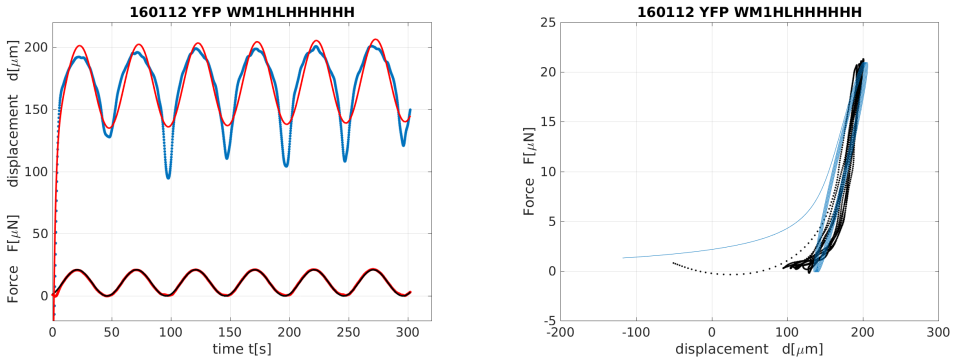

(a) (b)

Figure 6.9: Amplitude $A_F = 10.5\,\mu N$, frequency $f = 0.02\,Hz$, offset $F_c = 10.4\,\mu N$.

Figure 6.9 further supports this. In (a) one can clearly see that the fit does not follow the measured displacement and (b) shows the strictly affine behavior of Burgers model after the initial stretch. Here the targeted amplitude was set to $A_F = 15\,\mu N$ at a constant offset $F_c = 12\,\mu N$ at a frequency $f = 0.02\,Hz$. This was with pre-knowledge of the system and produced a forcing that returned almost to zero on each cycle with the real $A_F = 10.5\,\mu N$ and offset $F_c = 10.4\,\mu N$. The parameters of the shown fit are:

Burgers		model	Parameter
E_1	=	2800	Pa
η_1	=	5500	Pa s
E_2	=	2900	Pa
η_2	=	$5 \cdot 10^5$	Pa s
ε_0	=	-1000	
ε_{free}	=	1	

Table 6.4: The fitted parameters for the measurement shown in Figure 6.9, that proved Burgers model can not reproduce the most striking feature of the measured stress-strain behavior of the wing disc: it's extreme non-linearity.

While all data to which Burgers model was fitted yielded parameter values in a similar overall range, clearly this model can not reproduce the most striking feature of the measured stress-strain behavior: the extreme non-linearity. This should not come as a huge surprise, since, while being fairly complete in describing visco-elastic properties, all elements of the model are linear, therefore also their combination will always stay linear.
This is why Burgers model was abandoned and instead of directly fitting a model, the time domain behavior of $F(t)$ at constant displacement d_{fix} was investigated more closely. Figure 6.10 shows the force relaxation over time at fixed displacement $d_{fix} = 140\,\mu m$. The red curve is a two-component exponential decay with offset. The two relaxation times corresponding to the two components are $\tau_1 \approx 100\,s$ and $\tau_2 \approx 1000\,s$.
Note that there might be a third, shorter time $\tau_0 \approx 10\,s$, as was previously observed by imaging

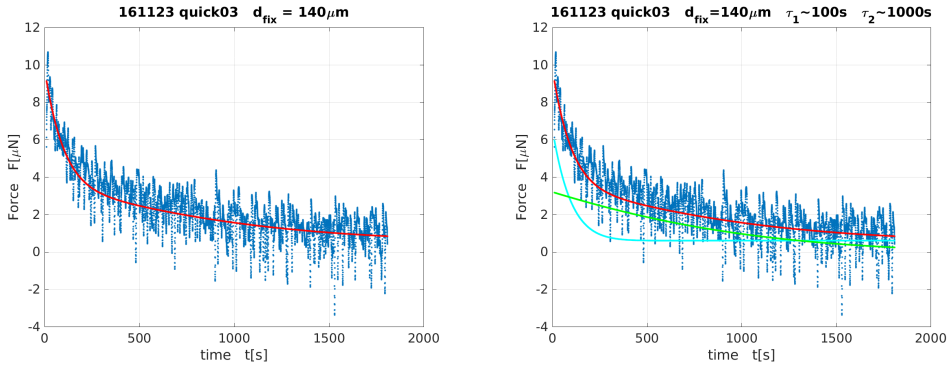

(a) (b)

Figure 6.10: Constant displacement $d_{fix} = 140\,\mu m$, revealing two component force-relaxation over time.

retracting discs after stretching and sudden debonding of one end of the discs [72], however this time scale is not observable using this method because the displacement d_{fix} can not be reached infinitely fast and so the first few seconds can not be analyzed rigorously.
These measurements, together with the ones about the non-linearity of the stress-strain curve, built the basis for a new model to describe the one-dimensional force-displacement behavior of the wing disc that is presented in Section 7.

6.3. On Geometry

After realization that the measured force-displacement data is not fitted well, using conventional visco-elastic models, the process of stretching the wing disc was observed more closely.
The disc is not a homogeneous block of material. Figure 1.6(b) showed how strongly folded the material is. And it was speculated that the observed extreme non-linearity of the stress-stain curve could come from first unfolding these folds and subsequent stretching of the material itself. To investigate this, three-dimensional image data of the disc during stretching was required. This is why the set-up was built on-top of a confocal microscope and the *Trol::GFP/Lac::YFP*-flies were chosen, in order to have distinguishable signal from the apical- as well as the basal-side of the cells. Figure 6.11 shows again how the disc was positioned in respect to the microscope object shown at the bottom.
This means that the peripodial membrane (PM) as well as the apical side of the disc proper can be imaged quite clearly. But less laser light will reach the basal side of the disc proper, exciting less fluorescence which then also has to travel back through the disc, the gap of medium, the cover slip and the immersion liquid without scattering, in order to be recorded by the confocal microscope.
The recorded image-data was post processed as described in Section 5.3 and then transferred to MorphoGraphX, an open source application for the visualization and analysis of 4-d biological data sets [74].
Figure 6.12 shows the *Lac::YFP* channel data from such a stretching-and-imaging experiment [16].

[16] Given the age of the microscope used, to record such a stack of approximately $1024 \times 1024 \times 500$ points took on the order of 30 min.

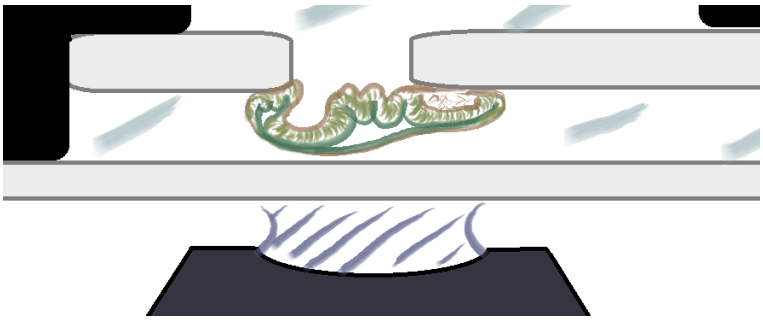

Figure 6.11: The wing disc is glued to the underside of two glass slides at such a height as to be as close as possible to the cover slip through which imaging takes place, while not touching it which would distort the force measurements.

They are turned, as if the whole experiment were done up-side-down, since this is usually the way one looks at the discs; pouch-up. In blue the unstretched disc is shown and in yellow the same disc at displacement $d_{fix} \approx 150\,\mu m$ can be seen.

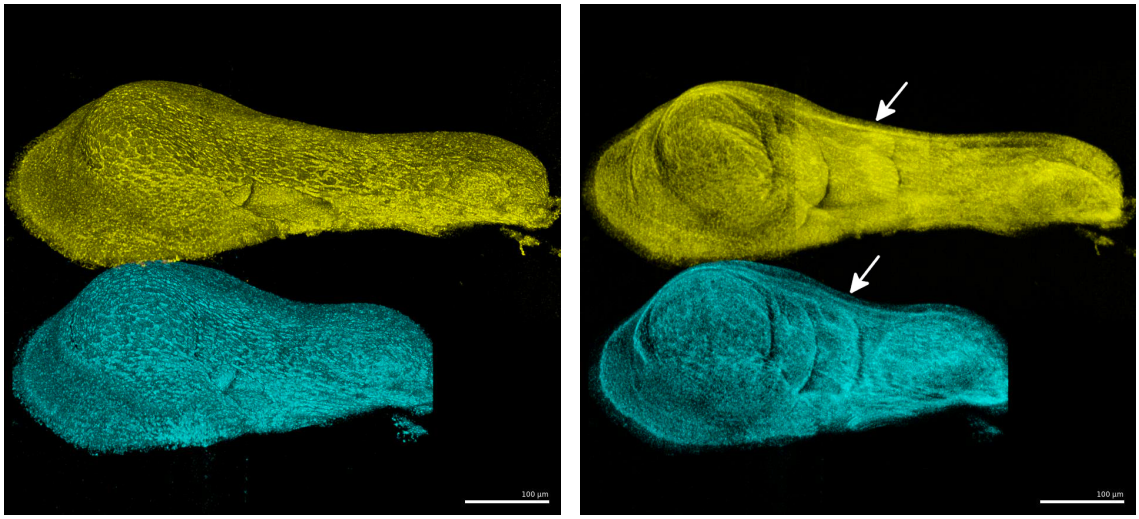

(a) (b)

Figure 6.12: 3-dimensional reconstructed *Lac::YFP* data of a wing disc, unstretched in blue, stretched in yellow. In (a) the peripodial membrane can be seen and individual cells can be distinguished, in (b) the stack is made semi-transparent in order to see the disc proper. The scale bar is 100 µm.

In Figure 6.12(a) the PM can be seen and individual cells therein can clearly be distinguished. Here also one can see a hole, cut or rip in the PM, probably due to accidental contact during dissection. The PM clearly gets strained over the full length of the disc.
Figure 6.12(b) shows the same data using the possibility of MorphoGraphX (MGX) to make the data semi-transparent. Now the disc proper is visible and it can be seen clearly that most of the elongation of the disc happens in the hinge region, where the folds are, indicated by the white arrows in the figure. This could already be seen from simple transmission images, but having the full 3-d stack allows one to now look at the cross sections.
Figure 6.13 shows the cross section of a disc before stretching and at a displacement of $d_{fix} =$

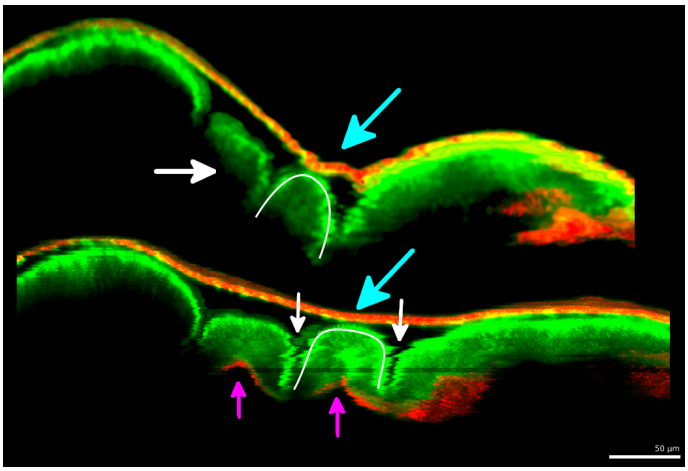

Figure 6.13: False color image of the cross section of a wing disc before and in stretching, ECM in red, cell-bodies in green. The scale bar is 100 µm.
$d_{fix} = 100\,\mu m$, $F_{ini} = 21\,\mu N$ to $F_{final} = 11\,\mu N$.

100 µm. ECM is represented in red and the cell-bodies in green. The scale bar corresponds to 50 µm and the measured force decayed, as described above, double-exponentially from initially $F_{ini} = 21\,\mu N$ to $F_{final} = 11\,\mu N$ after approximately 30 min at the end of image recording. So the acting force decays for the slices shown in the image from top to bottom but the position stays the same.
As described on page 47, the lower ECM is hardly visible, especially in the unstretched disc, see big white arrow in Figure 6.13.
The small vertical white arrows indicate the folds on the apical side. They have opened up a bit, compared to the upper image, but they have not completely unfolded. Obviously the PM is a lot straighter, see cyan arrows in the figure, and the basal side of the folds, magenta arrows, seem to open much more prominently than the apical side. Here the top part of the fold seems to flatten from a smooth dome-like form to something with more pronounced corners, as indicated by the white line along the apical side of the second fold. This could be an indication of some additional mechanical connection over the folds, through the lumen. Or it could mean the PM pushes down onto the folds.
Figure 6.14 shows more data, where more images were acquired, at rest and at four different displacement-positions: $d_0 = 0\,\mu m$, $d_1 = 50\,\mu m$, $d_2 = 100\,\mu m$, $d_3 = 150\,\mu m$ and $d_4 = 200\,\mu m$. 6.14(a) shows the view from the top, 6.14(b) the cross section in the direction of elongation and 6.14(c) shows the measured force, first as a function of time in red, and then as function of displacement.
Now we can see clearly that also at higher forces, the folds are not simply straightened as-if unfolding a worm-like structure with uniform thickness. Rather the cells themselves seem to vary in height in addition to the tissue being folded up a bit. Figure 6.16 shows a drawing of the proposed idea.
Next it was attempted to record even more of the dynamics of the process so an extremely slow, linear displacement gradient over time was started and as many full stacks recorded as possible. Figure 6.15 shows four frames taken out of the 15 totally recorded, representing similar points on the force-displacement curve as the ones in Figure 6.14. The full set is reproduced in appendix B Figure B.1.

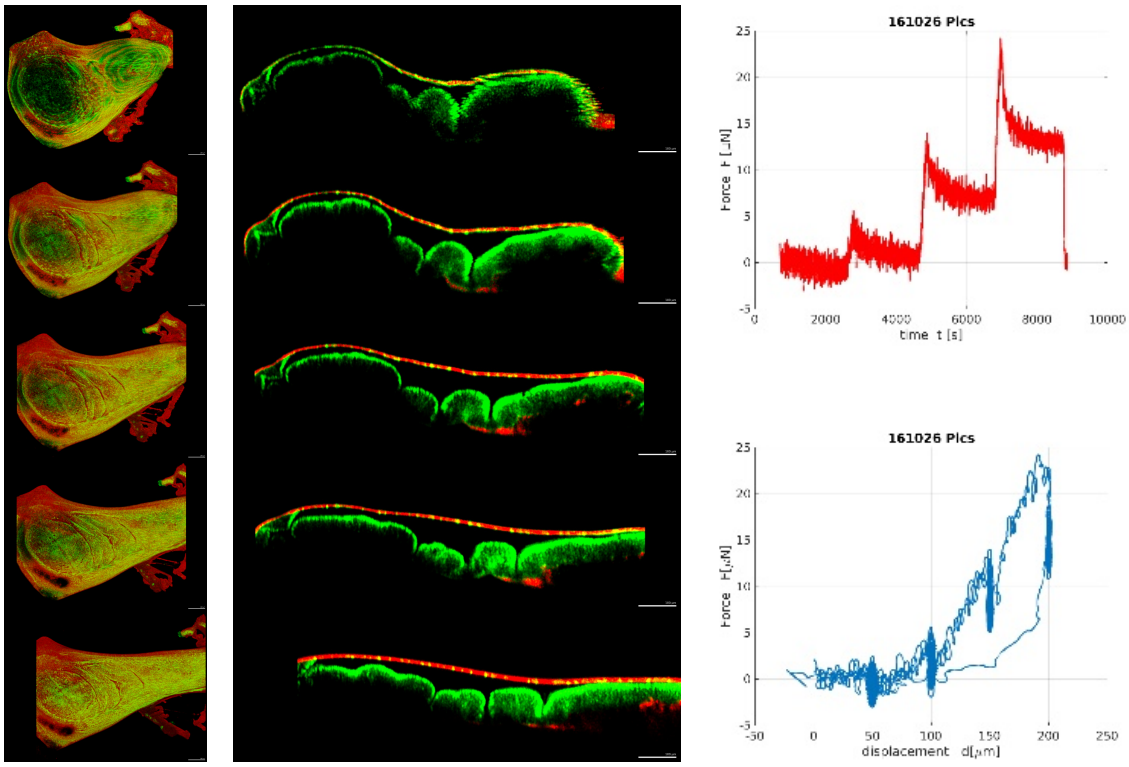

(a) (b) (c)

Figure 6.14: Montage of a stepwise displacement and imaging. (a) top view, (b) y-cross-section, (c) force data as function of time and of displacement. The scale bar is 100 µm.

This measurement reproduced the previous findings very accurately. Here the lower ECM can be seen a bit better than in the previous data and it seems to end up in a fairly straight line in 6.15(d). Additionally I included the orthogonal cross section through the wing pouch where one can see that the initial high dome starts to buckle. Also along the direction of pull there seems to be some buckling happening at later stages of pulling. The big jump in force, seen in Figure 6.15(d) (and B.1(m)), is due to partial debonding at the notum end.
To conclude, the 3-dimensional geometry of the wing disc is fairly complex, even though it is normally described as a simple, flat, cellular monolayer of columnar cells.
The intricate layout of folds, or furrows and domed sections allows global movement without the need for actual unfolding. In addition to this it can be asserted that the peripodial membrane (PM) gets stretched to a clearly observable extent.
In the next section the question "where inside the wing disc is the stress is actually carried?" shall be investigated.

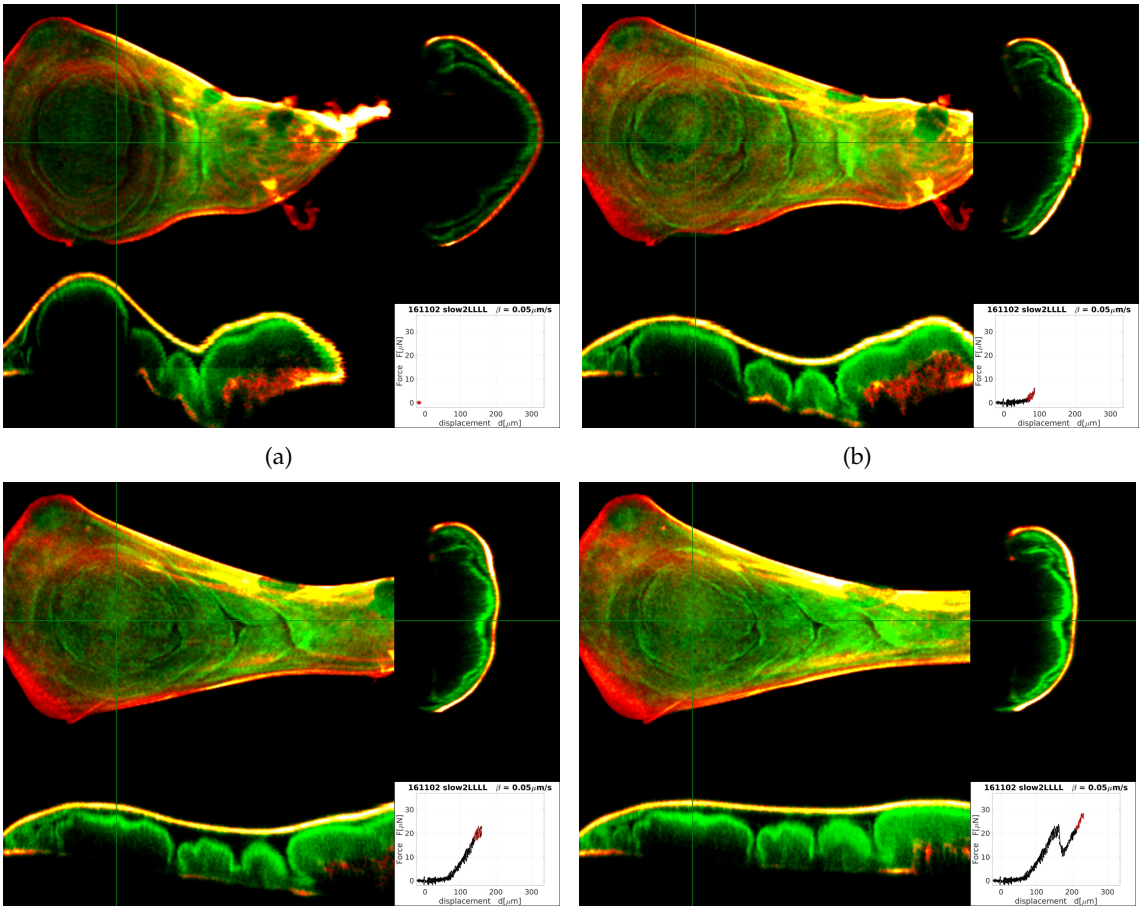

Figure 6.15: Subset of a continuously recorded 4-d data set. In the upper left portion a z-projection of the image data is shown right and below a x- and y-cross-section is shown. In the lower right corner the recorded force-displacement curve is plotted, see appendix B for bigger reproductions with better readability.

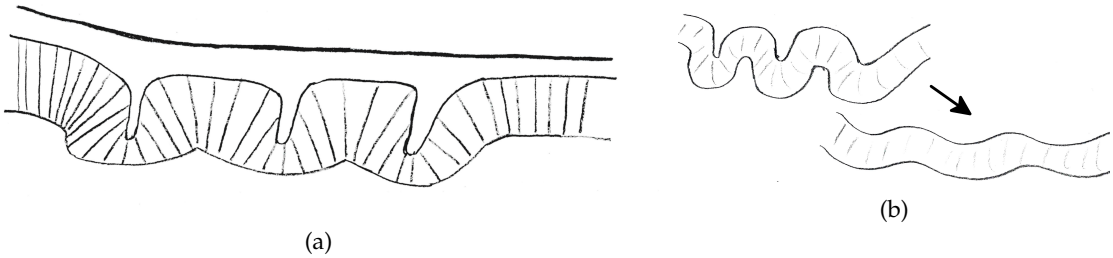

Figure 6.16: (a) Drawing of the proposed variation in cell height in the folds; left would be the wing pouch, and far right the notum region. (b) in contrast: had all cells the same height, the folds would unfold much like a worm that got stretched.

6.4. On internal Stress Distribution

The images from Figure B.1 were used to measure the length of: the lower ECM, the apical side of the disc proper and the PM. Figure 6.17 shows these line-length measurements over the 15 frames, normalized to the length in frame 2, which is considered to be closest to the rest position. It should be noted that it is extremely difficult to find landmarks in the images to base these measurements on. The presented data are mean values from several measurements along different parts of the three components.

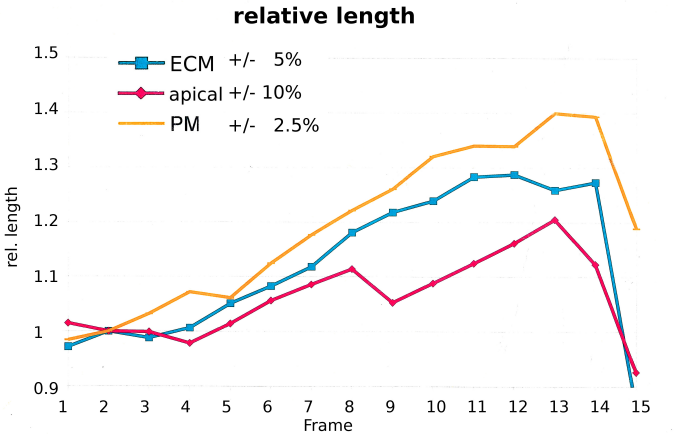

Figure 6.17: Relative line-length along the ECM (blue), the apical side of the disc proper (magenta) and the PM (orange). While the PM shows the most strain, the curve for the apical side resembles the measured force curve the closest, but has the highest uncertainty.

While clearly all these parts get elongated, two things can be noted: one, the PM seems to take the most strain, and two, the curve for the apical side seems to resemble the curve for the measured force-displacement curve closest, starting to increase after frame 4 ((e) in B.1) and also including a drop from frame 8 to 9 ((i) to (j) in B.1) as well as between frame 13 and 14, ((m) to (n)). But for the apical side it was the most difficult to get consistent measurements and in some parts, like the actual pouch, no strain at all was measured.
So to assume that these measurements show that the apical side of the cells in the disc proper is the primary force bearer in the tissue, with the PM being of lower stiffness as well as the ECM not playing the mayor role in force transduction, would be tempting. But deeper investigation into the strain distribution should be undertaken first.

In a next step the PM was chosen to investigate how the global strain affects the individual cells. The PM was chosen for two reasons, firstly for the high strain within the PM, secondly for feasibility. While cells in the disc proper and especially the wing pouch get imaged and segmented routinely now. It has to be stressed that for this the disc normally gets pressed flat against the cover slip and/or fixated and cleared. Figure 6.18 shows an example of a disc sandwiched between two cover slips as is common for imaging. And while the top view looks extremely nice [17], the cross section reveals the huge discrepancy between the hitherto shown wing discs and this one. It should be noted however that the proposed cell architecture, see Figure 6.16, is further

[17] One can clearly see the dividing cells that have brought their nuclei to the apical side and therefore have an area double that of the other cells.

supported by this cross section.

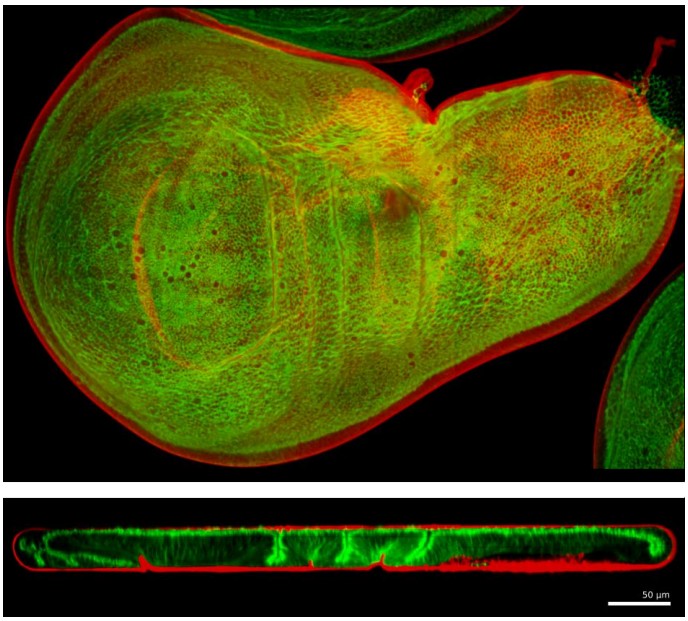

Figure 6.18: Normal mode of imaging a wing disc: pressing it flat against the cover slip produces nice picture of apical surface, but severe deformation can be seen in the cross section. The scale bar is 50 µm.

Such image stability is impossible when keeping the disc freely suspended. But the much bigger cells in the PM can often still be resolved. So Figure 6.19 shows the cells in the PM (left in cyan) before stretching and (right in yellow) at displacement $d_{fix} \approx 190\,\mu m$ at $F_c \approx 9\,\mu N$ [18]. The cells are colored with the same color in both cases, where the color indicates the area increase from cyan to yellow, deep blue corresponds to no increase or even slight area loss and cyan, yellow to red indicates area increase of 1.3 up to 2 [19]. In each cell center an orange line is placed, indicating the principal direction of strain. Close examination shows that, while most cells do follow the direction of external pull in their elongation, some even contracted in this direction, showing slight elongation in the orthogonal direction.
The image analysis was done in MorphoGraphX using the real projected area onto the strongly curved surface. For the PDG calculation a MATLAB script was written and the results were reloaded into MGX.
As can be seen, not all cells get strained the same amount, some, especially near the center of the pouch and slightly towards the hinge region actually decrease in size while the cells at the periphery get elongated the most.
Figure 6.20 shows the PM-cells color-coded with their area at rest and two stages of stretching [20], at $d_0 \approx 0\,\mu m$, $d_1 \approx 150\,\mu m$, $d_2 \approx 200\,\mu m$ and $F_0 \approx 0\,\mu N$, $F_1 \approx 5\,\mu N$, $F_2 \approx 10\,\mu N$.
Here the overall cell-size-increase is better visible. And it can be stated that external global straining does translate to local cell-area increase, albeit not uniformly. There are areas of higher strain and such with lower strain. And individual cells react somewhat individually.

[18] Data 150729

[19] I apologize again for the use of jet as colormap, unfortunately it can not be changed in MGX, jet.

[20] Data 160629

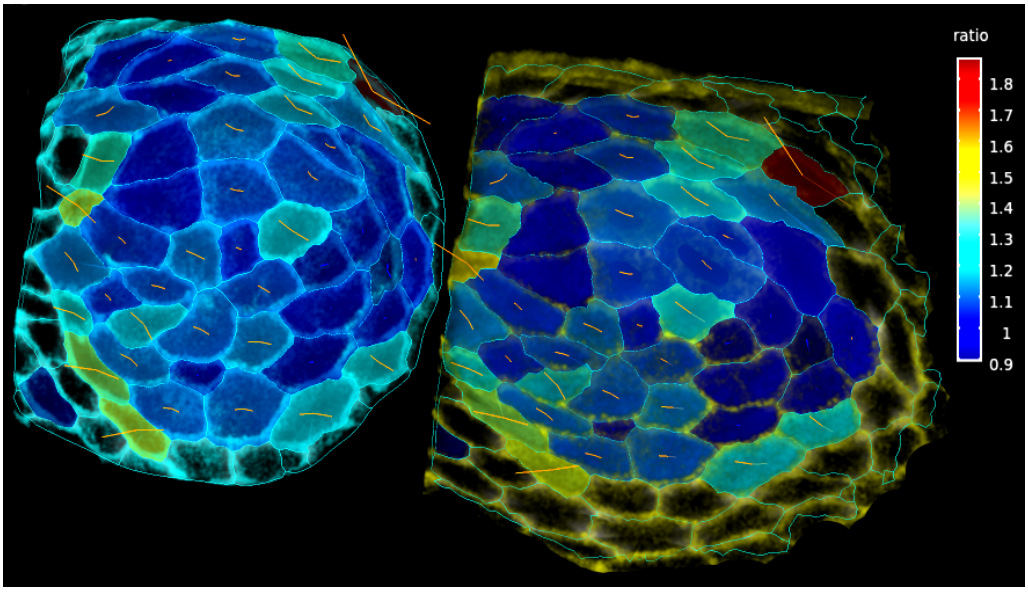

Figure 6.19: Cell area increase in the PM cells upon stretching to $d_{fix} \approx 190\,\mu m$ at $F_c \approx 9\,\mu N$. The orange line represent the principle direction of elongation.

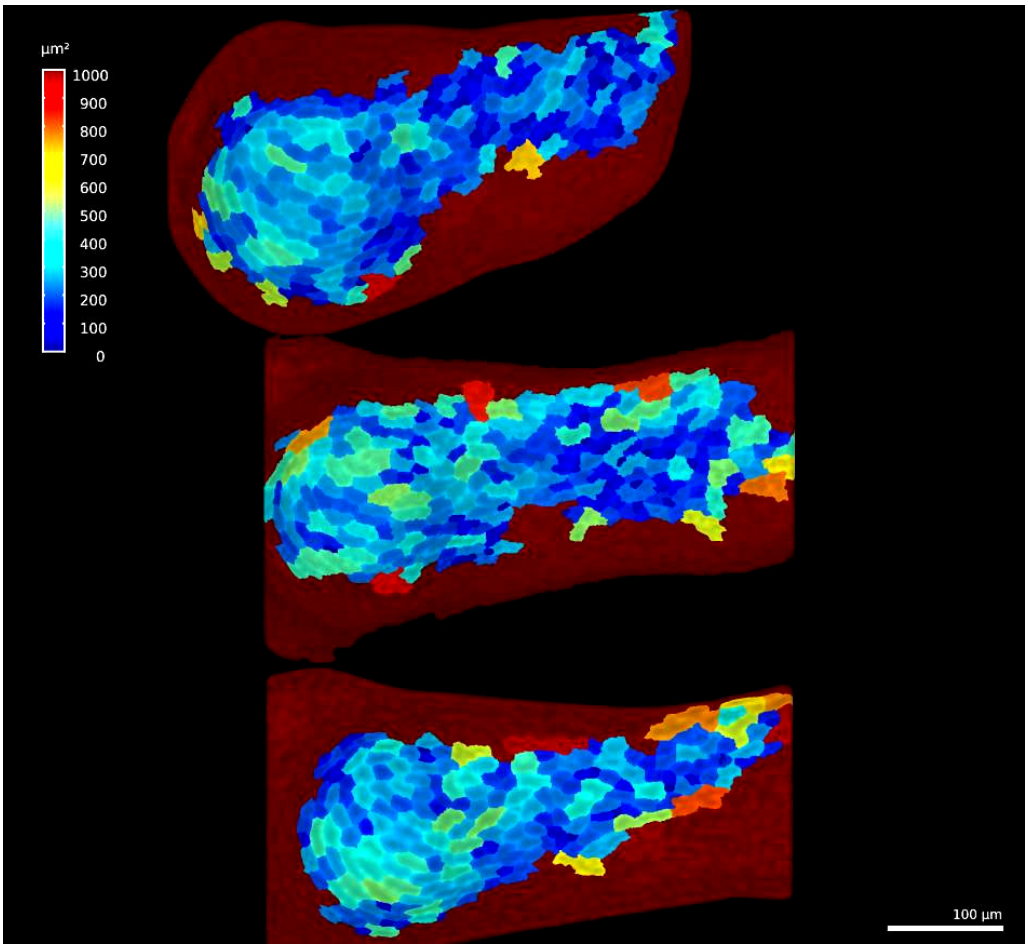

Figure 6.20: Cell areas of the whole PM upon stretching. The scale bar is 100 µm.

Part III.

7. Results: Descriptive 1-d Rheological Model

In this section I will present the main result from the explorative process described so far, namely the rheological model that describes the emerging macroscopic force-displacement behavior of the wing imaginal disc of the late third instar *Drosophila melanogaster* larva. It will not be presented in the form of stress and strain, since it is not believed to describe a homogeneous block of material. Rather the measured force in µN, displacement in µm and hence stiffness in N/m and relaxation times τ in s are used directly.
This in itself is considered to be an important result of this work: That the intricate 3-d geometry plays an important and non-negligible role in the discussion about forces in tissues, especially when talking about external forcing. But also within the tissue, curvature and differences in cell-height might well play an important role in determining the chains of force transduction.

From the measurements presented in Section 6.1, it can be deduced that the force-displacement characteristic of the wing disc should incorporate two affine parts, with an exponential crossover. This is described by a smooth step function, akin to a hill function, for the slope, or stiffness $h(d)$, changing from a to b with exponential sharpness c, at the critical displacement d_c.
Integrating this over d with $F(d=0)=0$ gives the lengthy but smooth function for $F(d)$.

$$h(d) = \frac{\partial F}{\partial d} = a + \frac{b-a}{1+e^{c(d_c-d)}} \tag{28}$$

$$F(d) = \frac{(b-a)}{c}\left(\ln(e^{c(d_c-d)}+1) - \ln(e^{cd_c}+1)\right) + b\cdot d \tag{29}$$

Now, in the time domain, it was uncovered that there too are two components, τ_1 and τ_2, to the exponential relaxation of force over time when kept at constant displacement d_{fix}, see 6.2. Careful examination of the acquired data suggested, that this could be described as a drift of the critical displacement d_c, when $d > d_c$, using the force difference from the critical point as driving agent. At $d < d_c$ there seemed to be some, albeit extremely slow, recovery. For both cases viscous creep, as described by the Kelvin model, see Equation (11), was assumed. Writing this directly in discrete form (such that it can easily be passed to the computer) gives Equation (30).
Note that in the first case the force difference $F(d) - F(d_c)$ is negative, so this case describes recovery, τ_1 is big, meaning recovery is slow. In the second case $F(d) - F(d_c)$ is positive and the smaller time constant τ_2 is added to allow for the two-component relaxation described in Section 6.2.

$$d_c(t+\Delta t) = \begin{cases} d_c(t) + \left[\frac{F(d(t)) - F(d_c(t))}{h(d(t))} \cdot \frac{e^{-\frac{\Delta t}{\tau_1}}}{\tau_1} \right] \cdot \Delta t & \text{for } d(t) \leq d_c(t), \\ d_c(t) + \left[\frac{F(d(t)) - F(d_c(t))}{h(d(t))} \cdot \left(\frac{e^{-\frac{\Delta t}{\tau_1}}}{\tau_1} + \frac{e^{-\frac{\Delta t}{\tau_2}}}{\tau_2} \right) \right] \cdot \Delta t & \text{for } d(t) > d_c(t) \end{cases} \tag{30}$$

The model I arrived at can be represented by the rheological model, shown in Figure 7.1. But keep in mind that in the macroscopic context, the springs have a stiffness not a Young's modulus and the dashpots would have units of Ns/m as to introduce two distinct relaxation times τ_1 and τ_2. The stop element used is of the exponential form, describing a continuously differentiable non-linearity with sharpness c as introduced in Section 3.

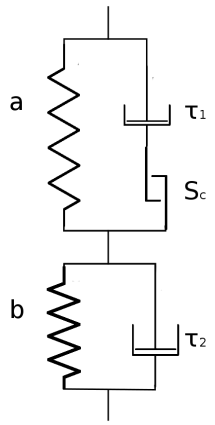

Figure 7.1: Force-displacement model used to describe the observed behavior of the wing disc under deformation.

Equation (29) was fitted to the measured force data, using the measured displacement as input and adjusting d_c for every time step using Equation (30).
Figure 7.2 shows two examples of the model fitted to data. On top the data and the fit are presented as $F(d)$, with the data in blue and the fit in red. In the lower panel the data and fit are presented as functions of time. $d(t)$ is in blue, $F(t)$ is in red and the fit is in black. Note that forces are scaled by a factor of 10 to make them easier visible. In-between the plots, the fit parameters are reproduced, where $d_0 = d_c(t = 0)$, as well as on the right the set conditions: amplitude A, frequency f and offset for harmonic excitations, and β and fixed state for linear measurements.
Figure 7.3 shows that this model is capable of fitting a variety of different cases from force relaxation at fixed displacement 7.3(a), over quasi-static cycling (b) to fast excitation in (c).

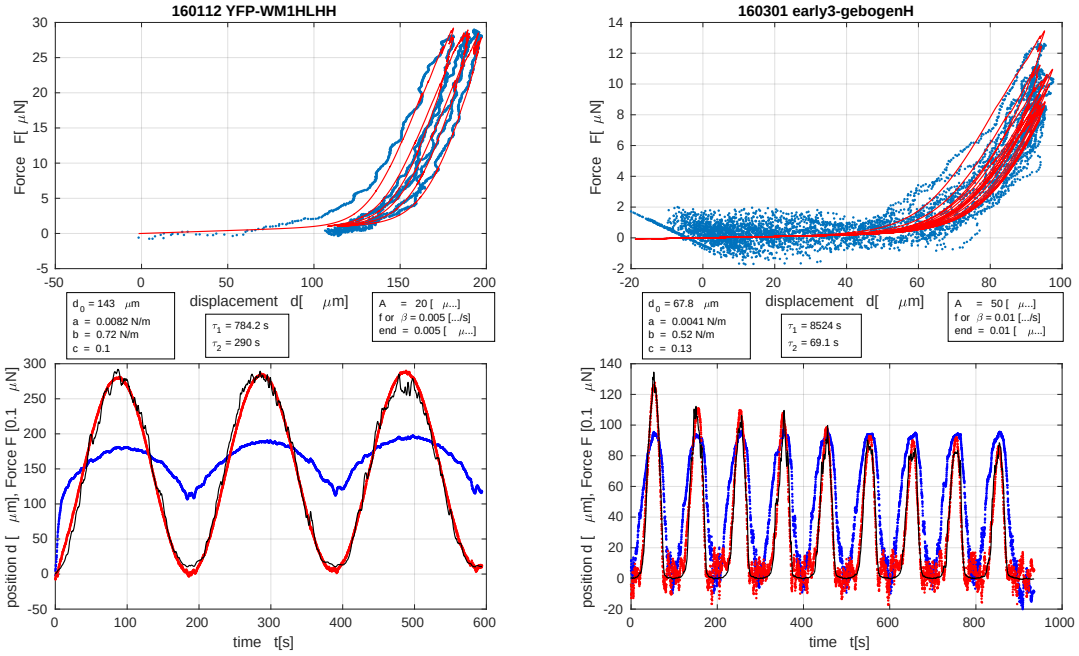

(a) (b)

Figure 7.2: Examples of fitting of the described model to data, clearly showing the following of the non-linearity and drift.

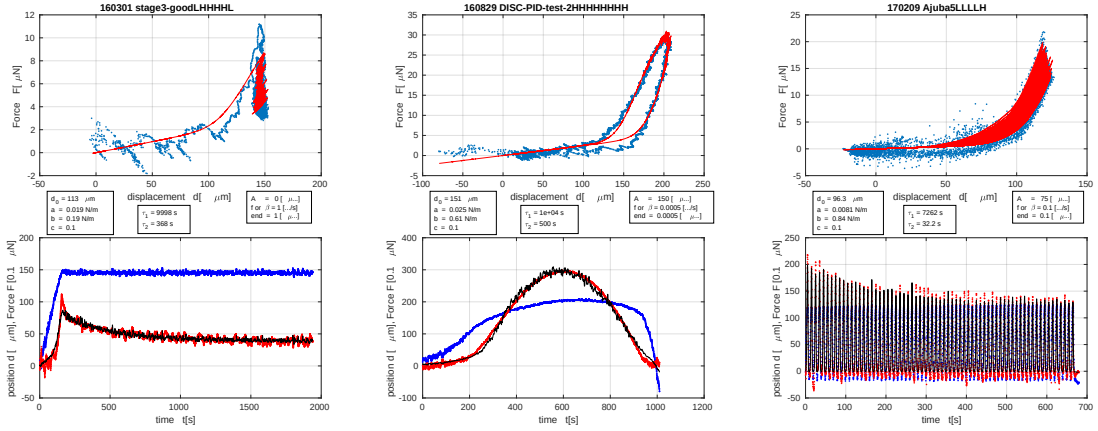

(a) (b) (c)

Figure 7.3: Fits for a variety of cases: (a) constant d_{fix}, (b) very slow cycle and (c) very fast cycling.

A total of 51 data sets were fitted, the complete set is appended to this work in appendix C. For each the residuals between the fit and the data were summed up and divided through the square of the number of points in the set, before taking the square root. The inverse of this value was used as goodness of the fit. In this way longer data sets get weighted more than short ones. The averages for the fit parameters weighted in this way are presented in table 7.1.

Wing Disc's		mech.	Parameters
d_0	=	190	µm
a	=	0.01	N/m
b	=	0.4	N/m
c	=	0.1	
τ_1	=	6000	s
τ_2	=	200	s

Table 7.1: The fitted mechanical parameters of *Drosophila's* wing disc.

d_0 found here is much larger than what was used in Section 6.2, because many measurements were included that followed previous extensions. It should realy be closer to the previously used 140 µm. a and b are both slightly smaller than what was previously found in Section 6.1. This might be because of the addition of the dashpots to the model. c is as expected. Finally the two time constants τ_1 and τ_2 are both bigger than expected; here it must be noted that they have the biggest spread of all the fit parameters. This might be an indication that there is a third timescale involved in the problem, as noted before. This can also be seen again in Figure 7.3(a), where the fit seems to miss the faster force increase in the beginning.
Also it should be noted that a considerable spread is expected when handling biologic tissue, especially with such a demanding sample preparation protocol and delicate sample placement.

8. Summary

The aim of this thesis was the characterization of the mechanical properties of the wing imaginal disc of the *Drosophila melanogaster* late third instar larvae as a model system to study the influence of mechanical forces on morphogenesis.
For this a versatile set-up was constructed with which the 3-dimensional structure of the wing disc could be imaged during highly sensitive force-displacement measurements.
It was uncovered that the wing disc has an extremely non-linear stress-strain response, a two[21]-component viscous relaxation characteristic, including some, but not complete recovery and that the over-all geometry plays a non-negligible part in the shaping of the mechanical properties of the tissue and on the internal force transduction.
In short: The wing disc is a fragile, active, non-linear visco-elasto-plastic inhomogenious composite material with a non-trivial geometry.

[21] Or three-components. The third component could possibly be an active response of the cells.

9. Discussion and Outlook

The incorporation of these findings into the context in which the work was set; the question if and how mechanical forces play a role in morphogenetic processes was not part of this thesis and will have to be left to others.
As stated in the introduction, it is believed that without measurements of the mechanical properties of a material, the discussion on the action of forces within this material or medium lacks proper footing. This work should benefit future endeavors by providing a set of parameters to characterize external force-displacement behavior of the wing disc.
A direct translation from force-displacement to stress-strain is difficult due to the strong overall reorganization of the 3-d geometry during stretching.
Rigorous analysis of the 4-d data sets in terms of Poisson's ratio could probably yield fruitful information on how to do this translation more meaningfully.
Also this work could serve to compare the outcome of similar experiments done *in silico* to. They could test different microscopic stress-strain-relations of the material and record the outcome of a global elongation experiment.
This work also provides a generic geometry of the wing disc in a top-down and y-cross-sectional view which is considered to be of great accuracy, see Figure 1.6. Especially this cross section incorporates the varying height of cells, see Figure 6.16 for detail.
With the discrete, 3-dimensional tensegrity model, described in Section 4, many of the mechanical properties uncovered in this work are believed to be reproducible and it could provide an interesting complementary counterpart to continuous material models.[22] Since it incorporates more clearly the cellular nature of the material, while intrinsically spreading forces throughout the structure, it is believed to hold interesting properties.
Further work would be needed to trace the force transduction within the tissue. For this especially drug treatments to influence the biochemical structure are of interest, now that the set-up is understood to an adequate degree. Even though these do pose additional challenges because the addition of substance to the pool of medium in which the wing disc resides is necessary. This changes the surface and therefore the surface tension which typically influences the force measurement on the same order of magnitude as the desired effect.
Also of interest are possible fluorescent labels that show dependence on external load. For this it is believed that the migration of the set-up to a newer microscope would be a necessity, since high resolution imaging on the extensometer requires fast image recording.

[22] One that could also be built of sticks and strings for experimentation and demonstration outside of the computer.

References

[1] Thompson D.W., On growth and form, UK: Cambrige University Press, 1917.

[2] Wikipedia, "D'Arcy Wentworth Thompson", *https://en.wikipedia.org/wiki/D%27Arcy_Wentworth_Thompson*, 2017.

[3] Watson J.D. and Crick F.H., "Molecular structure of nucleic acids", *Nature*, vol. 171(4356) pp. 737–738, 1953.

[4] Aegerter C., "PHY 431 - Biology for Physicists", *http://www.physik.uzh.ch/en/groups/aegerter/teaching/Biophys.html*, 2017.

[5] Galilei G., Discorsi e dimostrazioni matematiche, intorno à due nuove scienze attenenti alla mecanica & i movimenti locali, Lodewijk Elzevier, 1638.

[6] Culmann C., Die graphische statik, vol. 1, Meyer & Zeller, 1875.

[7] Wolff J., "Das Gesetz der Transformation der Knochen", *A Hirshwald*, vol. 1 pp. 1–152, 1892.

[8] Armbrecht G., Belavỳ D.L., Backström M., Beller G., Alexandre C., Rizzoli R. and Felsenberg D., "Trabecular and cortical bone density and architecture in women after 60 days of bed rest using high-resolution pQCT: WISE 2005", *Journal of bone and mineral research*, vol. 26(10) pp. 2399–2410, 2011.

[9] Vico L., Collet P., Guignandon A., Lafage-Proust M.H., Thomas T., Rehailia M. and Alexandre C., "Effects of long-term microgravity exposure on cancellous and cortical weight-bearing bones of cosmonauts", *The Lancet*, vol. 355(9215) pp. 1607–1611, 2000.

[10] Haapasalo H., Kontulainen S., Sievänen H., Kannus P., Järvinen M. and Vuori I., "Exercise-induced bone gain is due to enlargement in bone size without a change in volumetric bone density: a peripheral quantitative computed tomography study of the upper arms of male tennis players", *Bone*, vol. 27(3) pp. 351–357, 2000.

[11] Christen P., Ito K., Ellouz R., Boutroy S., Sornay-Rendu E., Chapurlat R.D. and Van Rietbergen B., "Bone remodelling in humans is load-driven but not lazy", *Nature communications*, vol. 5 p. 4855, 2014.

[12] Tatsumi S., Ishii K., Amizuka N., Li M., Kobayashi T., Kohno K., Ito M., Takeshita S. and Ikeda K., "Targeted Ablation of Osteocytes Induces Osteoporosis with Defective Mechanotransduction", *Cell Metabolism*, vol. 5 pp. 464 – 475, 2007.

[13] Jacobs C.R., Temiyasathit S. and Castillo A.B., "Osteocyte mechanobiology and pericellular mechanics", *Annual review of biomedical engineering*, vol. 12 pp. 369–400, 2010.

[14] Anderson P.W., "More is different", *Science*, vol. 177(4047) pp. 393–396, 1972.

[15] Wiktionary, "force", Wiktionary, The Free Dictionary: *https://en.wiktionary.org/w/index.php?title=force&oldid=46974402*, 2017.

[16] Wiktionary, "cause", Wiktionary, The Free Dictionary: *https://en.wiktionary.org/w/index.php?title=cause&oldid=47450576*, 2017.

[17] Lecuit T. and Le Goff L., "Orchestrating size and shape during morphogenesis", *Nature*, vol. 450(7167) p. 189, 2007.

[18] Wikipedia, "Drosophila melanogaster", *https://en.wikipedia.org/w/index.php?title=Drosophila_melanogaster&oldid=802243630*, 2017.

[19] Tyler M.S., Development of the Fruit Fly, chap. 8, Sinauer Associates, Inc. Publishers, Sunderland, MA, 2 edn., 2000.

[20] Linford N.J., Bilgir C., Ro J. and Pletcher S.D., "Measurement of Lifespan in Drosophila melanogaster", *Journal of Visualized Experiments : JoVE*, vol. 71, 2013.

[21] Diagnostics C., "Introduction to Drosophila Melanogaster", *http://www.creative-diagnostics.com/drosophila.htm*, 2017.

[22] Neufeld T.P., de la Cruz A.F.A., Johnston L.A. and Edgar B.A., "Coordination of growth and cell division in the Drosophila wing", *Cell*, vol. 93(7) pp. 1183–1193, 1998.

[23] Weigmann K., Cohen S. and Lehner C., "Cell cycle progression, growth and patterning in imaginal discs despite inhibition of cell division after inactivation of Drosophila Cdc2 kinase", *Development*, vol. 124(18) pp. 3555–3563, 1997.

[24] Day S. and Lawrence P., "Measuring dimensions: the regulation of size and shape", *Development*, vol. 127(14) pp. 2977–2987, 2000.

[25] Nienhaus U., On growth and form and patterning of drosophila wing imaginal discs, Ph.D. thesis, University of Zurich, Faculty of Science, Zürich, 2013.

[26] Aegerter-Wilmsen T., Smith A.C., Christen A.J., Aegerter C.M., Hafen E. and Basler K., "Exploring the effects of mechanical feedback on epithelial topology", *Development*, vol. 137(3) pp. 499–506, 2010.

[27] Gibson M.C. and Schubiger G., "Drosophila peripodial cells, more than meets the eye?", *Bioessays*, vol. 23(8) pp. 691–697, 2001.

[28] Sugimura K., Lenne P.F. and Graner F., "Measuring forces and stresses in situ in living tissues", *Development*, vol. 143(2) pp. 186–196, 2016.

[29] Mao Y. and Green J.B., "Systems morphodynamics: understanding the development of tissue hardware", , 2017.

[30] Milán M., Campuzano S. and García-Bellido A., "Cell cycling and patterned cell proliferation in the wing primordium of Drosophila", *Proceedings of the National Academy of Sciences*, vol. 93(2) pp. 640–645, 1996.

[31] Shraiman B.I., "Mechanical feedback as a possible regulator of tissue growth", *Proceedings of the National Academy of Sciences of the United States of America*, vol. 102(9) pp. 3318–3323, 2005.

[32] Aegerter-Wilmsen T., Aegerter C.M., Hafen E. and Basler K., "Model for the regulation of size in the wing imaginal disc of Drosophila", *Mechanisms of Development*, vol. 124(4) pp. 318 – 326, 2007.

[33] Schluck T., Nienhaus U., Aegerter-Wilmsen T. and Aegerter C.M., "Mechanical Control of Organ Size in the Development of the Drosophila Wing Disc", *PLOS ONE*, vol. 8(10) pp. 1–9, 2013.

[34] LeGoff L. and Lecuit T., "Mechanical forces and growth in animal tissues", *Cold Spring Harbor perspectives in biology*, vol. 8(3) p. a019232, 2016.

[35] Farhadifar R., Röper J.C., Aigouy B., Eaton S. and Jülicher F., "The influence of cell mechanics, cell-cell interactions, and proliferation on epithelial packing", *Current Biology*, vol. 17(24) pp. 2095–2104, 2007.

[36] Aegerter-Wilmsen T., Heimlicher M.B., Smith A.C., de Reuille P.B., Smith R.S., Aegerter C.M. and Basler K., "Integrating force-sensing and signaling pathways in a model for the regulation of wing imaginal disc size", *Development*, vol. 139(17) pp. 3221–3231, 2012.

[37] Alt S., Ganguly P. and Salbreux G., "Vertex models: from cell mechanics to tissue morphogenesis", *Phil. Trans. R. Soc. B*, vol. 372(1720) p. 20150520, 2017.

[38] Nienhaus U., Aegerter-Wilmsen T. and Aegerter C.M., "Determination of mechanical stress distribution in Drosophila wing discs using photoelasticity", *Mechanisms of Development*, vol. 126(11) pp. 942 – 949, 2009.

[39] Schluck T. and Aegerter C.M., "Photo-elastic properties of the wing imaginal disc of Drosophila", *The European Physical Journal E*, vol. 33(2) pp. 111–115, 2010.

[40] Ishihara S. and Sugimura K., "Bayesian inference of force dynamics during morphogenesis", *Journal of theoretical biology*, vol. 313 pp. 201–211, 2012.

[41] Nienhaus U., Aegerter-Wilmsen T. and Aegerter C.M., "In-Vivo Imaging of the Drosophila Wing Imaginal Disc over Time: Novel Insights on Growth and Boundary Formation", *PLOS ONE*, vol. 7(10) pp. 1–11, 2012.

[42] Ma X., Lynch H.E., Scully P.C. and Hutson M.S., "Probing embryonic tissue mechanics with laser hole drilling", *Physical biology*, vol. 6(3) p. 036004, 2009.

[43] Bonnet I., Marcq P., Bosveld F., Fetler L., Bellaïche Y. and Graner F., "Mechanical state, material properties and continuous description of an epithelial tissue", *Journal of The Royal Society Interface*, vol. 9(75) pp. 2614–2623, 2012.

[44] Burgers J., de Jong H.B., van Nieuwenburg C., Burgers W. and Jordan H., "First report on Viscosity and Plasticity", *Proceedings of the Royal Academy of Sciences, Amsterdam*, vol. 16, 1935.

[45] Ingber D.E., "The riddle of morphogenesis: a question of solution chemistry or molecular cell engineering?", *Cell*, vol. 75(7) pp. 1249–1252, 1993.

[46] Ingber D.E., "Cellular tensegrity: defining new rules of biological design that govern the cytoskeleton", *Journal of cell science*, vol. 104(3) pp. 613–627, 1993.

[47] Commons W., "File:Tensegrity 3-Prism.png — Wikimedia Commons, the free media repository", *https://commons.wikimedia.org/w/index.php?title=File:Tensegrity_3-Prism.png&oldid=156529883*, 2015.

[48] Ingber D.E., "Tensegrity I. Cell structure and hierarchical systems biology", *Journal of cell science*, vol. 116(7) pp. 1157–1173, 2003.

[49] Ingber D.E., "Tensegrity II. How structural networks influence cellular information processing networks", *Journal of cell science*, vol. 116(8) pp. 1397–1408, 2003.

[50] Levin S.M., "Continuous Tension, Discontinuous Compression - A Model for Biomechanical Support of the Body", *biotensegrityarchive.org*, , 1980.

[51] Swanson R.L., "Biotensegrity: a unifying theory of biological architecture with applications to osteopathic practice, education, and research—a review and analysis", *The Journal of the American Osteopathic Association*, vol. 113(1) pp. 34–52, 2013.

[52] Tibert G., Deployable tensegrity structures for space applications, Ph.D. thesis, KTH, 2002.

[53] Ragkousi K. and Gibson M.C., "Cell division and the maintenance of epithelial order", *J Cell Biol*, vol. 207(2) pp. 181–188, 2014.

[54] Stamenović D., Fredberg J.J., Wang N., Butler J.P. and Ingber D.E., "A microstructural approach to cytoskeletal mechanics based on tensegrity", *Journal of Theoretical Biology*, vol. 181(2) pp. 125–136, 1996.

[55] Restrepo S., Zartman J.J. and Basler K., Cultivation and Live Imaging of Drosophila Imaginal Discs, pp. 203–213, Springer New York, New York, NY, 2016.

[56] micro-epsilon, CH-9300 Wittenbach, Laser Triangulation Displacement Sensors, 2014.

[57] SmarAct GmbH, D-26135 Oldenburg, Product Catalogue, 2013.

[58] Leica, CH-4132 Muttenz, Leica HCS Objektive, Version 7.5, 2017.

[59] h+s Präzisionsfolien GmbH, D-92712 Pirk, Gehärteter Federbandstahl W.-Nr. 1.1274, 2014.

[60] Femto Tools, CH-8107 Buchs/ZH, FT-S540 Force Sensing Probe, 2010.

[61] Femto Tools, CH-8107 Buchs/ZH, FT-SDA01 User Guide, 2010.

[62] Elliott C., Vijayakumar V., Zink W. and Hansen R., "National instruments LabVIEW: a programming environment for laboratory automation and measurement", *JALA: Journal of the Association for Laboratory Automation*, vol. 12(1) pp. 17–24, 2007.

[63] Commons W., "File:PID en.svg — Wikimedia Commons, the free media repository", *https://commons.wikimedia.org/w/index.php?title=File:PID_en.svg&oldid=199645256*, 2016.

[64] Devlin E., "Drosophila HSP's", *http://people.hsc.edu/faculty-staff/edevlin/edsweb01/courses/Development/labmanual/new_page_7.htm*, 2017.

[65] Huang J., Zhou W., Dong W., Watson A.M. and Hong Y., "Directed, efficient, and versatile modifications of the Drosophila genome by genomic engineering", *Proceedings of the National Academy of Sciences*, vol. 106(20) pp. 8284–8289, 2009.

[66] Guha A., Lin L. and Kornberg T.B., "Regulation of Drosophila matrix metalloprotease Mmp2 is essential for wing imaginal disc:trachea association and air sac tubulogenesis", *Developmental Biology*, vol. 335(2) pp. 317 – 326, 2009.

[67] Lye C.M., Naylor H.W. and Sanson B., "Subcellular localisations of the CPTI collection of YFP-tagged proteins in Drosophila embryos", *Development*, vol. 141(20) pp. 4006–4017, 2014.

[68] Mdf, "Spherical-aberration-slice", Wikimedia: *https://commons.wikimedia.org/wiki/File:Spherical-aberration-slice.jpg*, 2005.

[69] Jacobkhed, "Jablonski Diagram of Fluorescence Only", Wikimedia: *https://commons.wikimedia.org/wiki/File:Jablonski_Diagram_of_Fluorescence_Only.png*, 2012.

[70] Scientific T., "Fluorescence SpectraViewer", *https://www.thermofisher.com/ch/en/home/life-science/cell-analysis/labeling-chemistry/fluorescence-spectraviewer.html*, 2017.

[71] Schindelin J., Arganda-Carreras I., Frise E., Kaynig V., Longair M., Pietzsch T., Preibisch S., Rueden C., Saalfeld S., Schmid B. et al., "Fiji - an Open Source platform for biological image analysis", *Nature methods*, vol. v(7) pp. 676–682, 2015.

[72] Schluck T., Mechanical perturbation and stimulation of drosophila wing imaginal discs, Ph.D. thesis, University of Zurich, Faculty of Science, Zürich, 2013.

[73] Edgeworth R., Dalton B. and Parnell u.T., "The pitch drop experiment", *European Journal of Physics*, vol. 5(4) p. 198, 1984.

[74] de Reuille P.B., Routier-Kierzkowska A.L., Kierzkowski D., Bassel G.W., Schüpbach T., Tauriello G., Bajpai N., Strauss S., Weber A., Kiss A. et al., "MorphoGraphX: a platform for quantifying morphogenesis in 4D", *Elife*, vol. 4 p. e05864, 2015.

[75] Mazia D., Schatten G. and Sale W., "Adhesion of cells to surfaces coated with polylysine. Applications to electron microscopy.", *The Journal of Cell Biology*, vol. 66(1) pp. 198–200, 1975.

APPENDIX

FemtoTool Reference Sheet

FEMTO TOOLS http://www.femtotools.com

Calibration Reference Sheet I

Device ID nr.:1613
Type: FT-S540
Calib. Ref.: S540_327
Package type: protective package v3

Sensor gain: 93.4uN/V

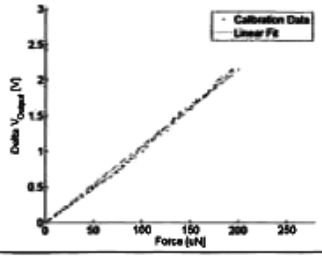

Calibration responsible:

S. Muntwyler

Figure .1: The calibration reference sheet for FT-S540, nr. 1613 used in set-up calibration.

A. Extended Protocol

I: Starting the PCs, the microscope, positioner, ILD-sensor and the software for imaging and force measurements before doing anything else ensured they will in fact be ready when needed. Also the laser needed some time to stabilize.

II: PLL stands for poly-l-lysin. Lysin is positively charged at physiological pH, providing electrostatic attraction for the anionic outside of tissues or single cells. The coating of surfaces with polylisine for tight adhesion in these cases is well established. A procedure almost identical to the original one, published in 1975 [75], was used here. A drop of 0.1% solution of polylysine in water was placed on the clean glass slide, where the wing disc shall be attached. For the glass slide at the end of the cantilever this meant to carefully place the drop at the underside of the glass slide, using a fine syringe. Then the PLL drops were left to dry out. The next step usually consists in rinsing the glass with water. This step was omitted as it was found that it was not essential for good adhesion and would have complicated the procedure.

III: To minimize chemical stress to the wing disc, its surrounding medium should change as little as possible when dissected out of the larval body. For this the optimized wing disc culture medium (WM1) was developed at the university [55]. It takes commercial Schneider's insect Medium as a base and adds insulin and Fly Extract which is harvested from adult flies. Dissection was carried out in a drop of 100 µl WM1 under a binocular. To increase visibility of the almost transparent wing disc, the illuminating light source was moved to a 90°angle, resulting in a dark-field-microscopy-kind of set up, observing mostly scattered light.

Since other than the wing disc, no other parts of the larvae needed to be treated with care, dissection was carried out in the following manner:

- The larva was held by two tweezers, as illustrated in Figure 5.18(b), by pulling, the skin of the larva opened up, see Figure 1.4.
- The imaginal discs, connected to the tracheae and to muscle fibers floated out. Some of the muscle fibers connected imaginal discs to one another.
- Next the big wing discs, connected to the small haltere discs, were located.
- To separate these two discs from the rest of the larva, the haltere disc was gripped with one pair of tweezers and the other one was used to pull away the trachea and connecting fibers from the wing disc. This way the wing disc was never touched directly by the tweezers.

IV: The same grip on the haltere disc was used to transfer the wing disc to a plastic basin filled with phosphate buffered saline (PBS). There the cover slip with the mini pool as well as the disc inverter with the PLL-treated glass slide were ready, as seen in Figure 5.19(a).

This and the following steps were performed in PBS instead of WM1, because of the big amount of solution used to fill the plastic basin. WM1 could not be provided in this quantity. PBS is a "first-order approximation" to a good culture medium, providing good ion content at the right pH. Nevertheless care was taken to preside swiftly until exchange of PBS for WM1 (step VIII:). On average the disc spent roughly 5 minutes in PBS.

V: To attach the first side of the wing disc to the glass slide, the wing disc, held by the haltere disc with the tweezers, was gently directed towards the glass slide. To get correct orientation

and positioning of the wing disc with respect to the glass slide required some practice, since it could rotate quite freely around the muscle fiber connecting it to the haltere disc. Figure 5.19(b) shows a cut trough a well-placed disc on the glass slide.

VI: When turning the disc inverter and placing it inside the pool on the cover slip, care had to be taken for the wing disc not to fold under the glass slide. This was done by hand and is the main purpose for the "disc inverter": to be big enough to handle and turn. Figure 5.19(c) shows the attached disc inverted, with the peripodial membrane facing down towards the cover slip but without touching it.

VII: Next the cover slip with the disc inverter was lifted out of the PBS basin and put into the aluminium frame, see Figure 5.6. Here a problem was faced using the original disc inverter shown in Figure 5.5. In essence the gap between the handles and the pool acted as a capillary, sucking medium out of the pool and quickly draining the pool. After some attempts to prevent this from happening, it was realized that the stiction of the disc inverter on the cover slide was much bigger than any force on the wing disc would ever be, so the handles were not needed and the problem was solved by simply cutting them off.

VIII: The pool roughly held 400 µl of medium. To exchange the PBS for WM1, 300 µl of PBS were pipetted out of the pool, just leaving the wing disc covered, then 100 µl of WM1 were added and mixed with the PBS and 100 µl of the mixture were pipetted out again. This was repeated three times before filling the pool up entirely with WM1.

IX: Having succeeded in the delicate work of dissecting and attaching the wing disc and exchanging the medium, the transfer to the microscope in the aluminium frame was straightforward. After placing a drop of H_2O on the objective, the aluminium frame could be sunken into the corresponding opening on the sample holder.

X: As the sketch in Figure 5.1 indicates, the cantilever was mounted to a 2-axis dovetail translation stage for y- and z-axis control. The x-axis movement was controlled directly by the positioner. These were used to move the cantilever in air until its glass slide was above the wing disc.

Here the position of the ILD displacement sensor needed to be adjusted, such that its laser light hit the upper flag extension at the end of the cantilever.

While observing trough the microscope, the cantilever was then lowered into the medium and positioned just above the wing disc. The anionic PLL on the glass slide will gradually get covered in fat and other biomolecules from the medium so the following steps were performed as swiftly as possible.

XI: Measurement started in LabVIEW.

XII: The second side of the wing disc was attached to the glass slide from the cantilever, simply by lowering said glass slide until the wing disc was gently squeezed between it and the cover slip and left in this position for a few seconds to ensure good attachment.

XIII: The height was then reset, to have the two glass slides on the same height. This was a bit difficult to see by eye in the wide field transmission image. In order to get the best results possible this could be checked in the confocal image.

XIV: To minimize noise on the measurement and evaporation of the medium (see Section 5.1.1, paragraphs cantilever and noise reduction) wet tissues were placed next to the experiment and everything was covered by a box.

XV: Finally all desired parameters for the experiment in the Leica imaging software as well as the LabVIEW force measurement software were set and the experiment started.

B. Full Geometry Timeline

Continuously recorded 4-d data set. Upper left: a z-projection, upper right: x-cross-section, lower left: y-cross-section and lower right: recorded force-displacement curve.

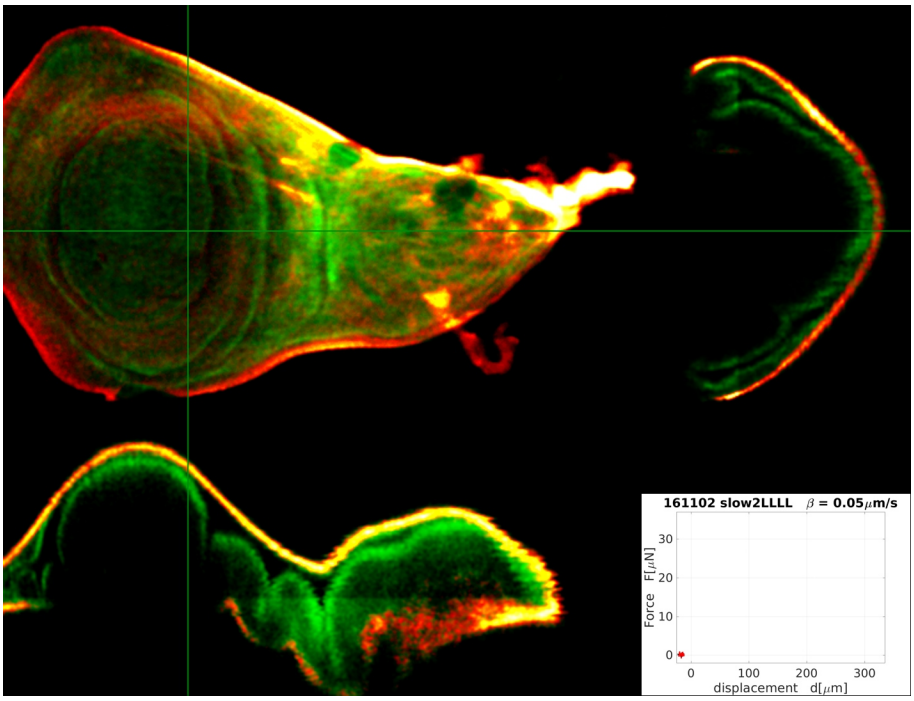

(a)

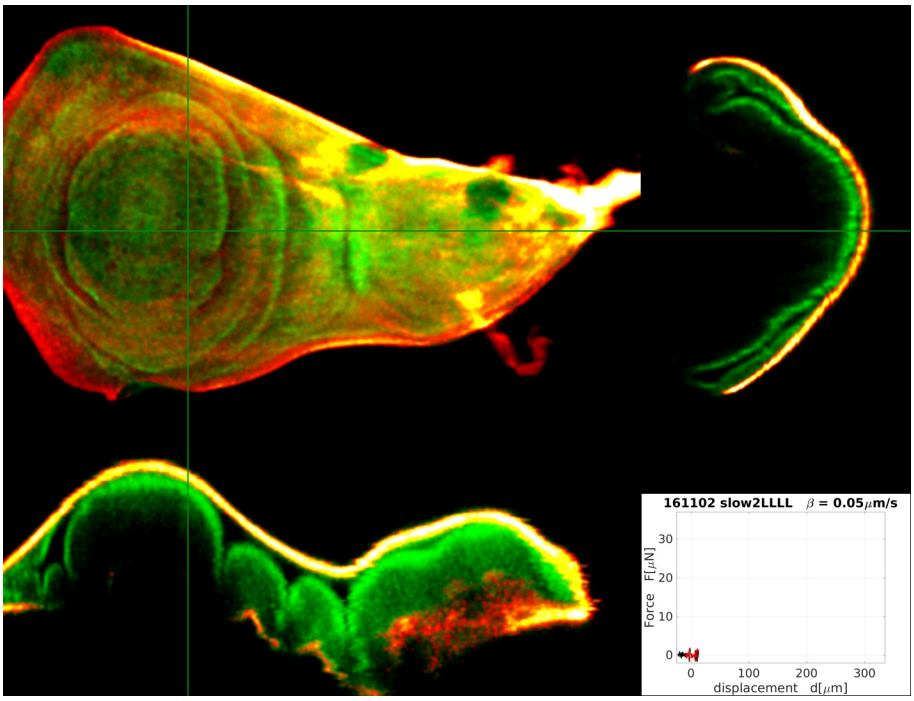
161102 slow2LLLL β = 0.05μm/s
Force F[μN]
30
20
10
0
0
100
200
300
displacement d[μm]

(b)

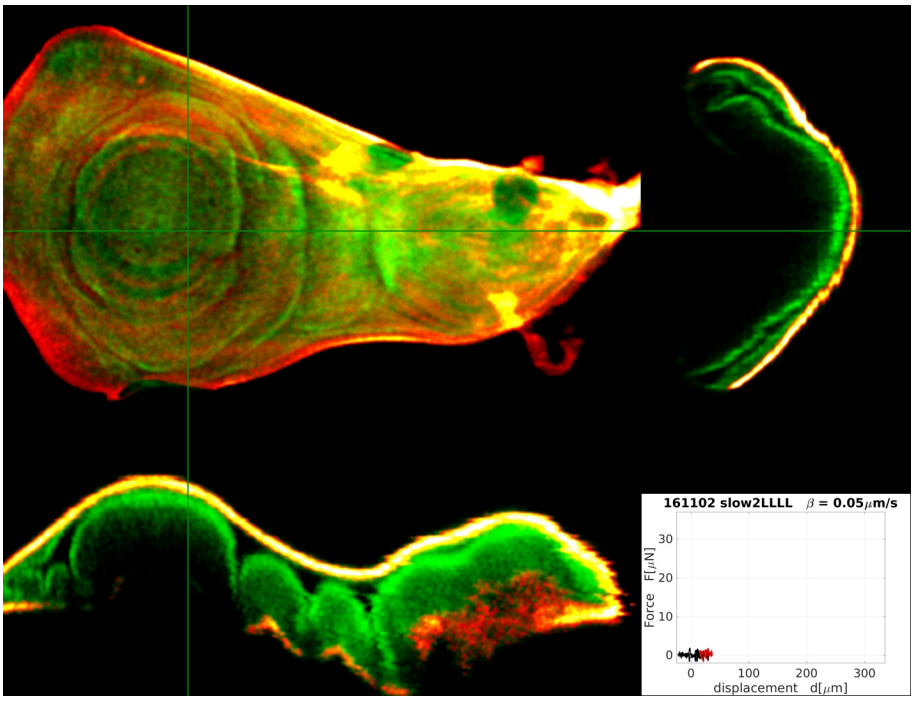
161102 slow2LLLL β = 0.05μm/s
Force F[μN]
30
20
10
0
0
100
200
300
displacement d[μm]

(c)

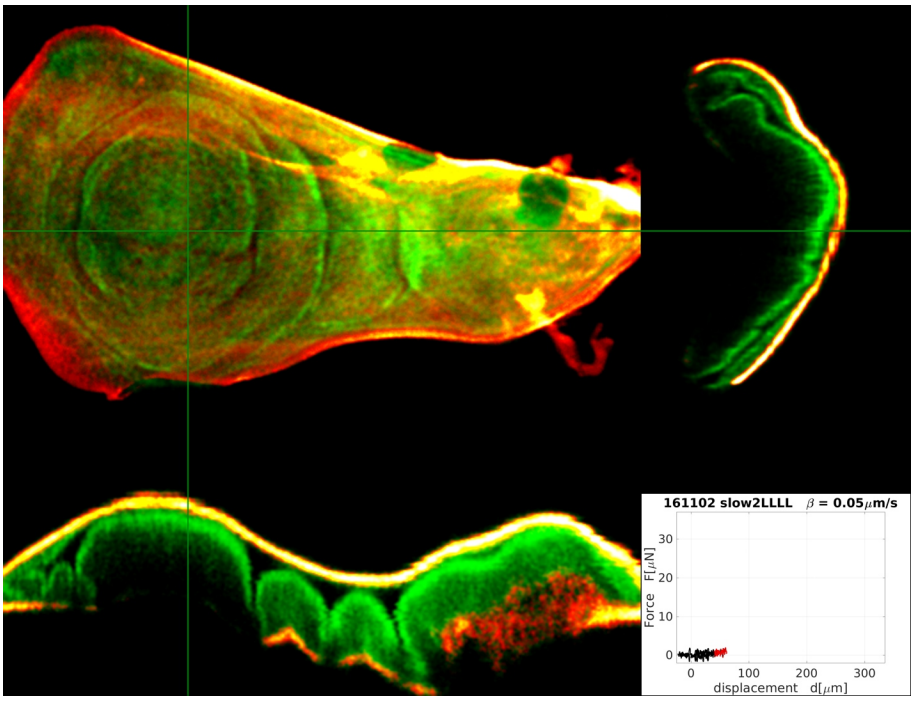
161102 slow2LLLL β = 0.05μm/s
Force F[μN]
30
20
10
0
0
100
200
300
displacement d[μm]

(d)

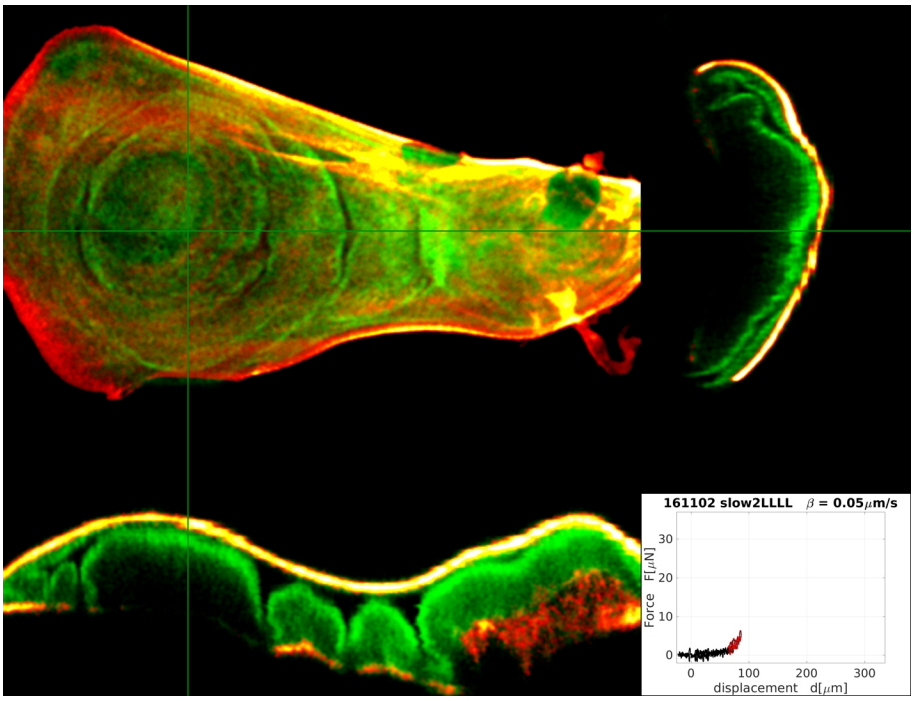
161102 slow2LLLL β = 0.05μm/s
Force F[μN]
30
20
10
0
0
100
200
300
displacement d[μm]

(e)

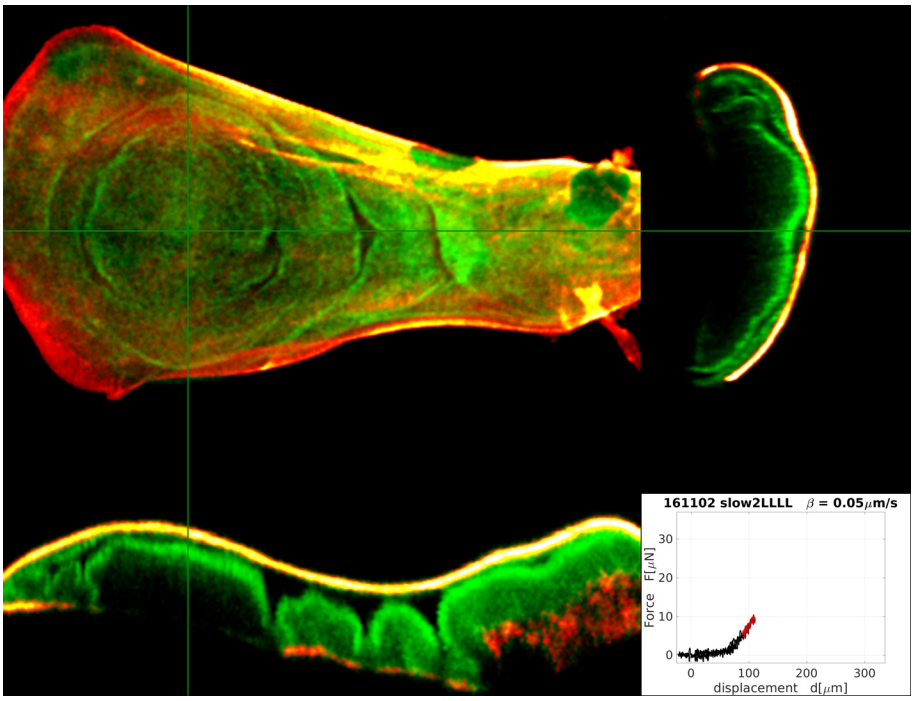
161102 slow2LLLL β = 0.05μm/s
Force F[μN]
30
20
10
0
0
100
200
300
displacement d[μm]

(f)

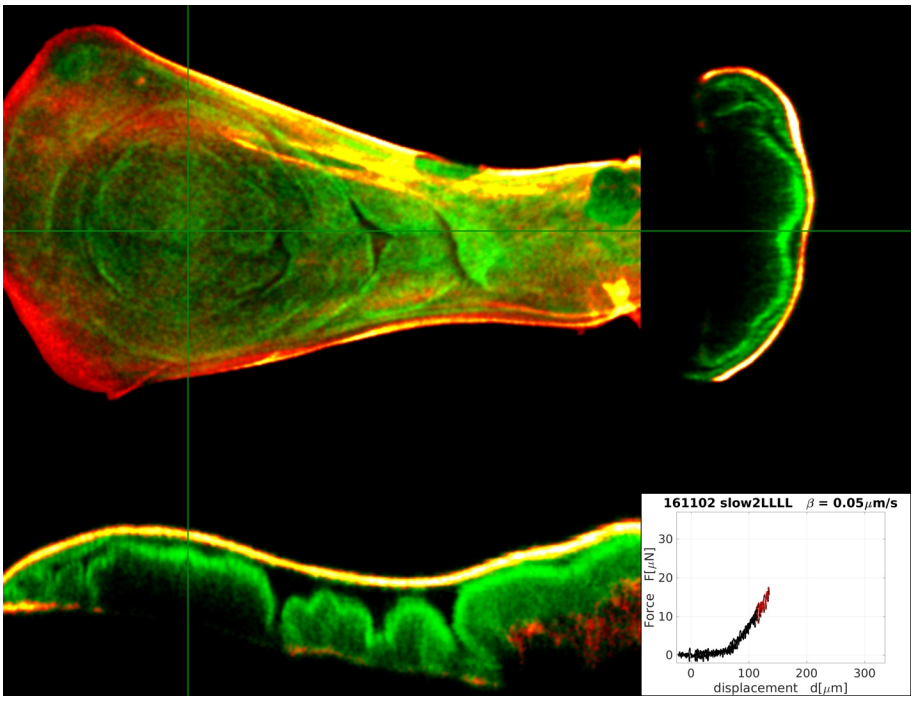
161102 slow2LLLL β = 0.05μm/s
Force F[μN]
30
20
10
0
0
100
200
300
displacement d[μm]

(g)

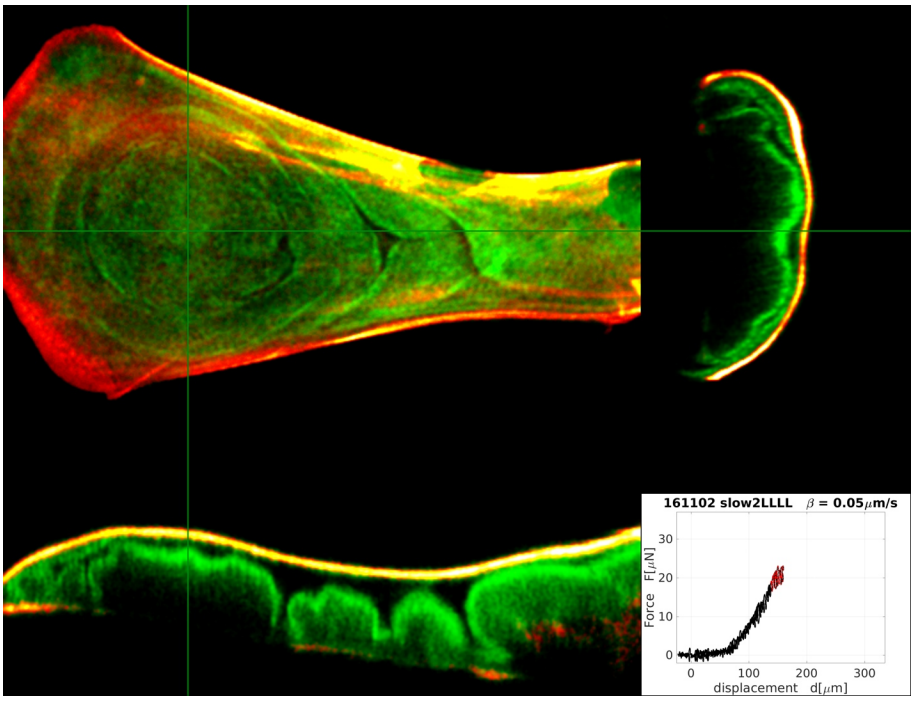
161102 slow2LLLL β = 0.05μm/s
Force F[μN]
30
20
10
0
0
100
200
300
displacement d[μm]

(h)

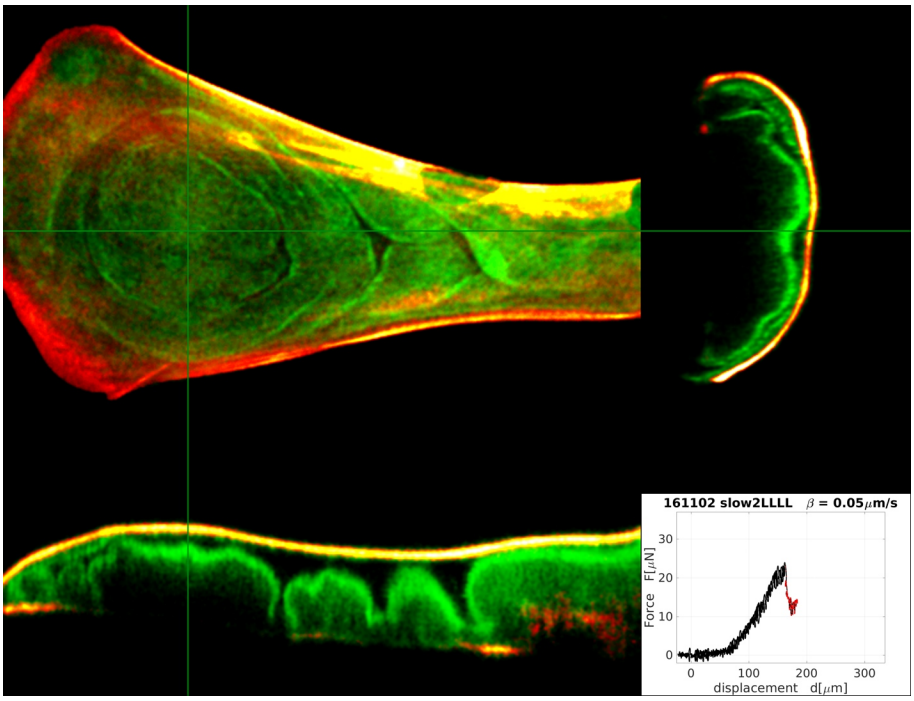
161102 slow2LLLL β = 0.05μm/s
Force F[μN]
30
20
10
0
0
100
200
300
displacement d[μm]

(i)

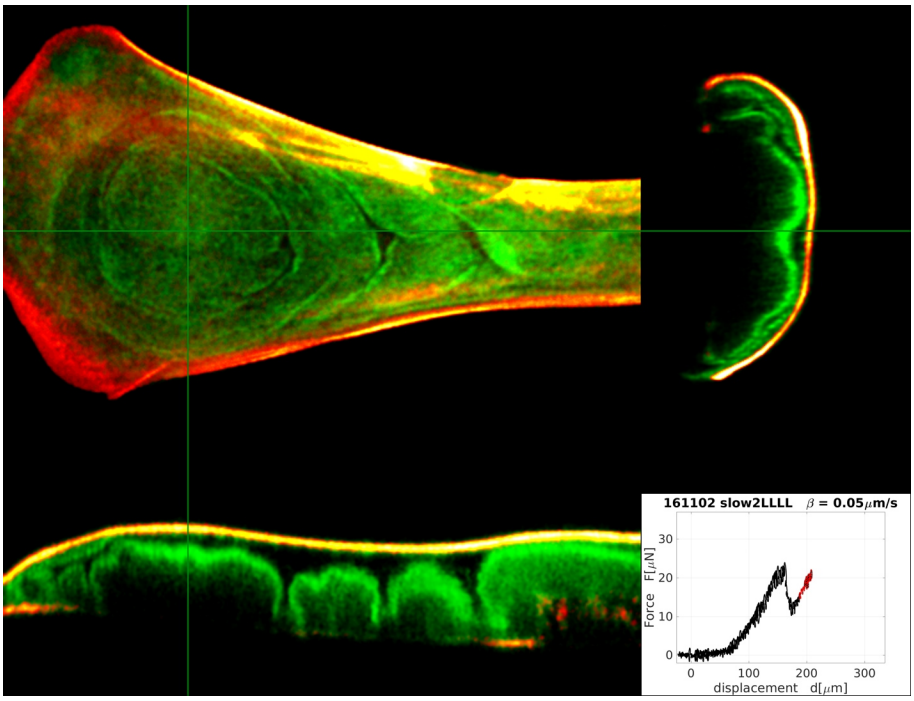
161102 slow2LLLL β = 0.05μm/s
Force F[μN]
30
20
10
0
0
100
200
300
displacement d[μm]

(j)

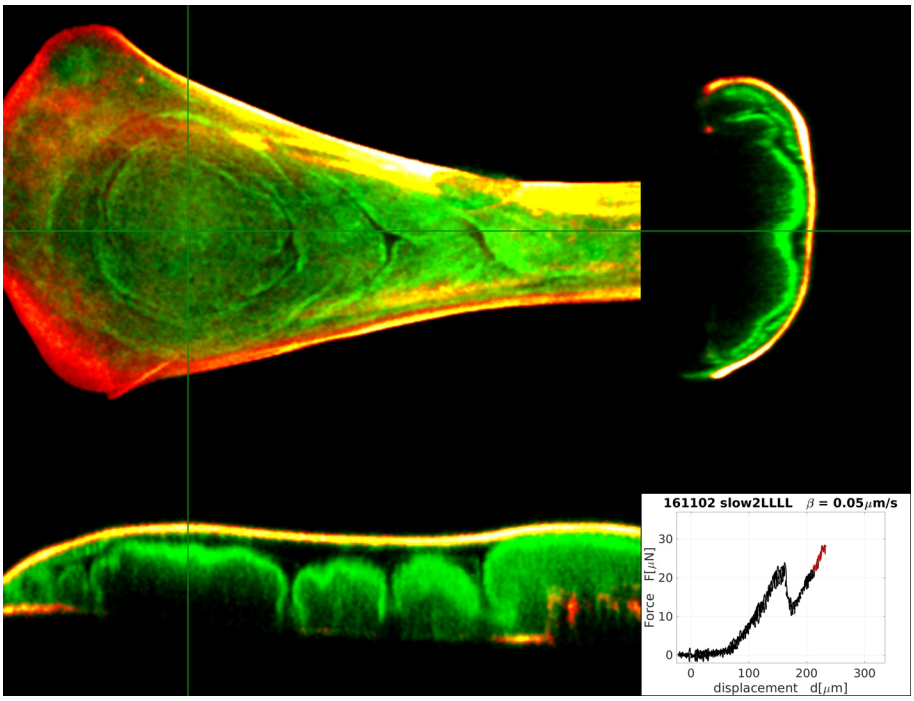
161102 slow2LLLL β = 0.05μm/s
Force F[μN]
30
20
10
0
0
100
200
300
displacement d[μm]

(k)

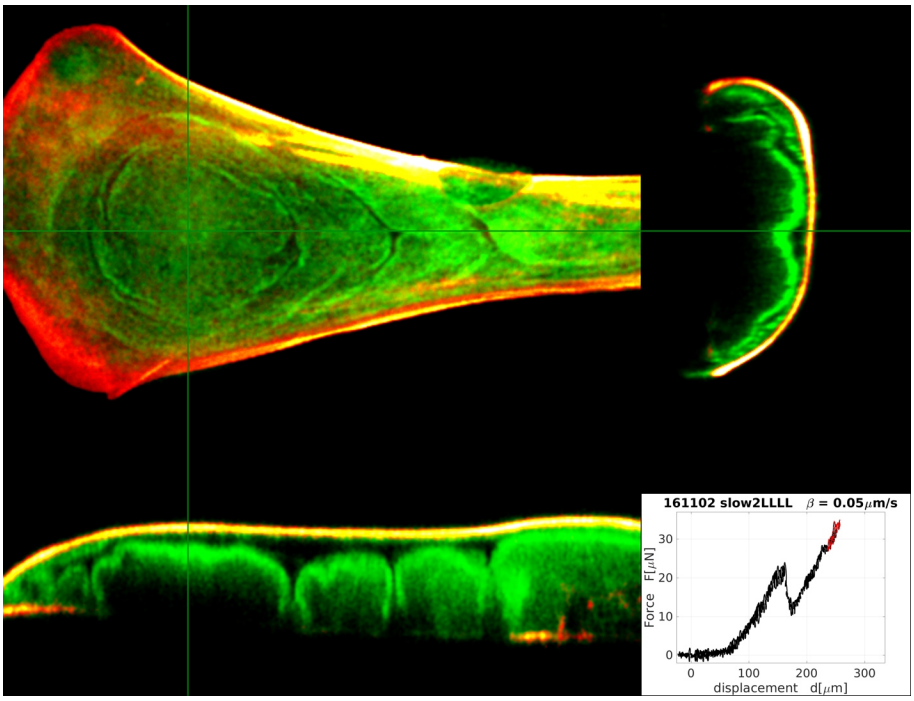
161102 slow2LLLL β = 0.05μm/s
Force F[μN]
30
20
10
0
0
100
200
300
displacement d[μm]

(l)

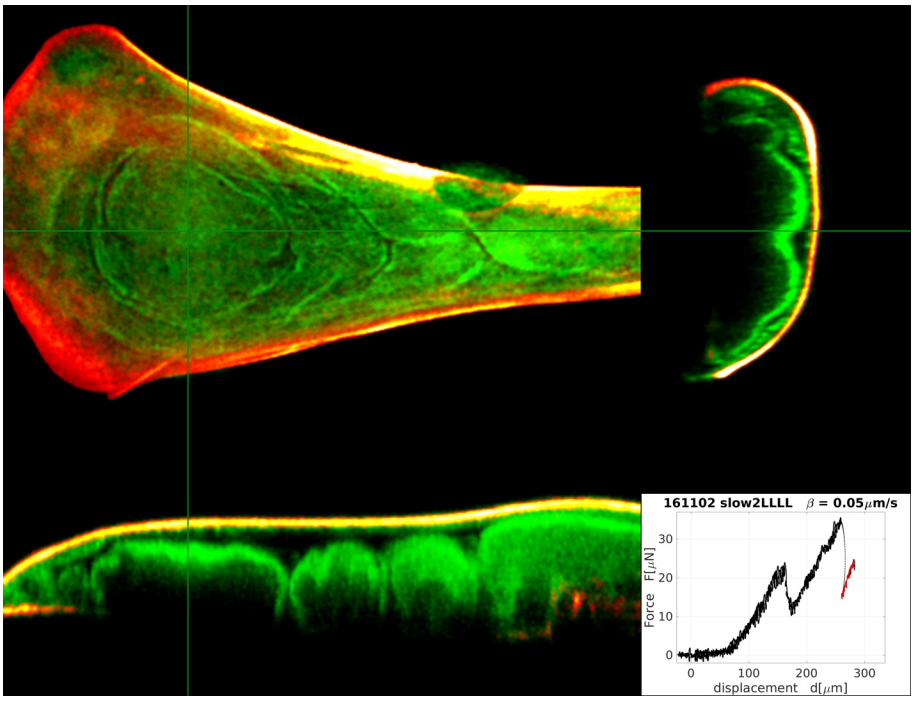
161102 slow2LLLL β = 0.05μm/s
Force F[μN]
30
20
10
0
0
100
200
300
displacement d[μm]

(m)

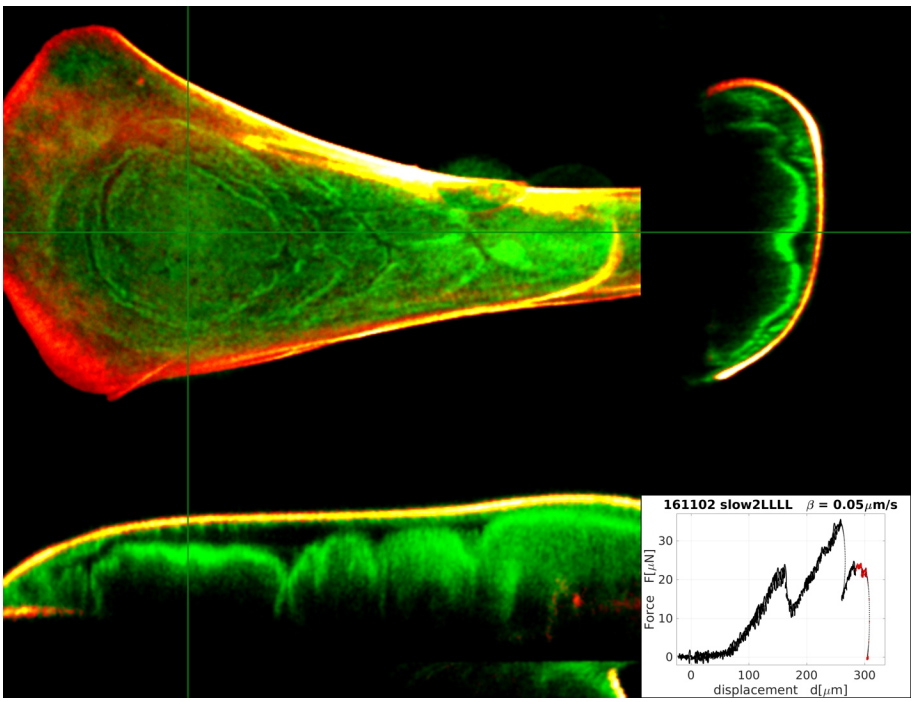

(n)

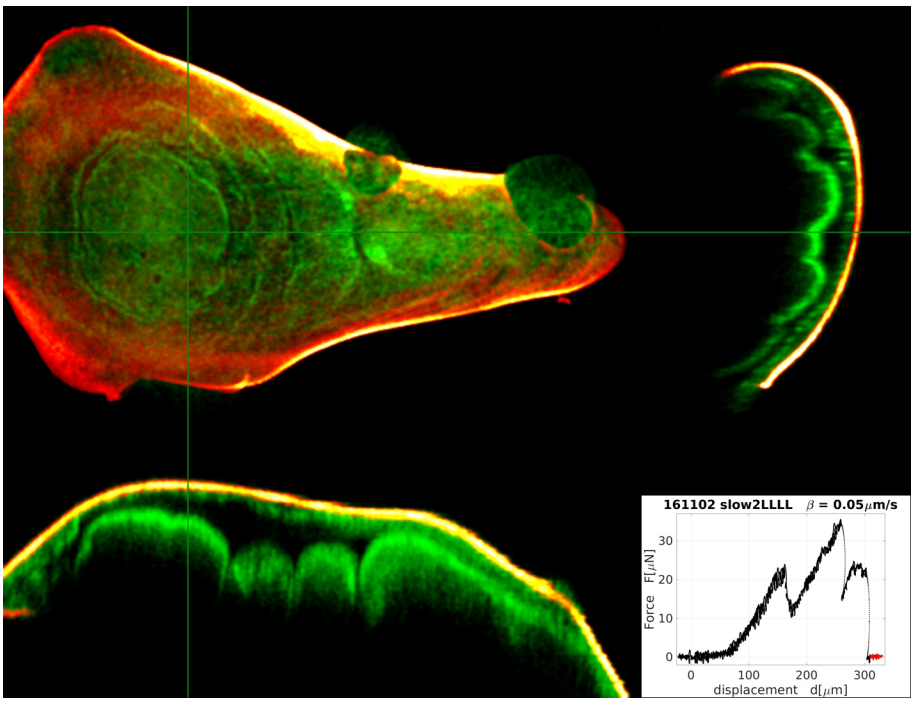

(o)

Figure B.1: Continuously recorded 4-d data set. Upper left: a z-projection, upper right: x-cross-section, lower left: y-cross-section and lower right: recorded force-displacement curve.

C. 1-D Model Fits

Reproduction of the 51 fits of the constructed rheological model to describe the emergent force-displacement characteristics of the wing imaginal disc of *Drosophila melanogaster*.

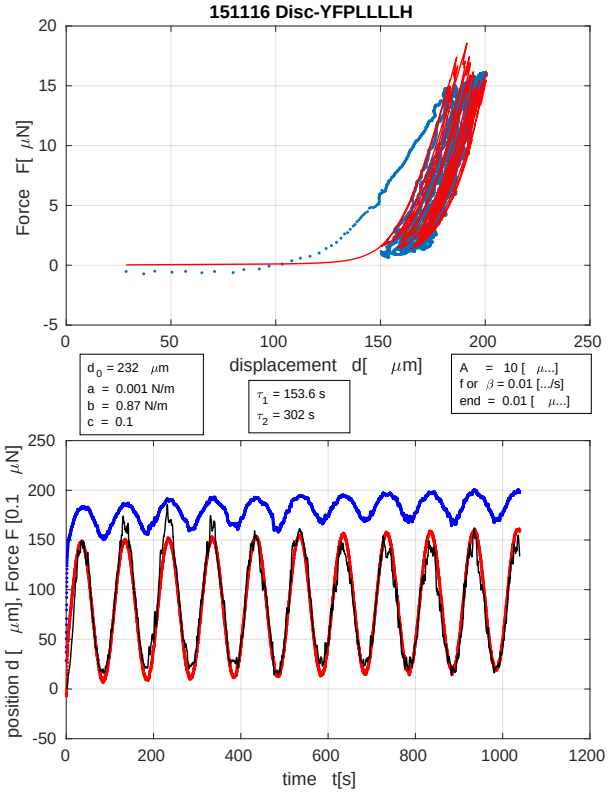

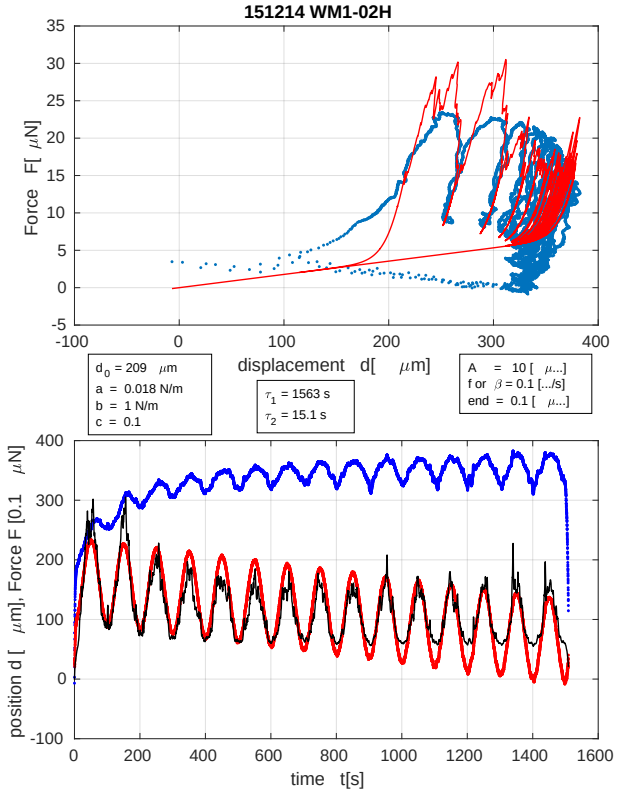

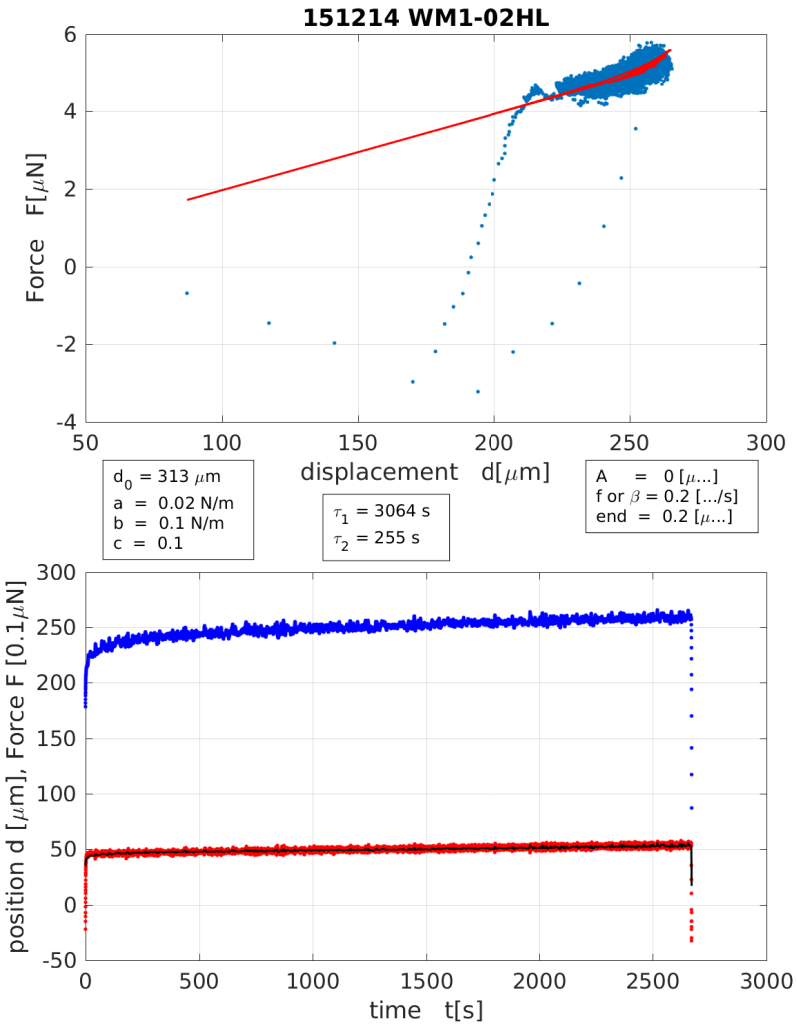
151214 WM1-02HL
Force F[μN]
displacement d[μm]
d0 = 313 μm
a = 0.02 N/m
b = 0.1 N/m
c = 0.1
τ1 = 3064 s
τ2 = 255 s
A = 0 [μ...]
f or β = 0.2 [.../s]
end = 0.2 [μ...]
position d [μm], Force F [0.1μN]
time t[s]

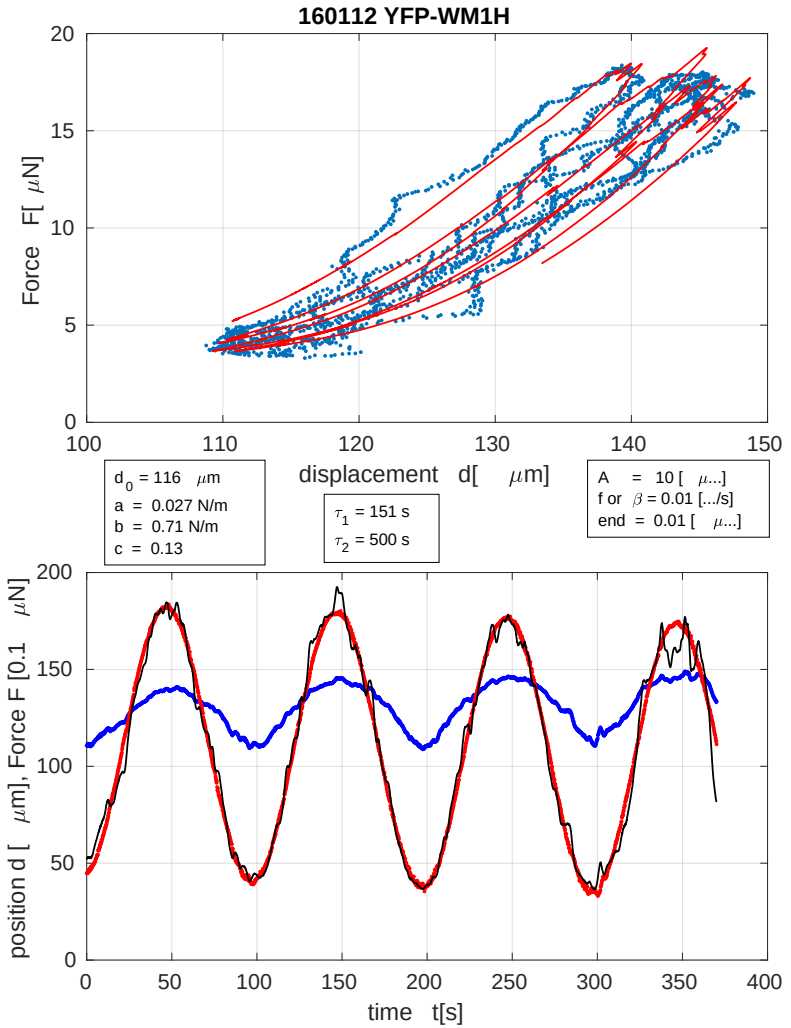
160112 YFP-WM1H
Force F[μN]
displacement d[μm]
d0 = 116 μm
a = 0.027 N/m
b = 0.71 N/m
c = 0.13
τ1 = 151 s
τ2 = 500 s
A = 10 [μ...]
f or β = 0.01 [.../s]
end = 0.01 [μ...]
position d [μm], Force F [0.1 μN]
time t[s]

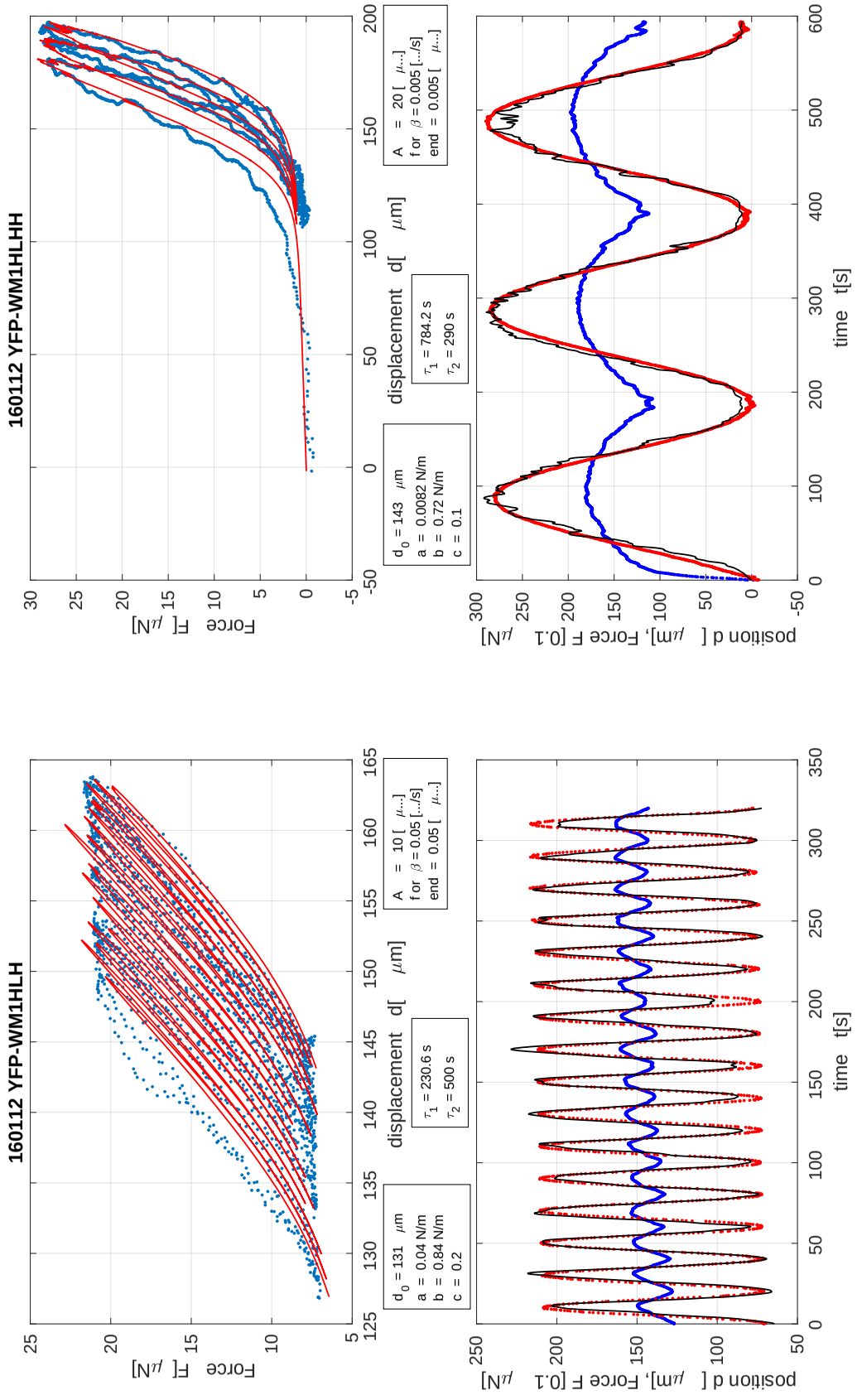
160112 YFP-WM1HLHH
Force F[μN]
displacement d[μm]
d0 = 143 μm
a = 0.0082 N/m
b = 0.72 N/m
c = 0.1
τ1 = 784.2 s
τ2 = 290 s
A = 20 [μ...]
for β = 0.005 [.../s]
end = 0.005 [μ...]
position d [μm], Force F [0.1 μN]
time t[s]
160112 YFP-WM1HLH
Force F[μN]
displacement d[μm]
d0 = 131 μm
a = 0.04 N/m
b = 0.84 N/m
c = 0.2
τ1 = 230.6 s
τ2 = 500 s
A = 10 [μ...]
for β = 0.05 [.../s]
end = 0.05 [μ...]
position d [μm], Force F [0.1 μN]
time t[s]

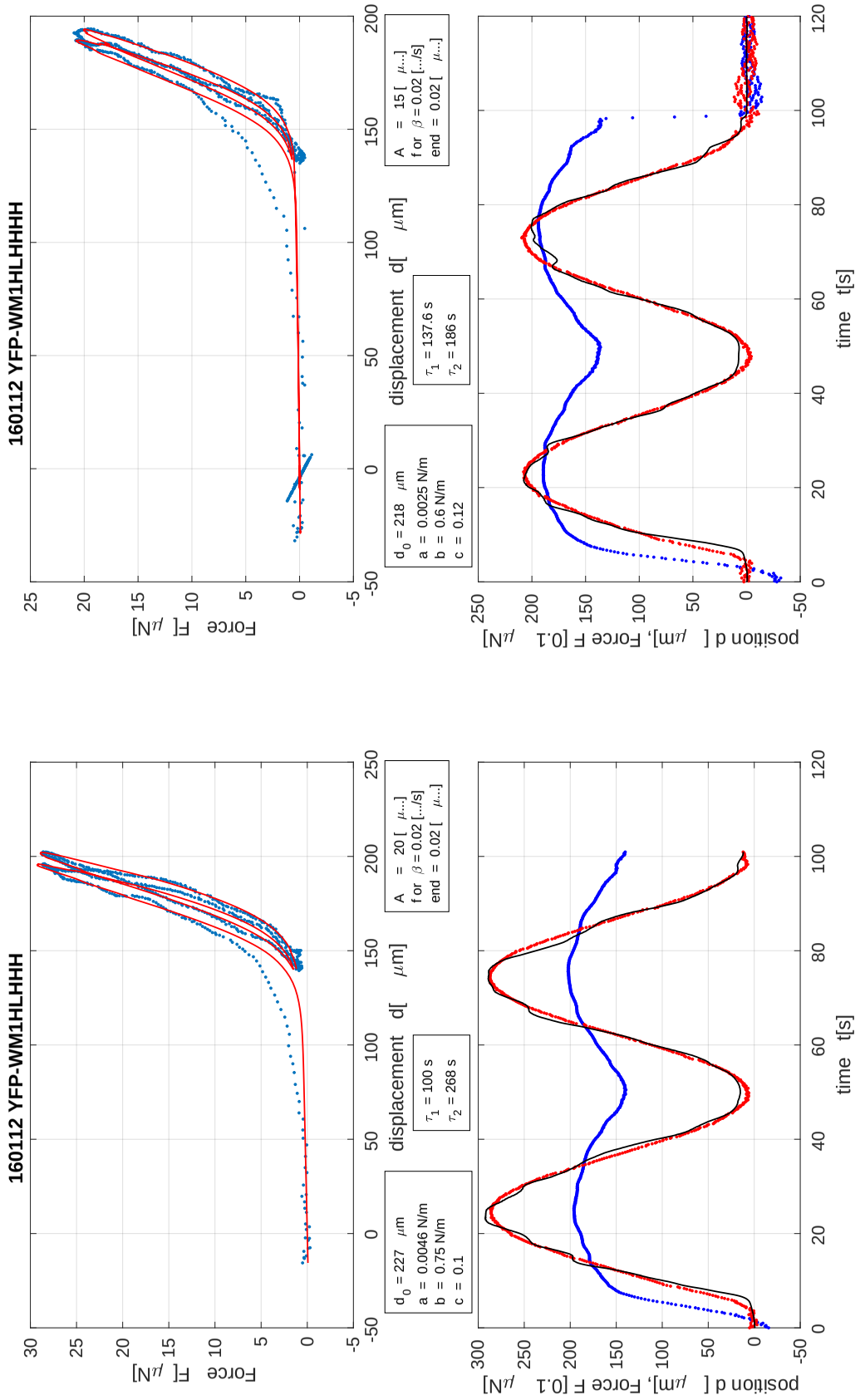
160112 YFP-WM1HLHHH
Force F[μN]
displacement d[μm]
d0 = 218 μm
a = 0.0025 N/m
b = 0.6 N/m
c = 0.12
τ1 = 137.6 s
τ2 = 186 s
A = 15 [μ...]
for β = 0.02 [.../s]
end = 0.02 [μ...]
position d [μm], Force F [0.1 μN]
time t[s]
160112 YFP-WM1HLHHH
Force F[μN]
displacement d[μm]
d0 = 227 μm
a = 0.0046 N/m
b = 0.75 N/m
c = 0.1
τ1 = 100 s
τ2 = 268 s
A = 20 [μ...]
for β = 0.02 [.../s]
end = 0.02 [μ...]
position d [μm], Force F [0.1 μN]
time t[s]

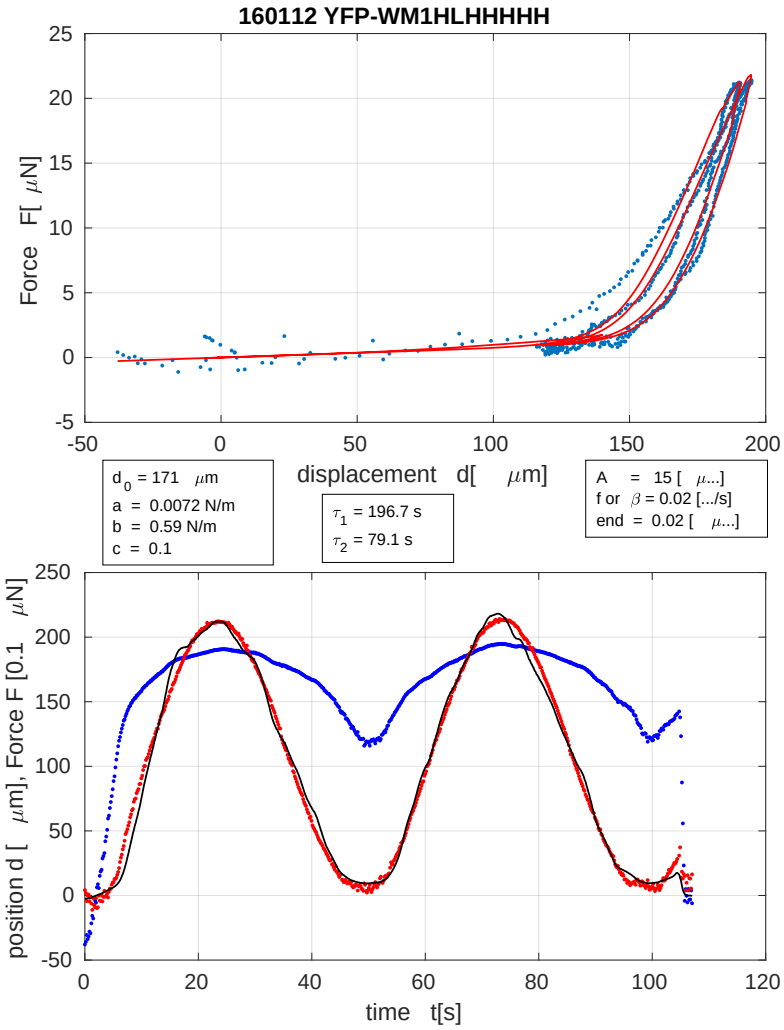
160112 YFP-WM1HLHHHHH
Force F[μN]
displacement d[μm]
d0 = 171 μm
a = 0.0072 N/m
b = 0.59 N/m
c = 0.1
τ1 = 196.7 s
τ2 = 79.1 s
A = 15 [μ...]
f or β = 0.02 [.../s]
end = 0.02 [μ...]
position d [μm], Force F [0.1 μN]
time t[s]

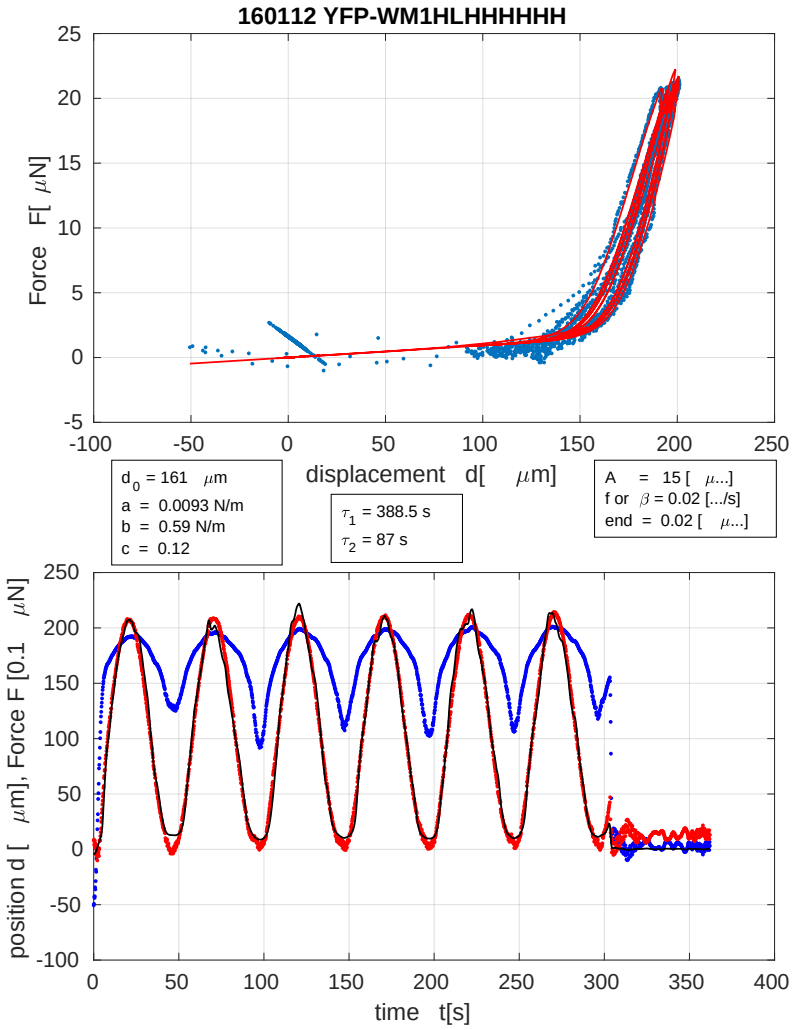
160112 YFP-WM1HLHHHHHH
Force F[μN]
displacement d[μm]
d0 = 161 μm
a = 0.0093 N/m
b = 0.59 N/m
c = 0.12
τ1 = 388.5 s
τ2 = 87 s
A = 15 [μ...]
f or β = 0.02 [.../s]
end = 0.02 [μ...]
position d [μm], Force F [0.1 μN]
time t[s]

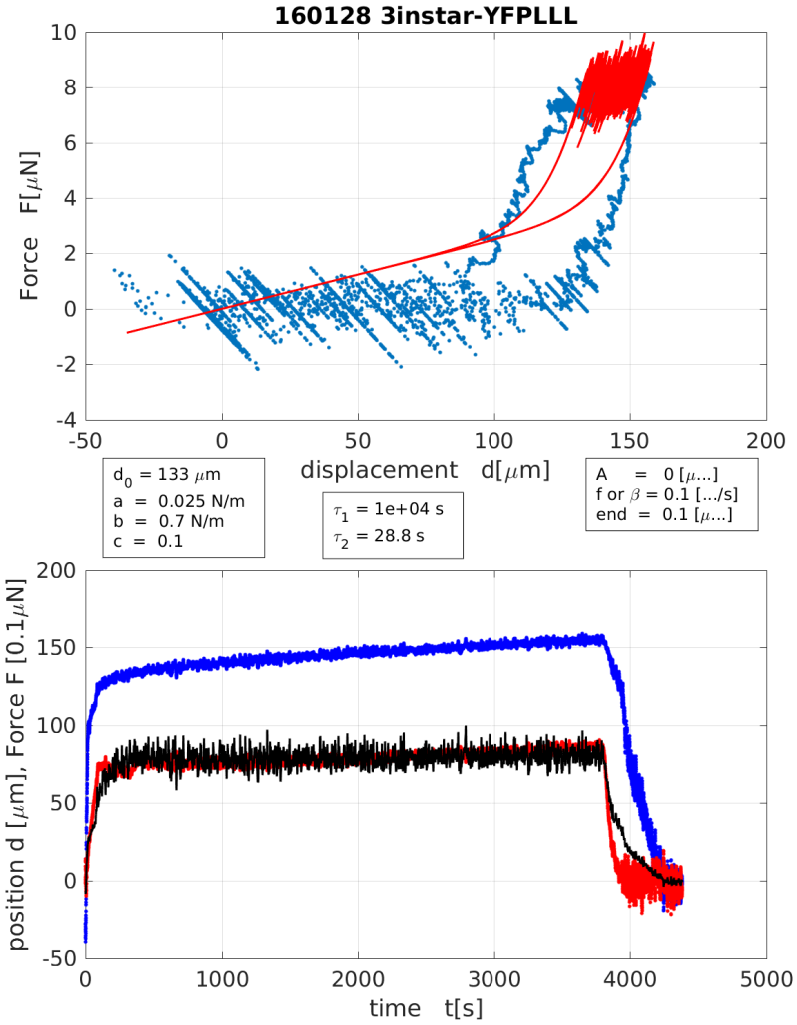
160128 3instar-YFPLLL
Force F[μN]
displacement d[μm]
d$_0$ = 133 μm
a = 0.025 N/m
b = 0.7 N/m
c = 0.1
τ_1 = 1e+04 s
τ_2 = 28.8 s
A = 0 [μ...]
f or β = 0.1 [.../s]
end = 0.1 [μ...]
position d [μm], Force F [0.1μN]
time t[s]

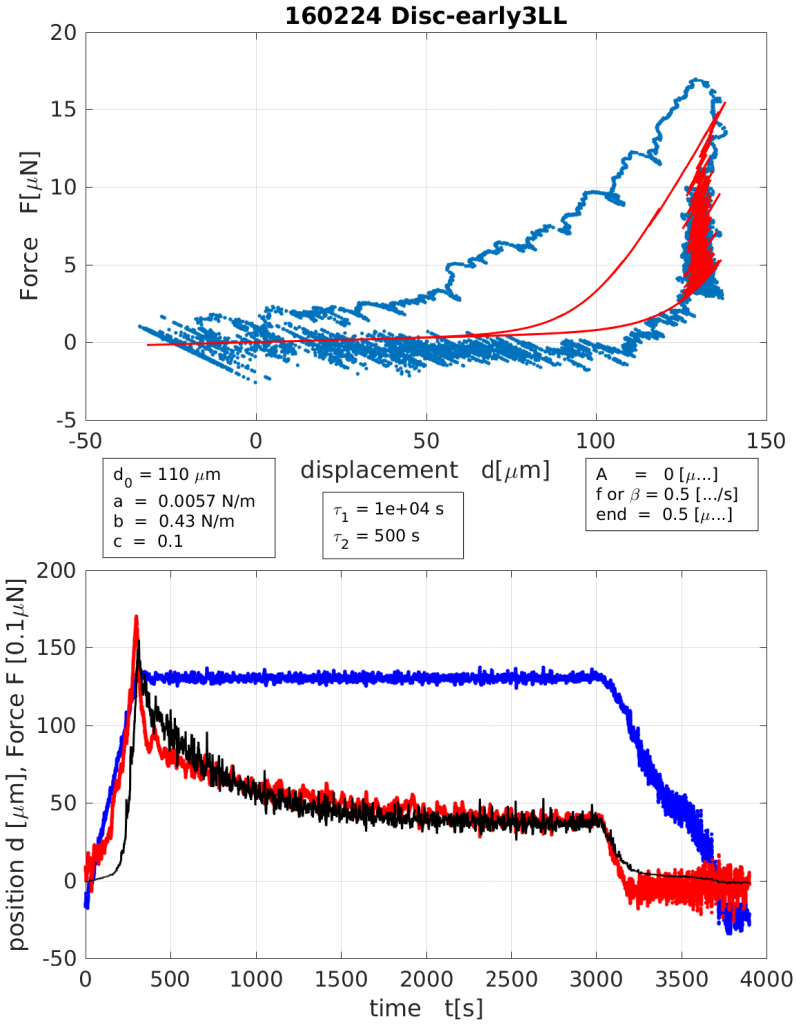
160224 Disc-early3LL
Force F[μN]
displacement d[μm]
d$_0$ = 110 μm
a = 0.0057 N/m
b = 0.43 N/m
c = 0.1
τ_1 = 1e+04 s
τ_2 = 500 s
A = 0 [μ...]
f or β = 0.5 [.../s]
end = 0.5 [μ...]
position d [μm], Force F [0.1μN]
time t[s]

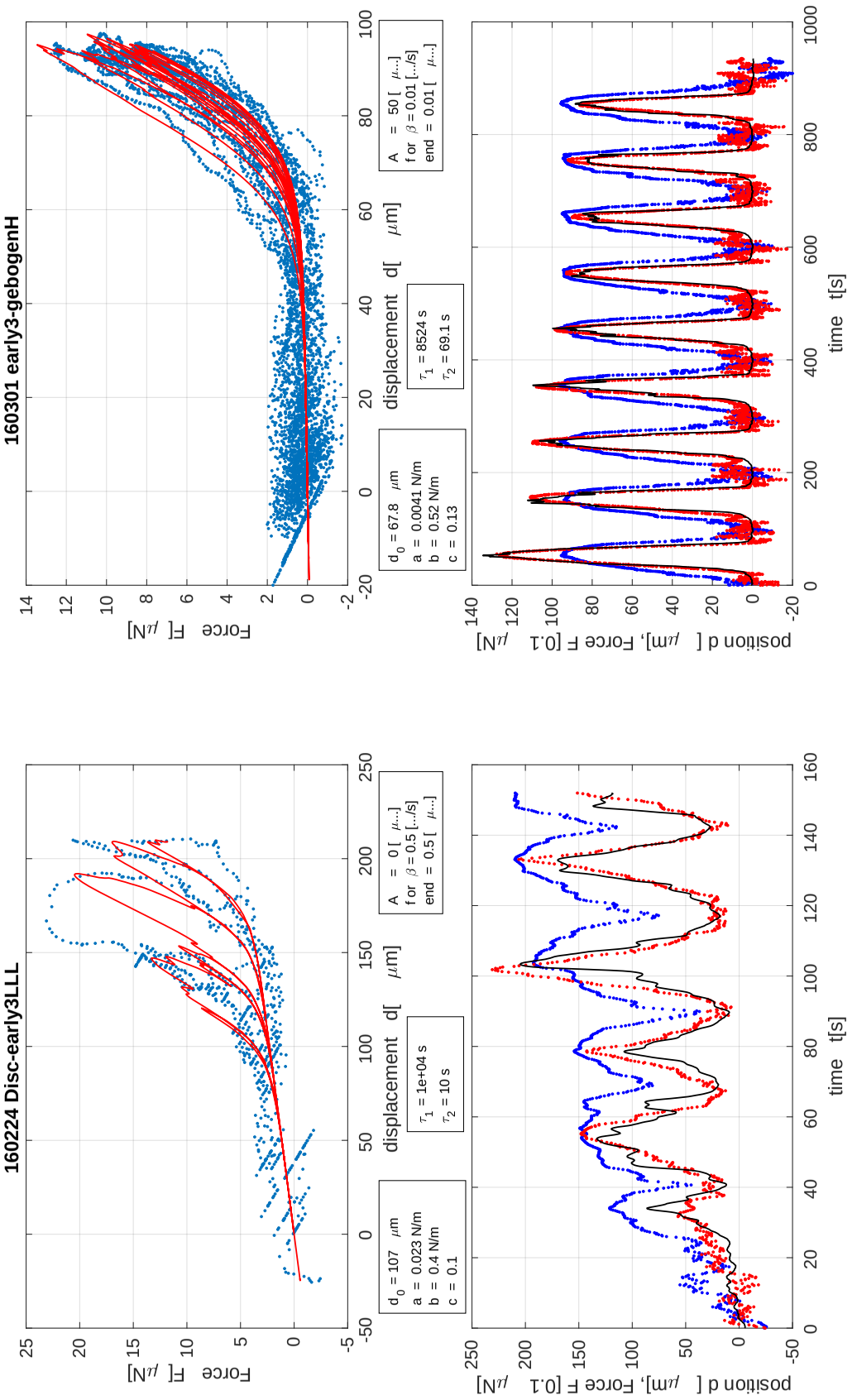
160301 early3-gebogenH
Force F[μN]
displacement d[μm]
d0 = 67.8 μm
a = 0.0041 N/m
b = 0.52 N/m
c = 0.13
τ1 = 8524 s
τ2 = 69.1 s
A = 50 [μ...]
for β = 0.01 [.../s]
end = 0.01 [μ...]
position d [μm], Force F [0.1 μN]
time t[s]
160224 Disc-early3LLL
Force F[μN]
displacement d[μm]
d0 = 107 μm
a = 0.023 N/m
b = 0.4 N/m
c = 0.1
τ1 = 1e+04 s
τ2 = 10 s
A = 0 [μ...]
for β = 0.5 [.../s]
end = 0.5 [μ...]
position d [μm], Force F [0.1 μN]
time t[s]

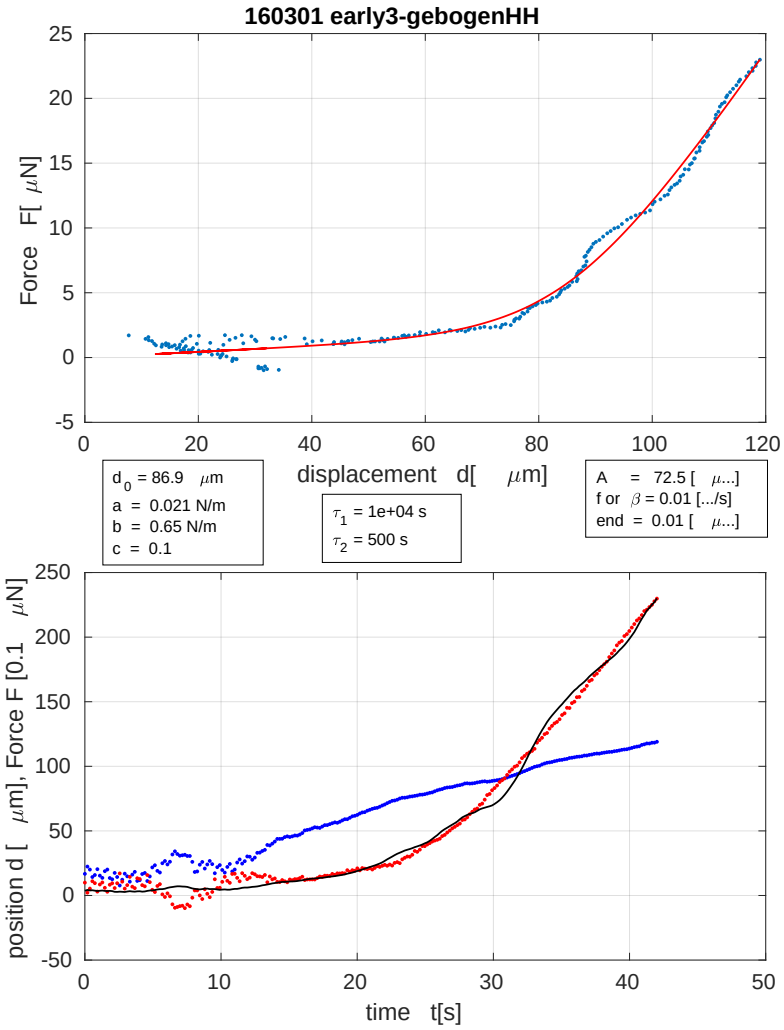
160301 early3-gebogenHH
Force F[μN]
displacement d[μm]
d0 = 86.9 μm
a = 0.021 N/m
b = 0.65 N/m
c = 0.1
τ1 = 1e+04 s
τ2 = 500 s
A = 72.5 [μ...]
f or β = 0.01 [.../s]
end = 0.01 [μ...]
position d [μm], Force F [0.1 μN]
time t[s]

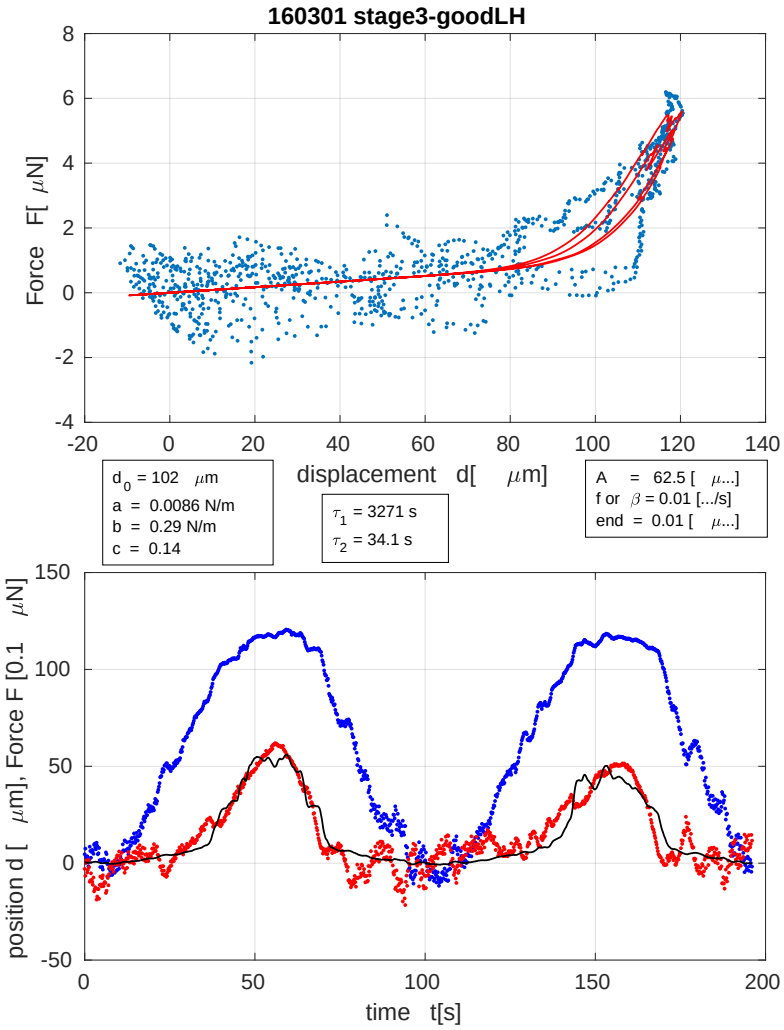
160301 stage3-goodLH
Force F[μN]
displacement d[μm]
d0 = 102 μm
a = 0.0086 N/m
b = 0.29 N/m
c = 0.14
τ1 = 3271 s
τ2 = 34.1 s
A = 62.5 [μ...]
f or β = 0.01 [.../s]
end = 0.01 [μ...]
position d [μm], Force F [0.1 μN]
time t[s]

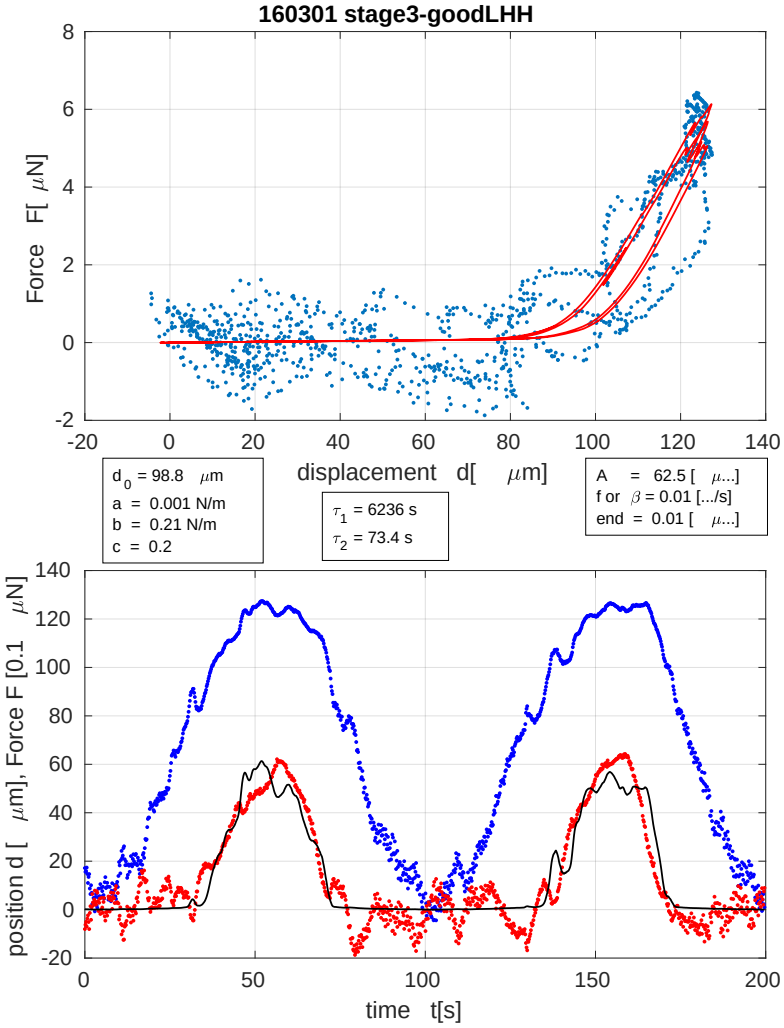
160301 stage3-goodLHH
Force F[μN]
displacement d[μm]
d0 = 98.8 μm
a = 0.001 N/m
b = 0.21 N/m
c = 0.2
τ1 = 6236 s
τ2 = 73.4 s
A = 62.5 [μ...]
f or β = 0.01 [.../s]
end = 0.01 [μ...]
position d [μm], Force F [0.1 μN]
time t[s]

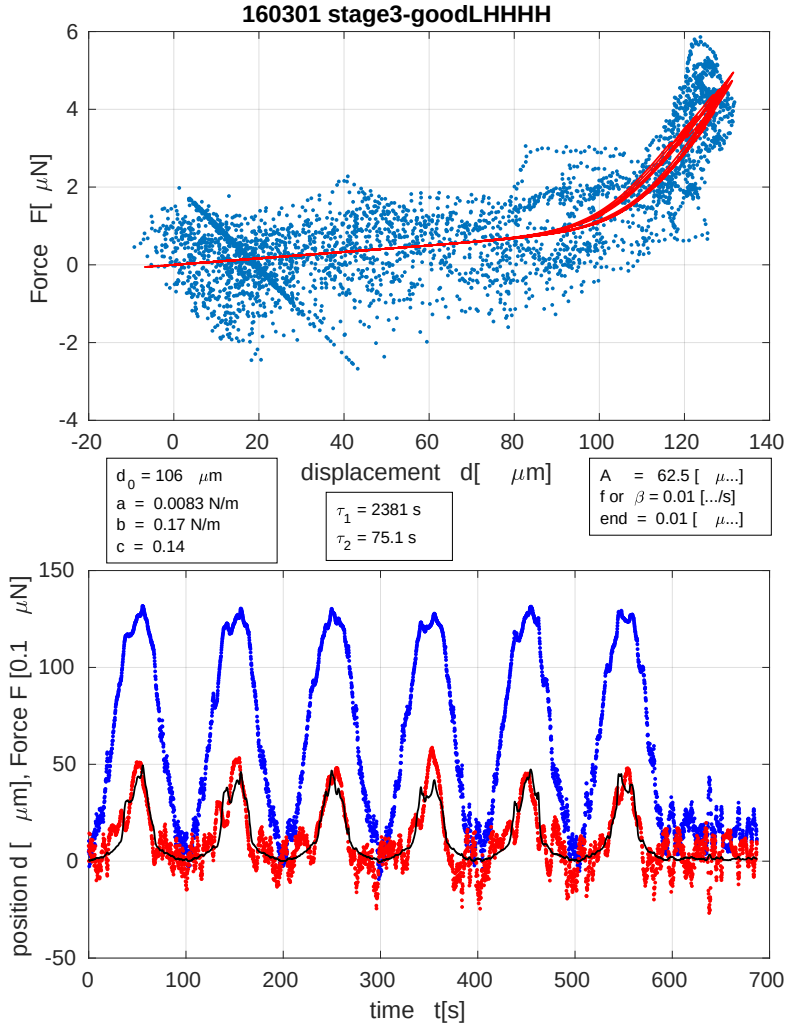
160301 stage3-goodLHHHH
Force F[μN]
displacement d[μm]
d0 = 106 μm
a = 0.0083 N/m
b = 0.17 N/m
c = 0.14
τ1 = 2381 s
τ2 = 75.1 s
A = 62.5 [μ...]
f or β = 0.01 [.../s]
end = 0.01 [μ...]
position d [μm], Force F [0.1 μN]
time t[s]

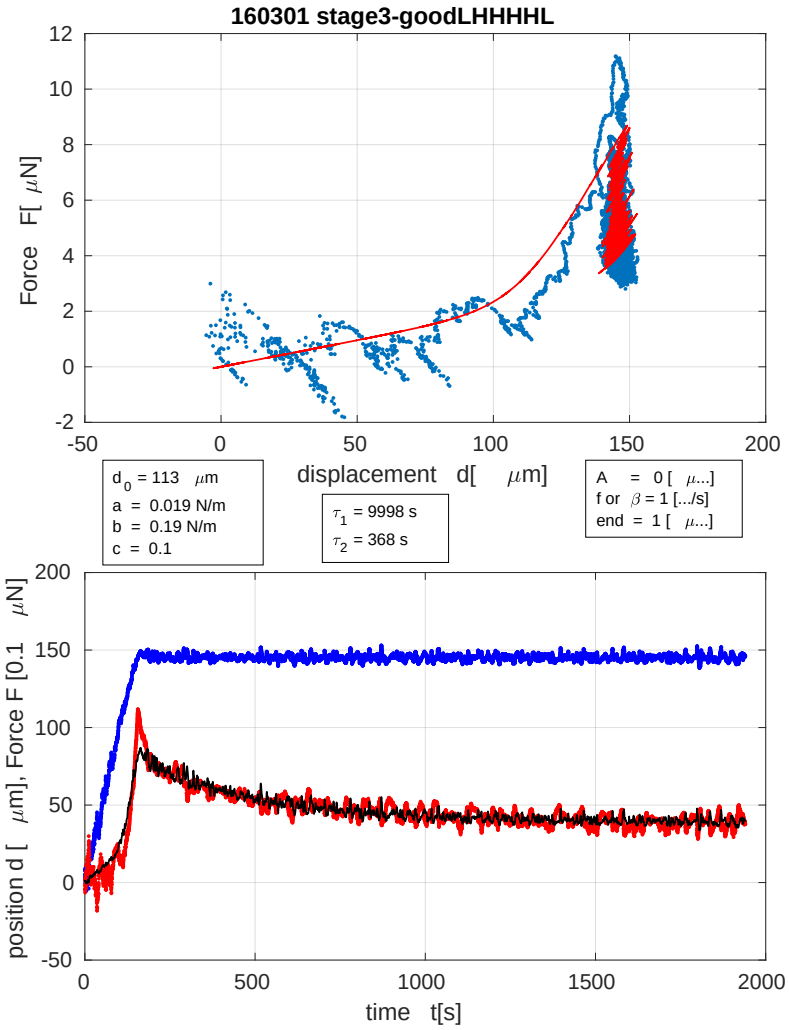
160301 stage3-goodLHHHHL
Force F[μN]
displacement d[μm]
d0 = 113 μm
a = 0.019 N/m
b = 0.19 N/m
c = 0.1
τ1 = 9998 s
τ2 = 368 s
A = 0 [μ...]
f or β = 1 [.../s]
end = 1 [μ...]
position d [μm], Force F [0.1 μN]
time t[s]

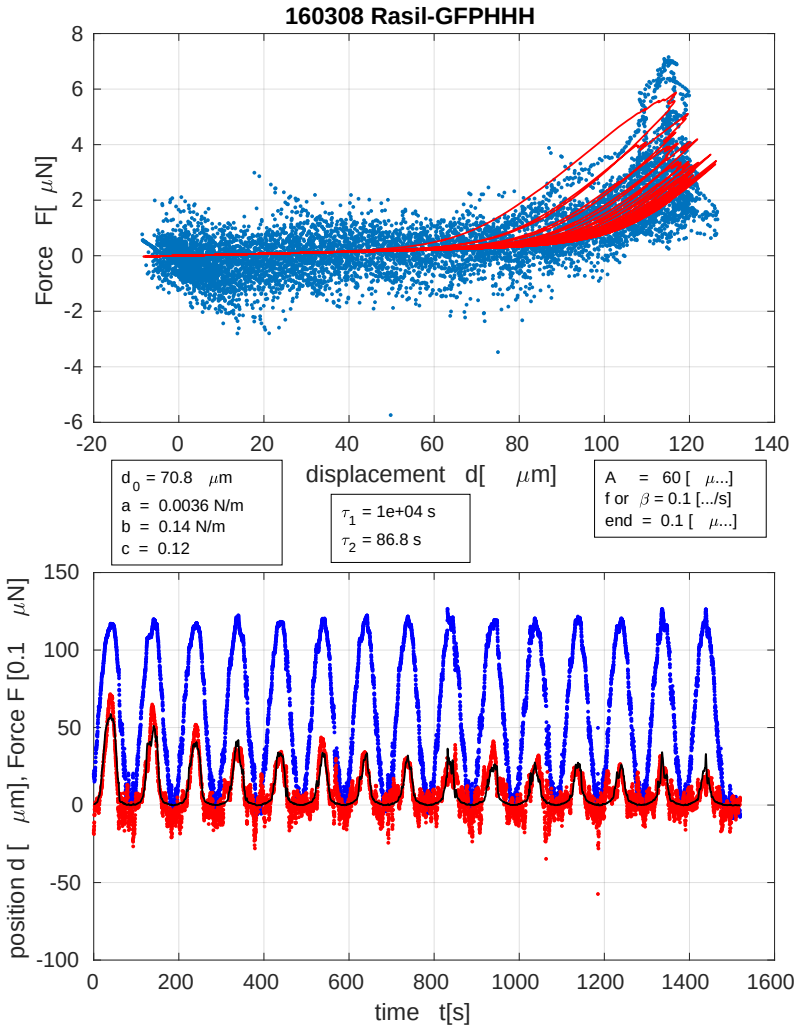
160308 Rasil-GFPHHH
Force F[μN]
displacement d[μm]
d0 = 70.8 μm
a = 0.0036 N/m
b = 0.14 N/m
c = 0.12
τ1 = 1e+04 s
τ2 = 86.8 s
A = 60 [μ...]
f or β = 0.1 [.../s]
end = 0.1 [μ...]
position d [μm], Force F [0.1 μN]
time t[s]

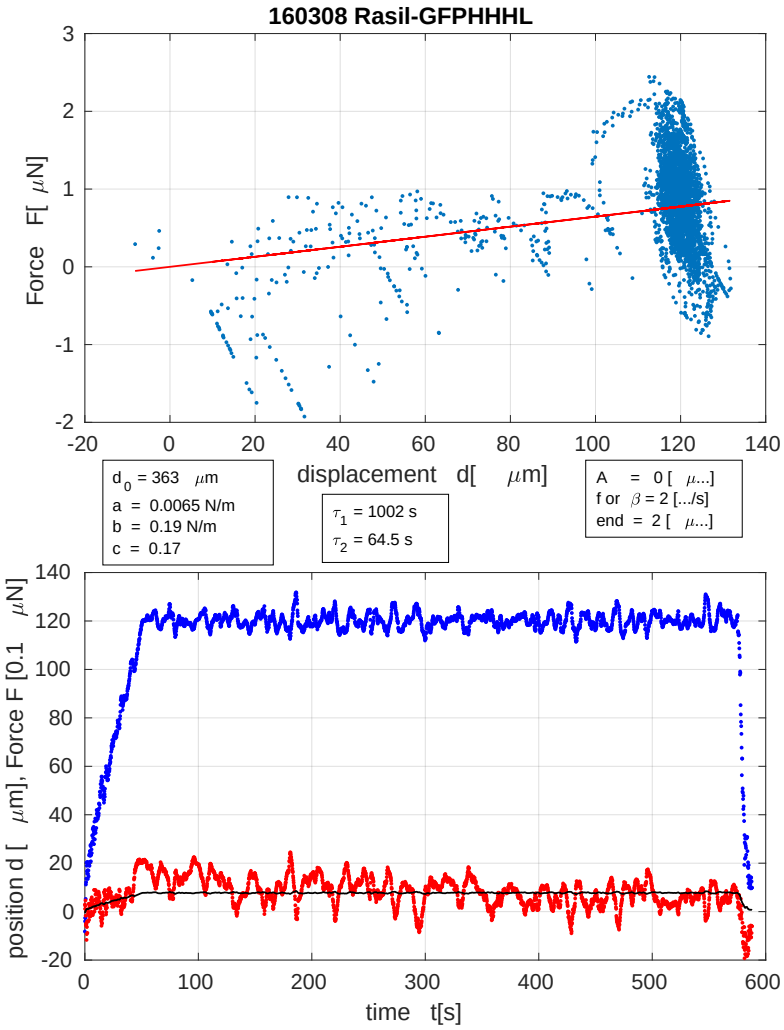
160308 Rasil-GFPHHHL
Force F[μN]
displacement d[μm]
d0 = 363 μm
a = 0.0065 N/m
b = 0.19 N/m
c = 0.17
τ1 = 1002 s
τ2 = 64.5 s
A = 0 [μ...]
f or β = 2 [.../s]
end = 2 [μ...]
position d [μm], Force F [0.1 μN]
time t[s]

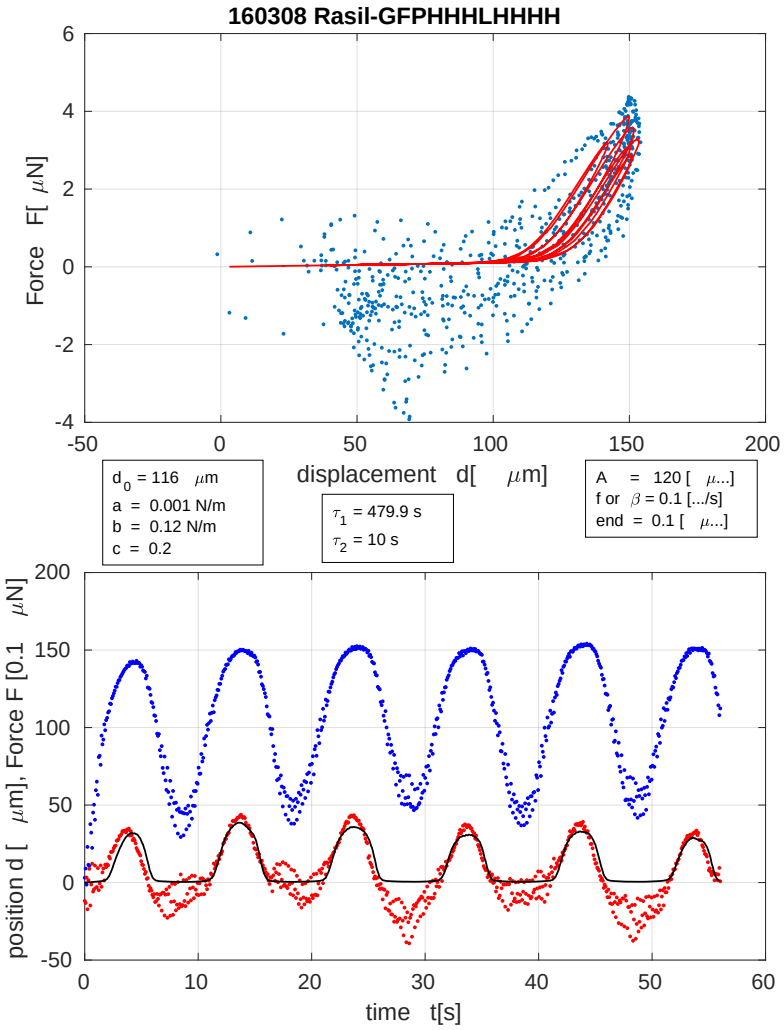
160308 Rasil-GFPHHHLHHHH
Force F[μN]
displacement d[μm]
d0 = 116 μm
a = 0.001 N/m
b = 0.12 N/m
c = 0.2
τ1 = 479.9 s
τ2 = 10 s
A = 120 [μ...]
f or β = 0.1 [.../s]
end = 0.1 [μ...]
position d [μm], Force F [0.1 μN]
time t[s]

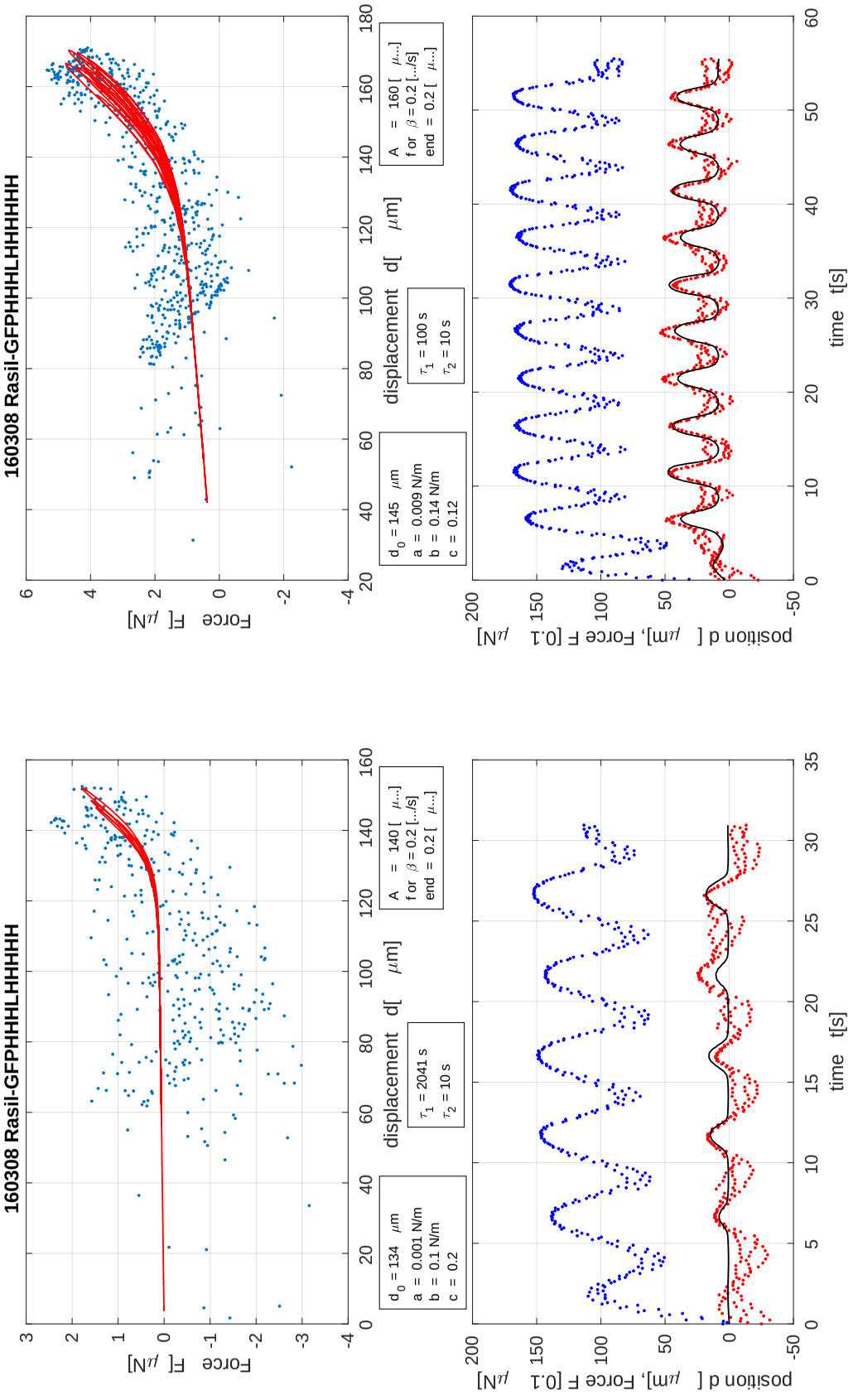
160308 Rasil-GFPHHHLHHHHH
Force F[μN]
displacement d[μm]
d0 = 134 μm
a = 0.001 N/m
b = 0.1 N/m
c = 0.2
τ1 = 2041 s
τ2 = 10 s
A = 140 [μ...]
for β = 0.2 [.../s]
end = 0.2 [μ...]
position d [μm], Force F [0.1 μN]
time t[s]
160308 Rasil-GFPHHHLHHHHH
Force F[μN]
displacement d[μm]
d0 = 145 μm
a = 0.009 N/m
b = 0.14 N/m
c = 0.12
τ1 = 100 s
τ2 = 10 s
A = 160 [μ...]
for β = 0.2 [.../s]
end = 0.2 [μ...]
position d [μm], Force F [0.1 μN]
time t[s]

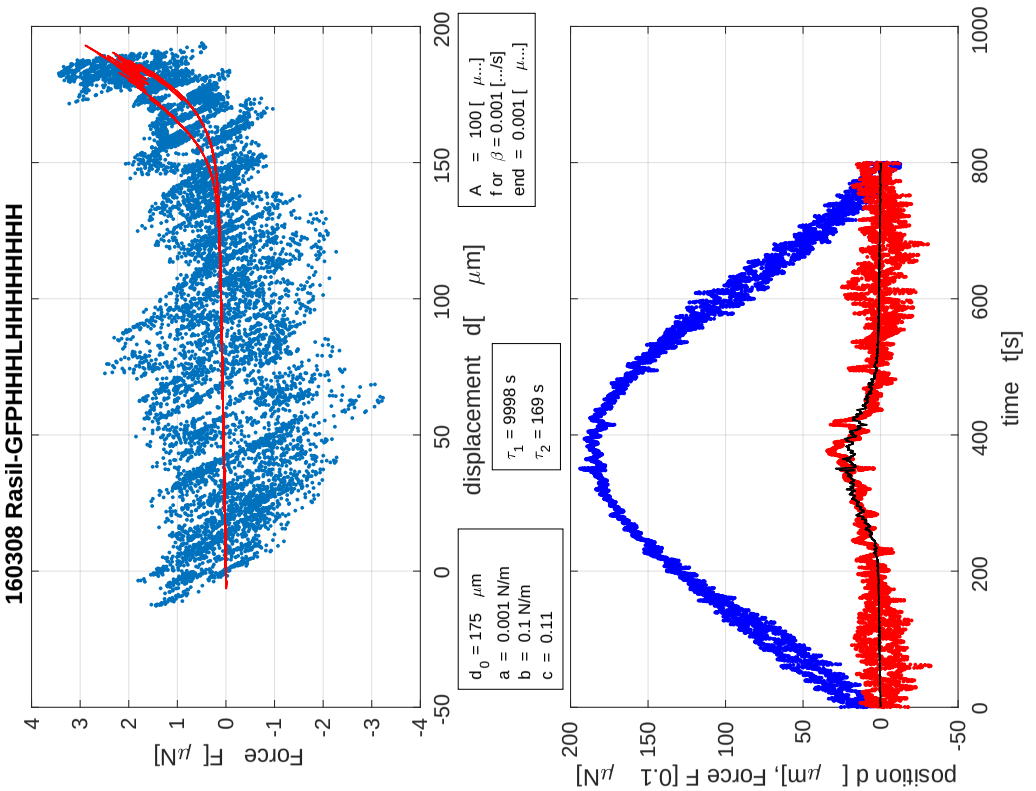
160308 Rasil-GFPHHHLHHHHHHHH
Force F[μN]
displacement d[μm]
d0 = 175 μm
a = 0.001 N/m
b = 0.1 N/m
c = 0.11
τ1 = 9998 s
τ2 = 169 s
A = 100 [μ...]
for β = 0.001 [.../s]
end = 0.001 [μ...]
position d [μm], Force F [0.1 μN]
time t[s]

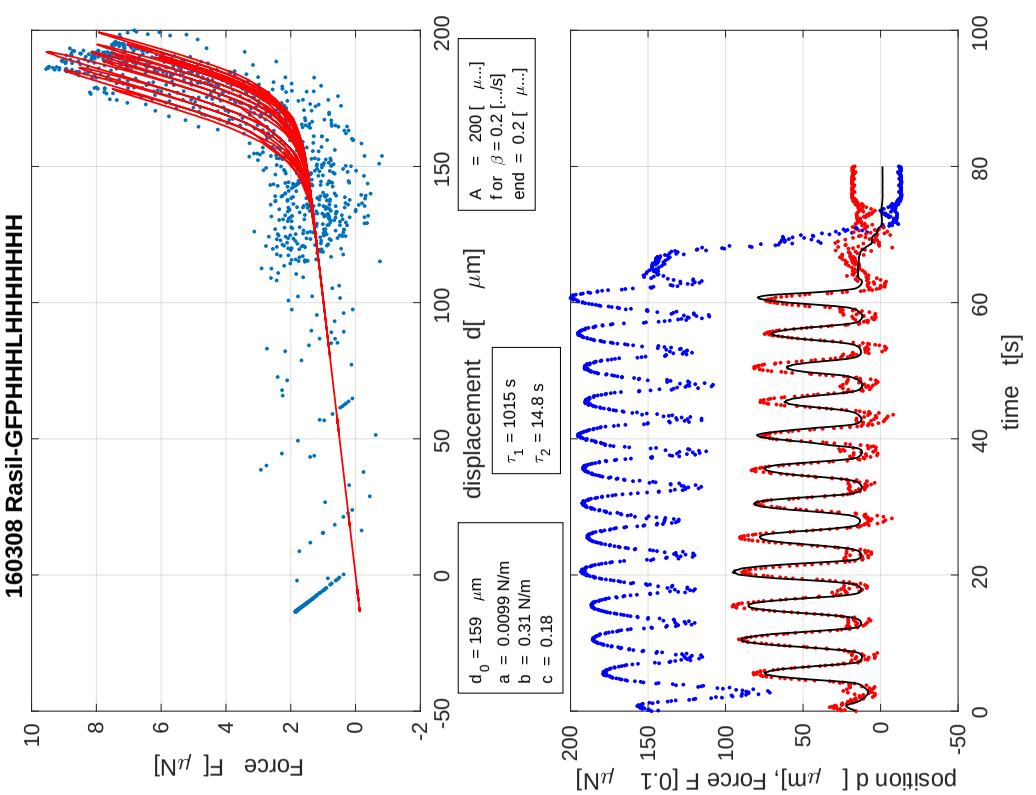
160308 Rasil-GFPHHHLHHHHHHHH
Force F[μN]
displacement d[μm]
d0 = 159 μm
a = 0.0099 N/m
b = 0.31 N/m
c = 0.18
τ1 = 1015 s
τ2 = 14.8 s
A = 200 [μ...]
for β = 0.2 [.../s]
end = 0.2 [μ...]
position d [μm], Force F [0.1 μN]
time t[s]

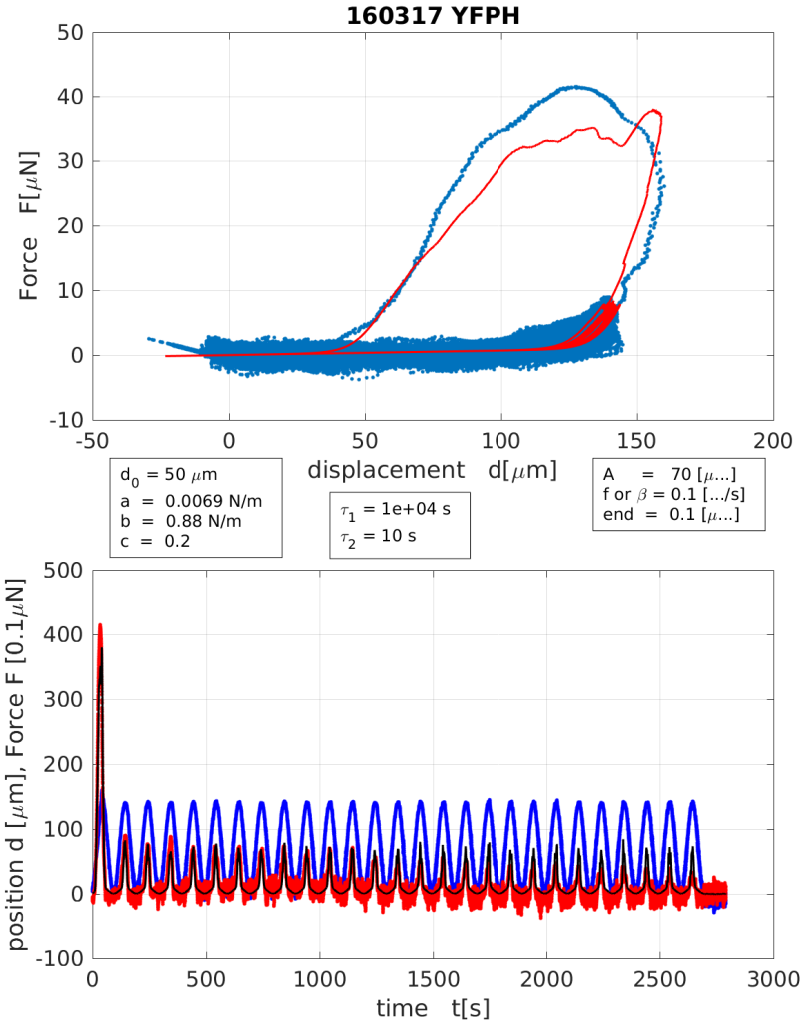
160317 YFPH
Force F[μN]
displacement d[μm]
d0 = 50 μm
a = 0.0069 N/m
b = 0.88 N/m
c = 0.2
τ1 = 1e+04 s
τ2 = 10 s
A = 70 [μ...]
f or β = 0.1 [.../s]
end = 0.1 [μ...]
position d [μm], Force F [0.1μN]
time t[s]

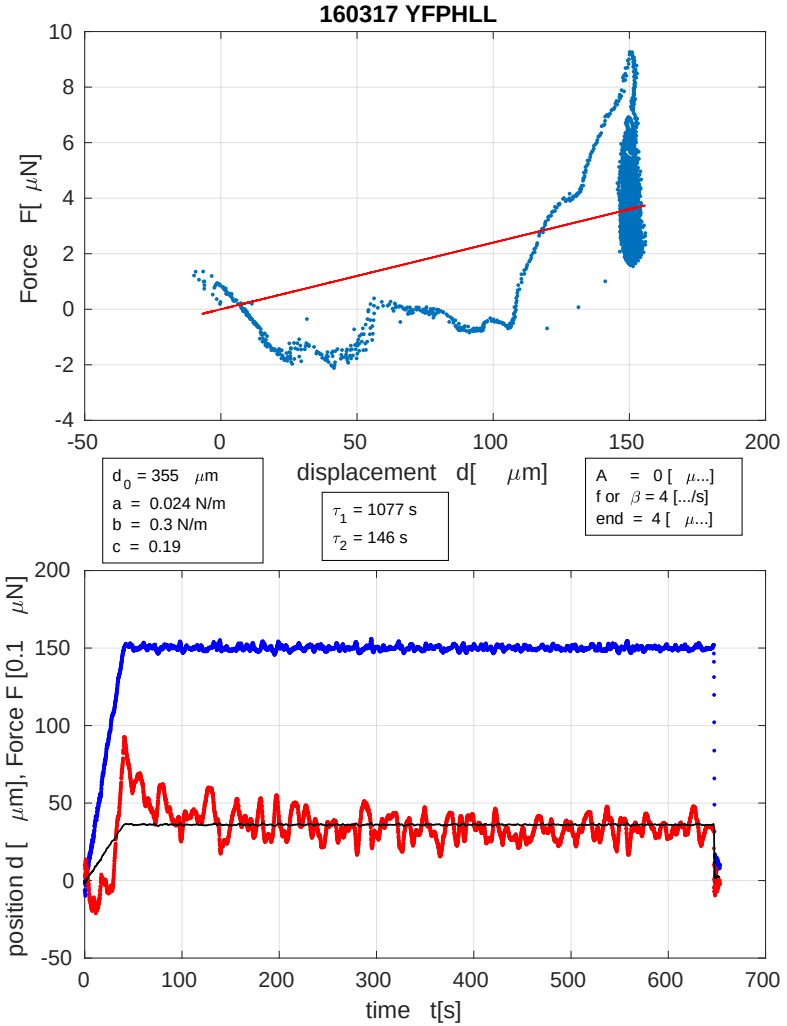
160317 YFPHLL
Force F[μN]
displacement d[μm]
d0 = 355 μm
a = 0.024 N/m
b = 0.3 N/m
c = 0.19
τ1 = 1077 s
τ2 = 146 s
A = 0 [μ...]
f or β = 4 [.../s]
end = 4 [μ...]
position d [μm], Force F [0.1 μN]
time t[s]

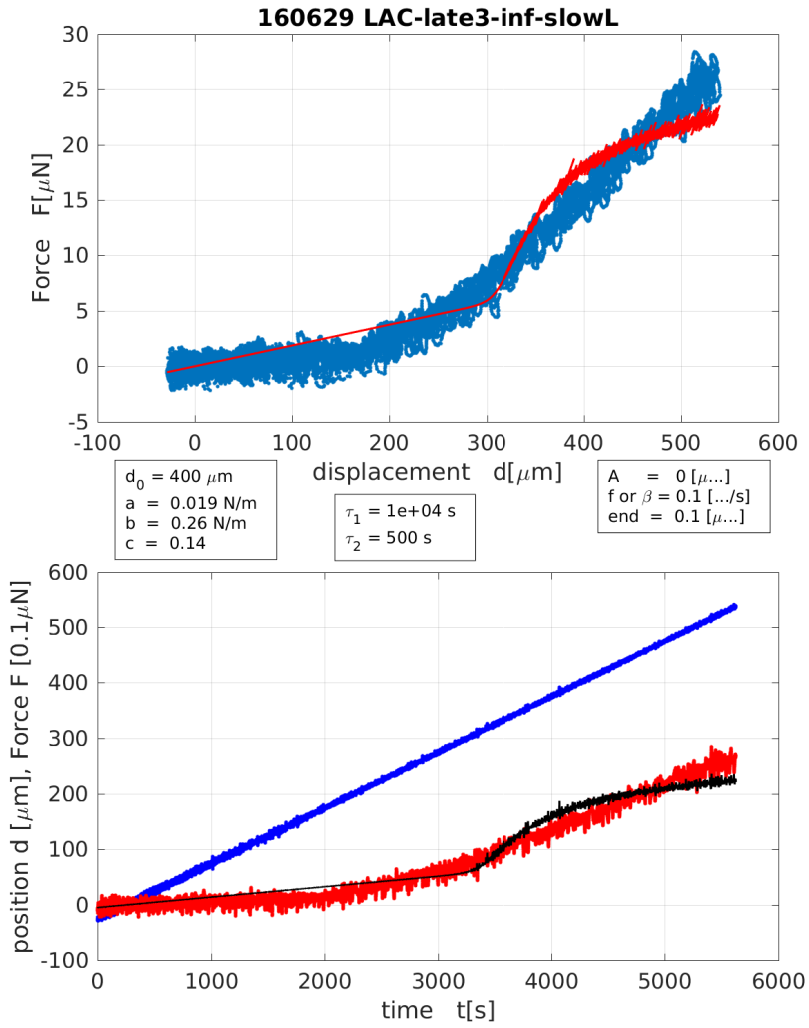
160629 LAC-late3-inf-slowL
Force F[μN]
displacement d[μm]
d0 = 400 μm
a = 0.019 N/m
b = 0.26 N/m
c = 0.14
τ1 = 1e+04 s
τ2 = 500 s
A = 0 [μ...]
f or β = 0.1 [.../s]
end = 0.1 [μ...]
position d [μm], Force F [0.1μN]
time t[s]

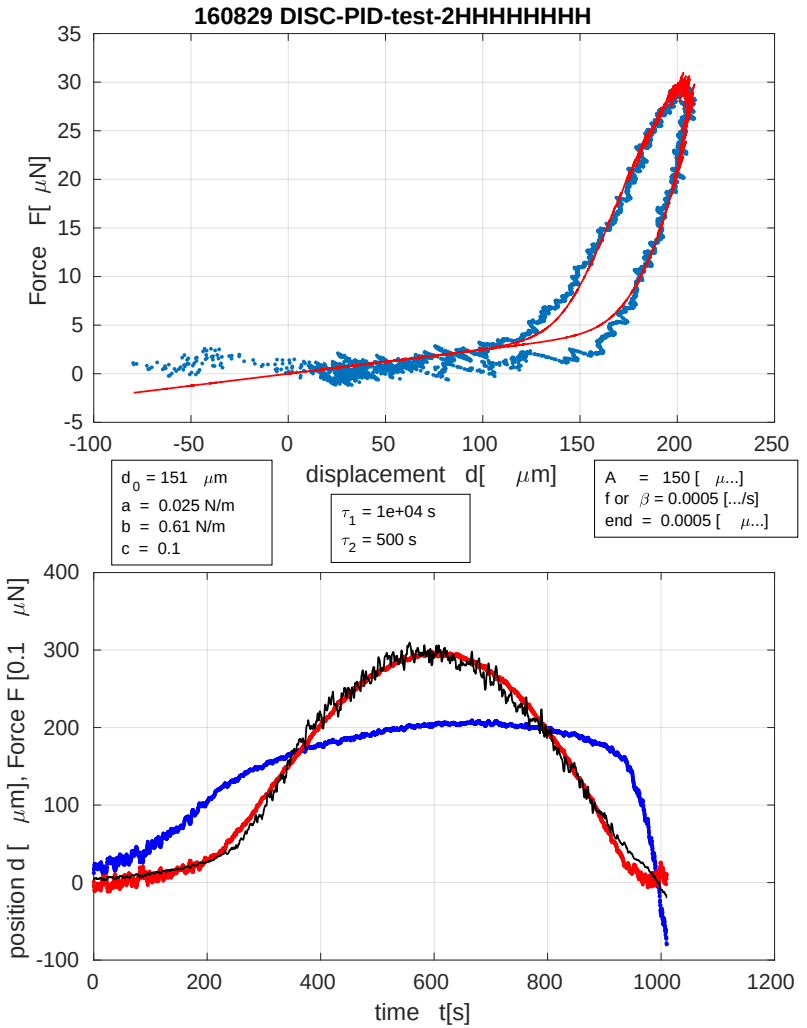
160829 DISC-PID-test-2HHHHHHHH
Force F[μN]
displacement d[μm]
d0 = 151 μm
a = 0.025 N/m
b = 0.61 N/m
c = 0.1
τ1 = 1e+04 s
τ2 = 500 s
A = 150 [μ...]
f or β = 0.0005 [.../s]
end = 0.0005 [μ...]
position d [μm], Force F [0.1 μN]
time t[s]

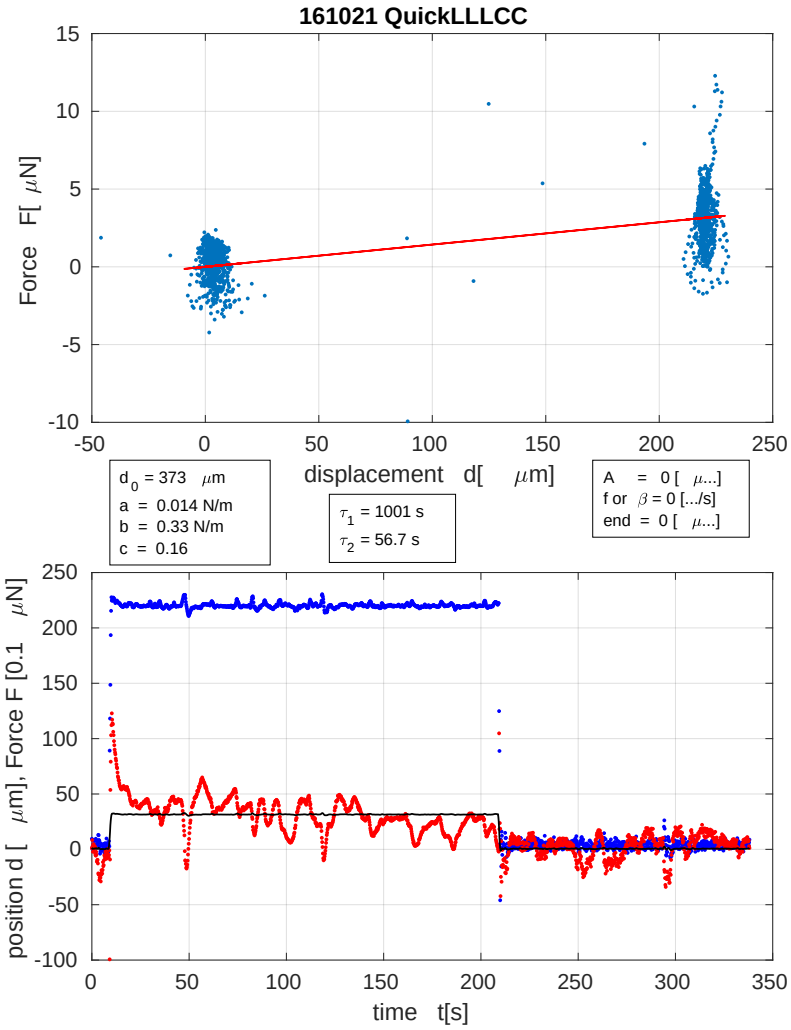
161021 QuickLLLCC
Force F[μN]
displacement d[μm]
d0 = 373 μm
a = 0.014 N/m
b = 0.33 N/m
c = 0.16
τ1 = 1001 s
τ2 = 56.7 s
A = 0 [μ...]
f or β = 0 [.../s]
end = 0 [μ...]
position d [μm], Force F [0.1 μN]
time t[s]

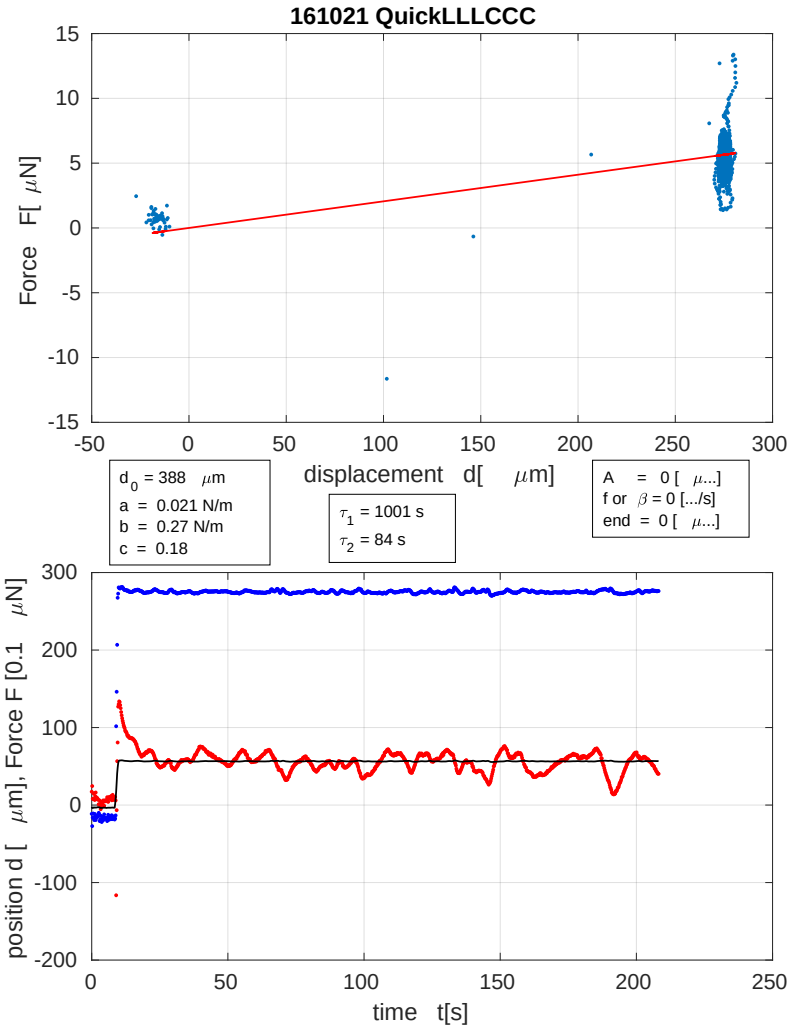
161021 QuickLLLCCC
Force F[μN]
displacement d[μm]
d0 = 388 μm
a = 0.021 N/m
b = 0.27 N/m
c = 0.18
τ1 = 1001 s
τ2 = 84 s
A = 0 [μ...]
f or β = 0 [.../s]
end = 0 [μ...]
position d [μm], Force F [0.1 μN]
time t[s]

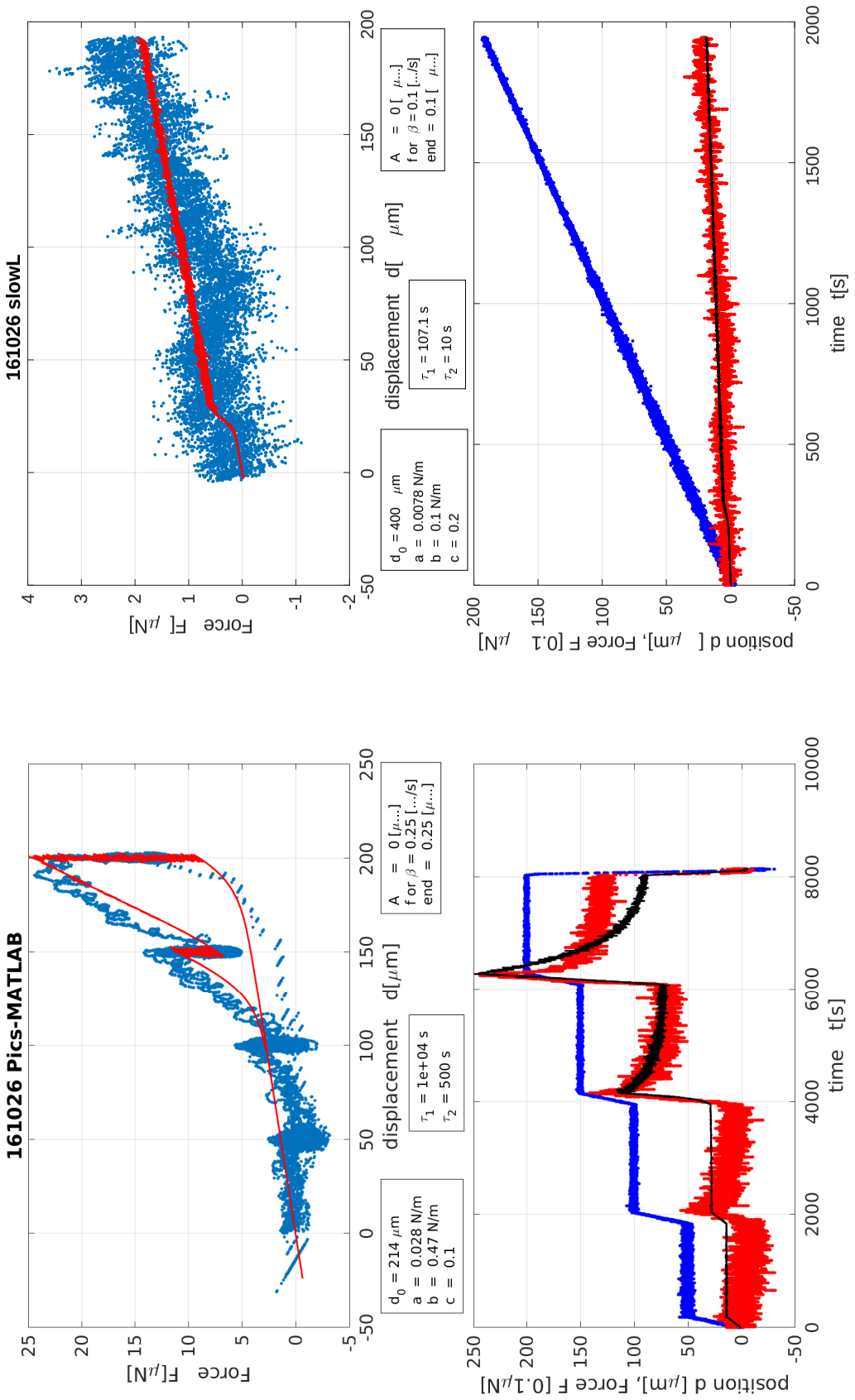
161026 slowL
Force F[μN]
displacement d[μm]
d0 = 400 μm
a = 0.0078 N/m
b = 0.1 N/m
c = 0.2
τ1 = 107.1 s
τ2 = 10 s
A = 0 [μ...]
for β = 0.1 [.../s]
end = 0.1 [μ...]
position d [μm], Force F [0.1 μN]
time t[s]
161026 Pics-MATLAB
Force F[μN]
displacement d[μm]
d0 = 214 μm
a = 0.028 N/m
b = 0.47 N/m
c = 0.1
τ1 = 1e+04 s
τ2 = 500 s
A = 0 [μ...]
for β = 0.25 [.../s]
end = 0.25 [μ...]
position d [μm], Force F [0.1μN]
time t[s]

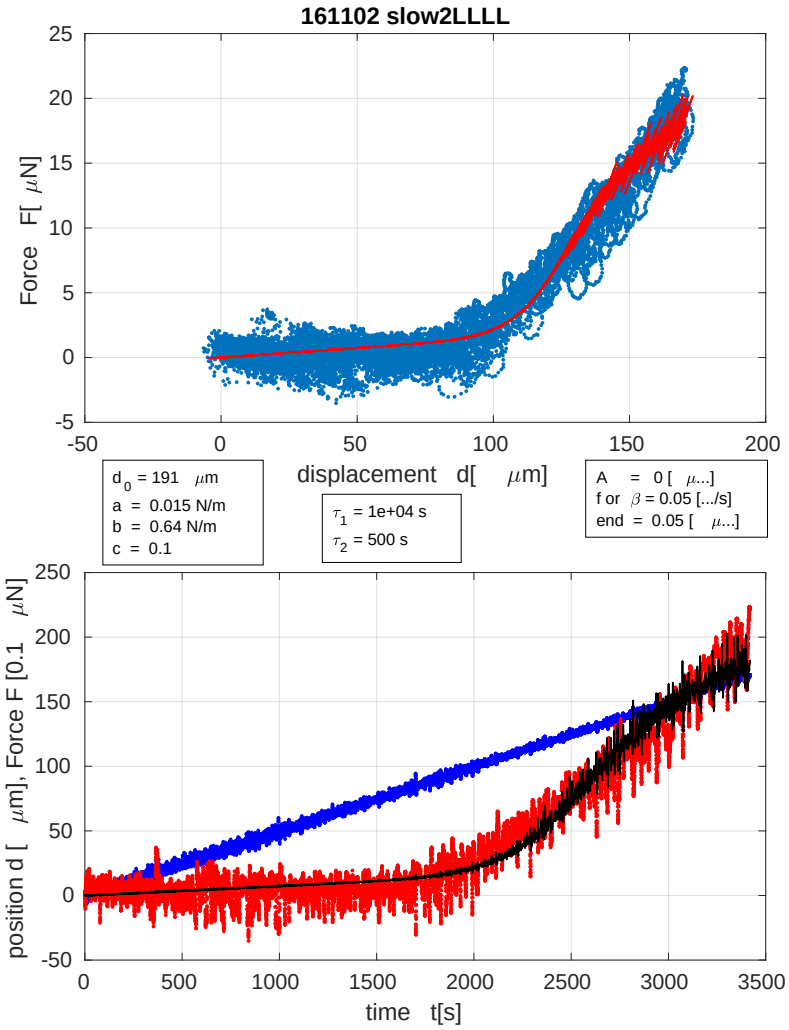
161102 slow2LLLL
Force F[μN]
displacement d[μm]
d0 = 191 μm
a = 0.015 N/m
b = 0.64 N/m
c = 0.1
τ1 = 1e+04 s
τ2 = 500 s
A = 0 [μ...]
f or β = 0.05 [.../s]
end = 0.05 [μ...]
position d [μm], Force F [0.1 μN]
time t[s]

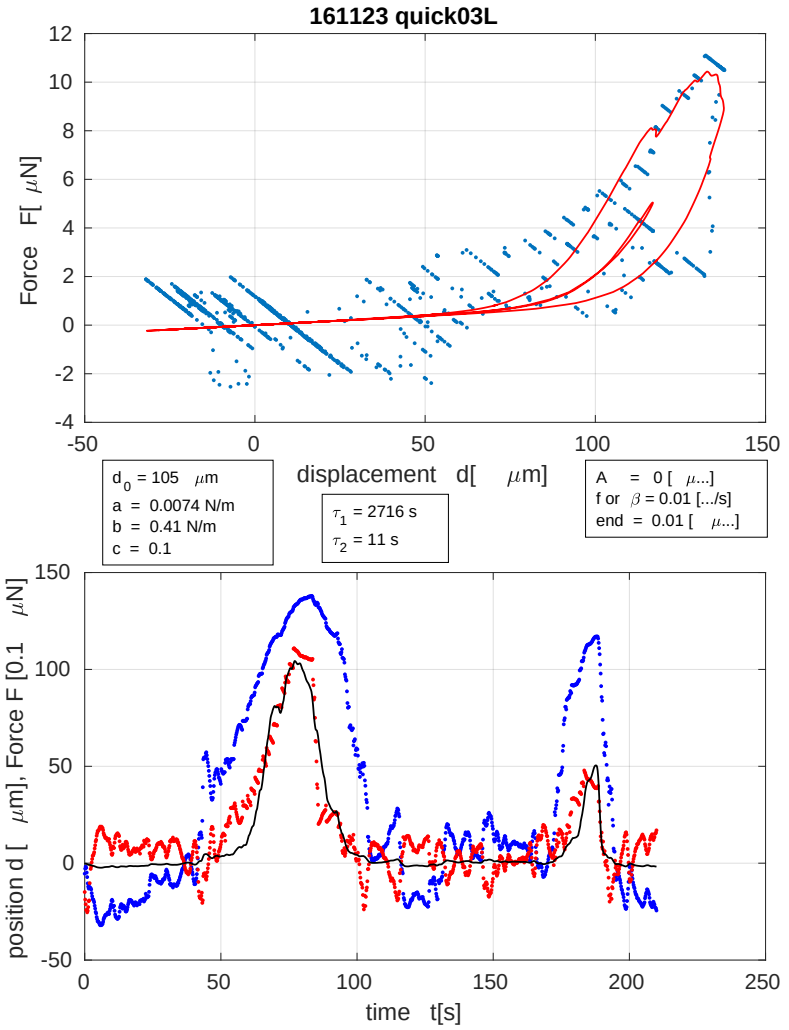
161123 quick03L
Force F[μN]
displacement d[μm]
d0 = 105 μm
a = 0.0074 N/m
b = 0.41 N/m
c = 0.1
τ1 = 2716 s
τ2 = 11 s
A = 0 [μ...]
f or β = 0.01 [.../s]
end = 0.01 [μ...]
position d [μm], Force F [0.1 μN]
time t[s]

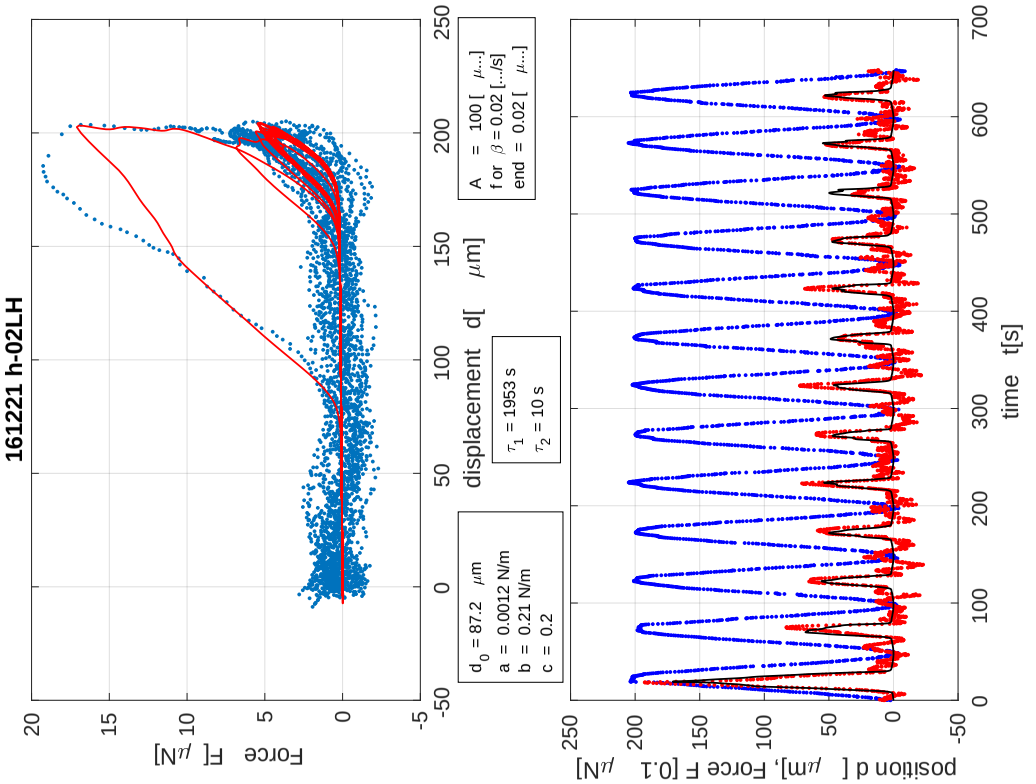
161221 h-02LH
Force F[μN]
displacement d[μm]
d0 = 87.2 μm
a = 0.0012 N/m
b = 0.21 N/m
c = 0.2
τ1 = 1953 s
τ2 = 10 s
A = 100 [μ...]
for β = 0.02 [.../s]
end = 0.02 [μ...]
position d [μm], Force F [0.1 μN]
time t[s]

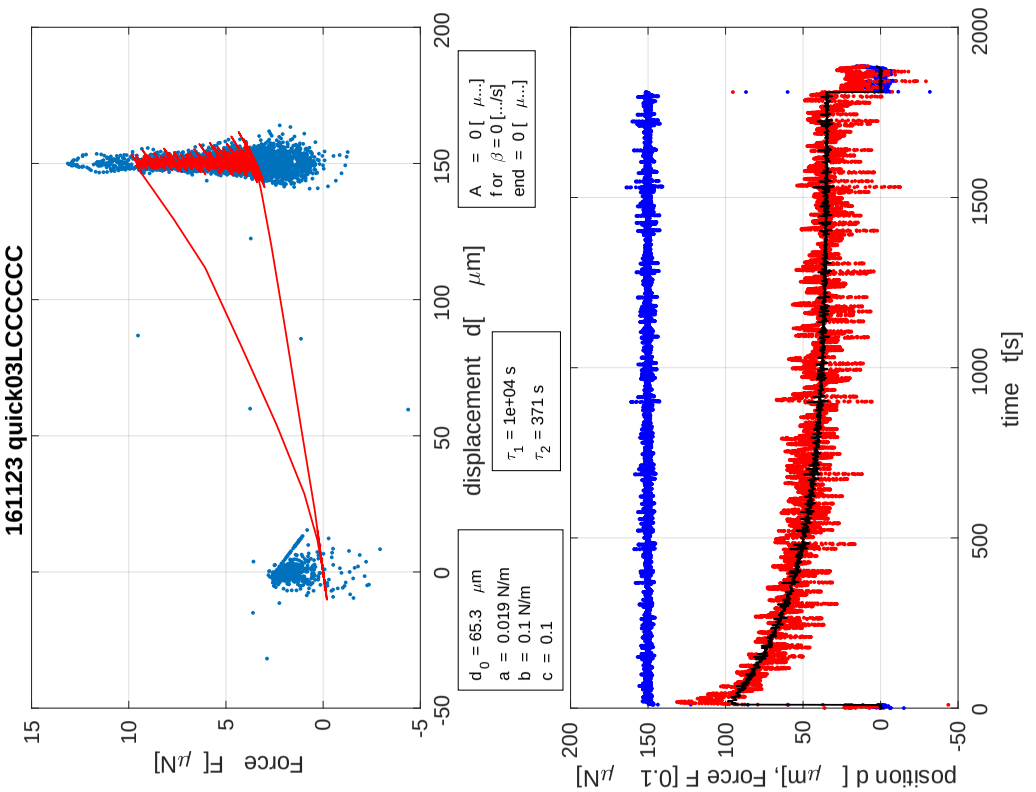
161123 quick03LCCCCCC
Force F[μN]
displacement d[μm]
d0 = 65.3 μm
a = 0.019 N/m
b = 0.1 N/m
c = 0.1
τ1 = 1e+04 s
τ2 = 371 s
A = 0 [μ...]
for β = 0 [.../s]
end = 0 [μ...]
position d [μm], Force F [0.1 μN]
time t[s]

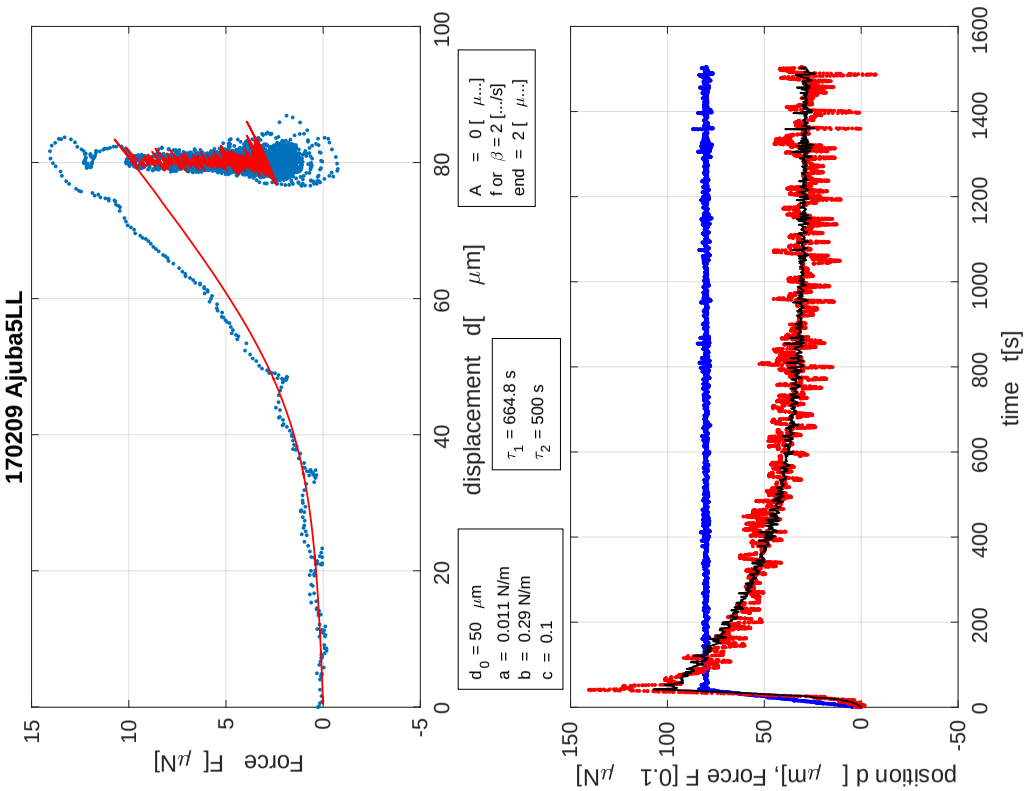
170209 Ajuba5LL
Force F[μN]
displacement d[μm]
d0 = 50 μm
a = 0.011 N/m
b = 0.29 N/m
c = 0.1
τ1 = 664.8 s
τ2 = 500 s
A = 0 [μ...]
for β = 2 [.../s]
end = 2 [μ...]
position d [μm], Force F [0.1 μN]
time t[s]

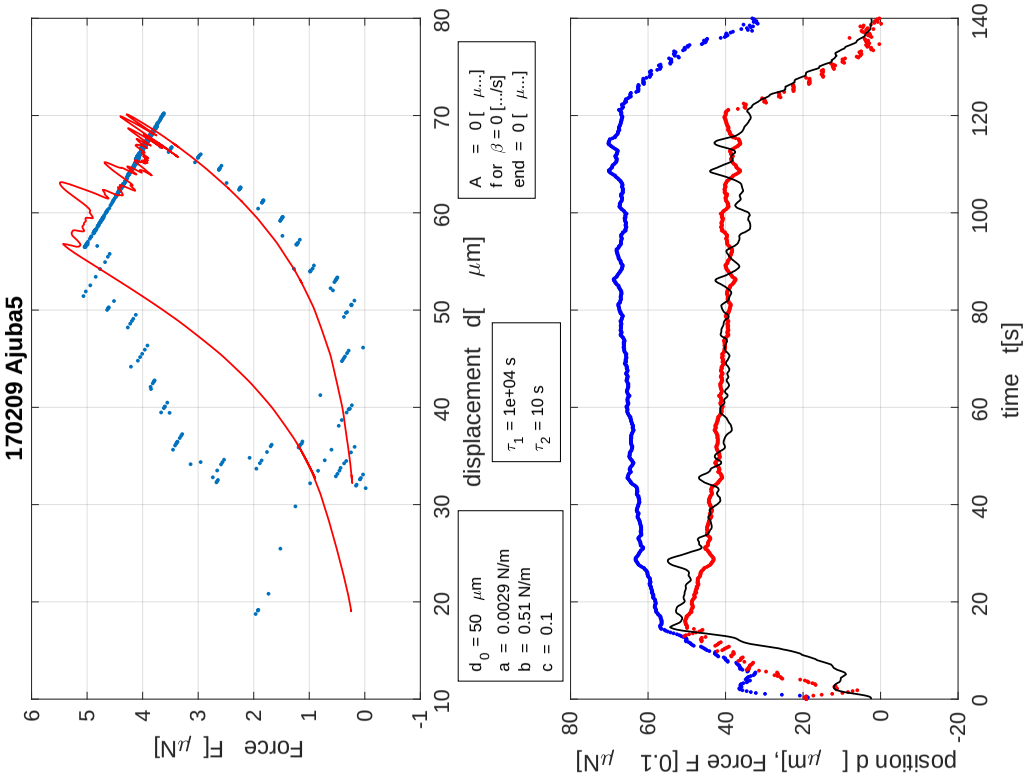
170209 Ajuba5
Force F[μN]
displacement d[μm]
d0 = 50 μm
a = 0.0029 N/m
b = 0.51 N/m
c = 0.1
τ1 = 1e+04 s
τ2 = 10 s
A = 0 [μ...]
for β = 0 [.../s]
end = 0 [μ...]
position d [μm], Force F [0.1 μN]
time t[s]

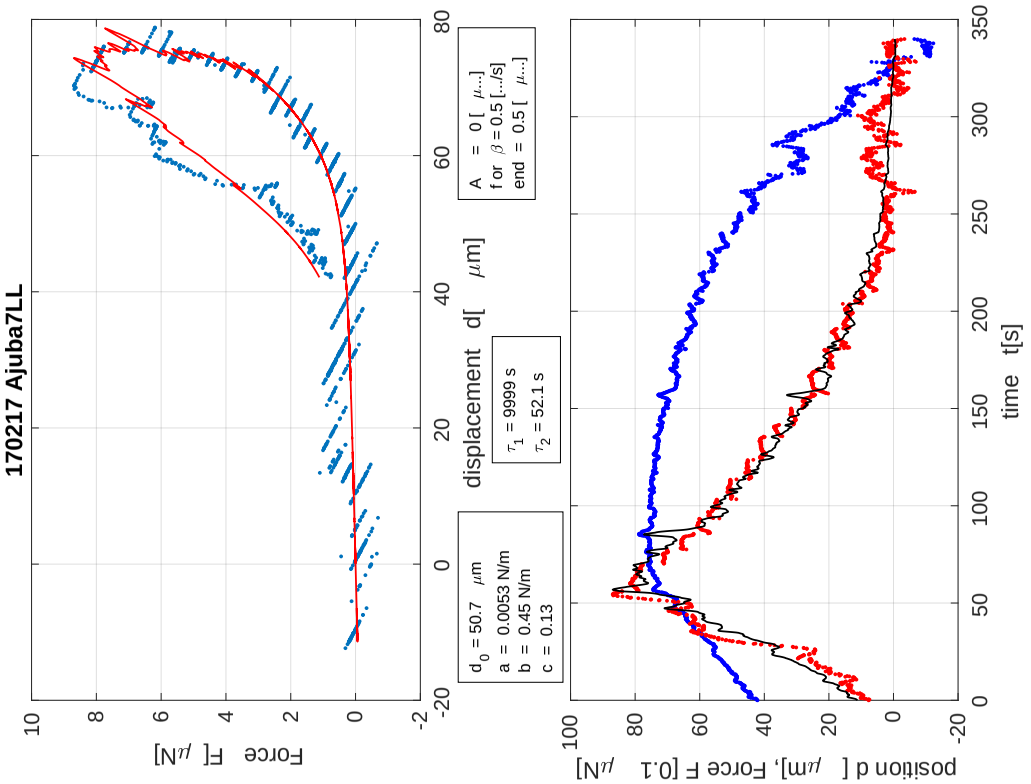
170217 Ajuba7LL
Force F[μN]
displacement d[μm]
d0 = 50.7 μm
a = 0.0053 N/m
b = 0.45 N/m
c = 0.13
τ1 = 9999 s
τ2 = 52.1 s
A = 0 [μ...]
for β = 0.5 [.../s]
end = 0.5 [μ...]
position d [μm], Force F [0.1 μN]
time t[s]

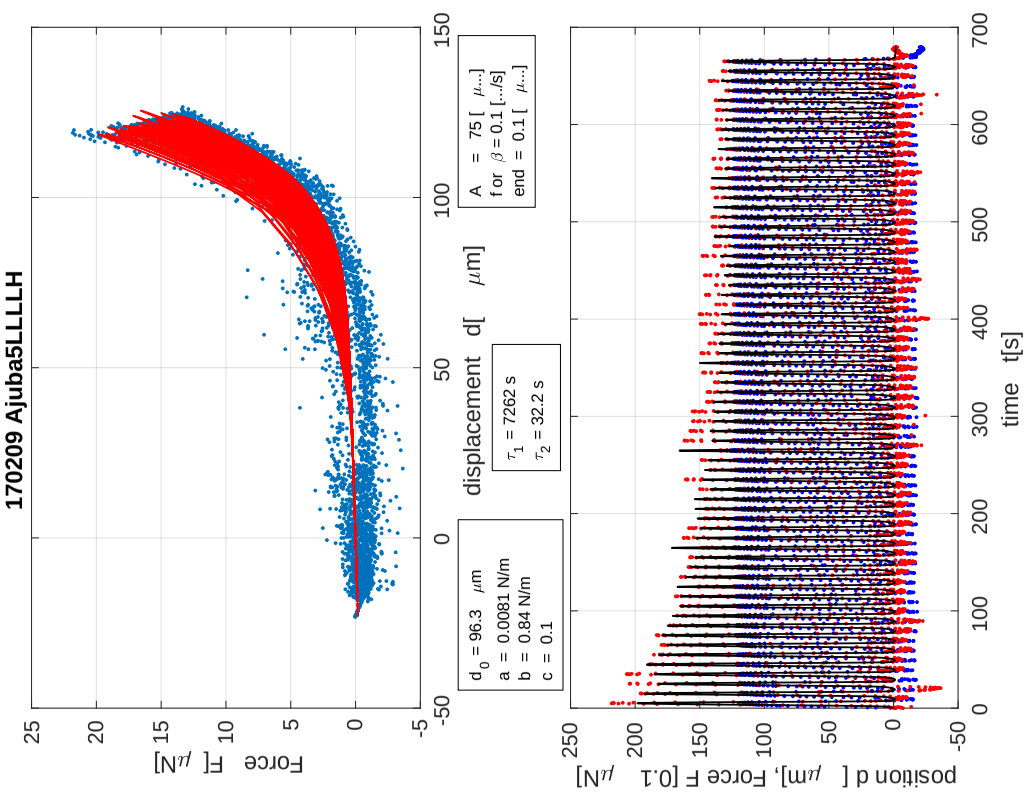
170209 Ajuba5LLLLH
Force F[μN]
displacement d[μm]
d0 = 96.3 μm
a = 0.0081 N/m
b = 0.84 N/m
c = 0.1
τ1 = 7262 s
τ2 = 32.2 s
A = 75 [μ...]
for β = 0.1 [.../s]
end = 0.1 [μ...]
position d [μm], Force F [0.1 μN]
time t[s]

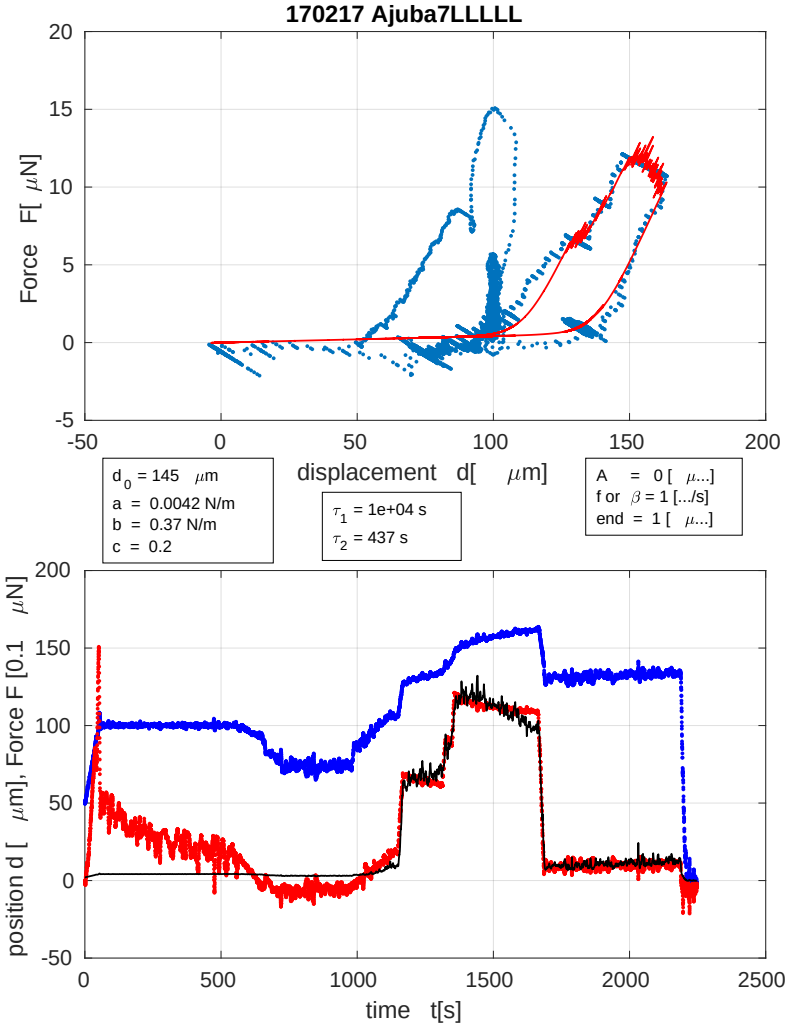
170217 Ajuba7LLLLL
Force F[μN]
displacement d[μm]
d0 = 145 μm
a = 0.0042 N/m
b = 0.37 N/m
c = 0.2
τ1 = 1e+04 s
τ2 = 437 s
A = 0 [μ...]
f or β = 1 [.../s]
end = 1 [μ...]
position d [μm], Force F [0.1 μN]
time t[s]

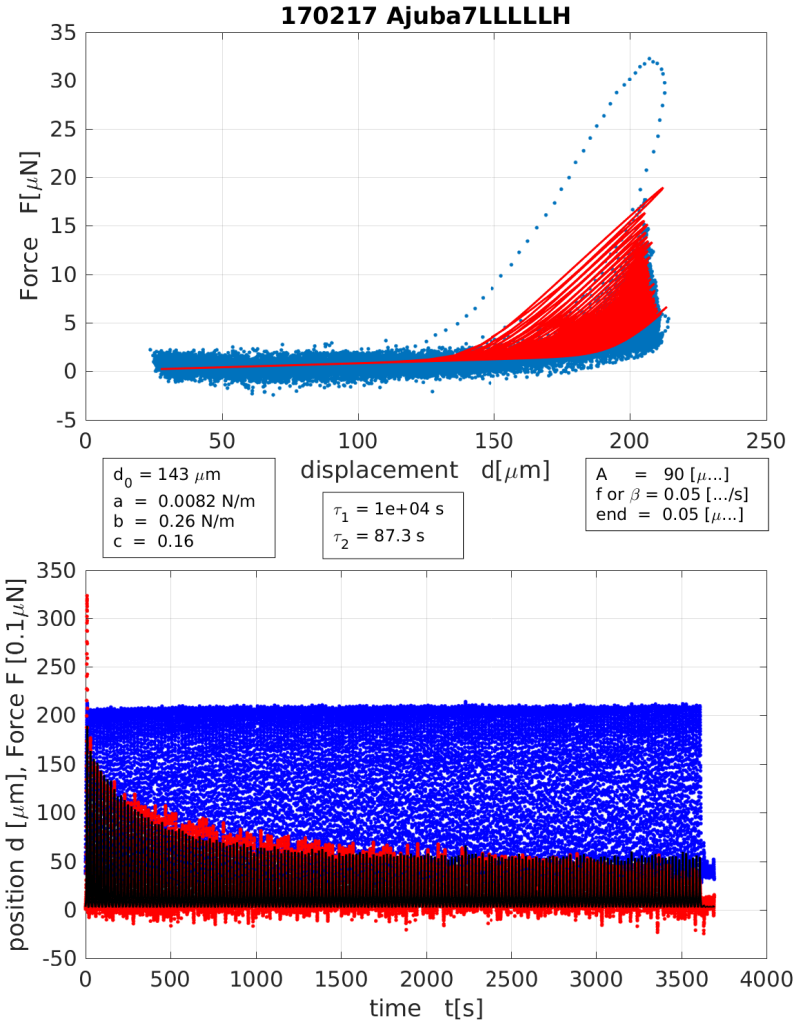
170217 Ajuba7LLLLLH
Force F[μN]
displacement d[μm]
d0 = 143 μm
a = 0.0082 N/m
b = 0.26 N/m
c = 0.16
τ1 = 1e+04 s
τ2 = 87.3 s
A = 90 [μ...]
f or β = 0.05 [.../s]
end = 0.05 [μ...]
position d [μm], Force F [0.1μN]
time t[s]

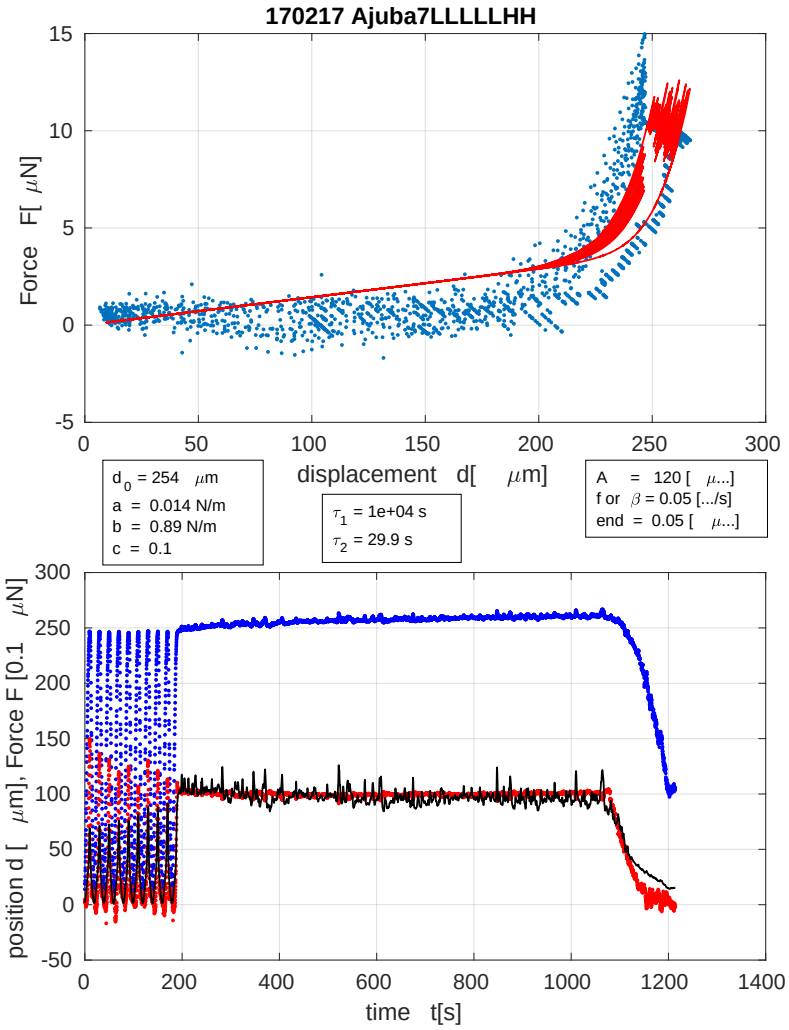
170217 Ajuba7LLLLLHH
Force F[μN]
displacement d[μm]
d0 = 254 μm
a = 0.014 N/m
b = 0.89 N/m
c = 0.1
τ1 = 1e+04 s
τ2 = 29.9 s
A = 120 [μ...]
f or β = 0.05 [.../s]
end = 0.05 [μ...]
position d [μm], Force F [0.1 μN]
time t[s]

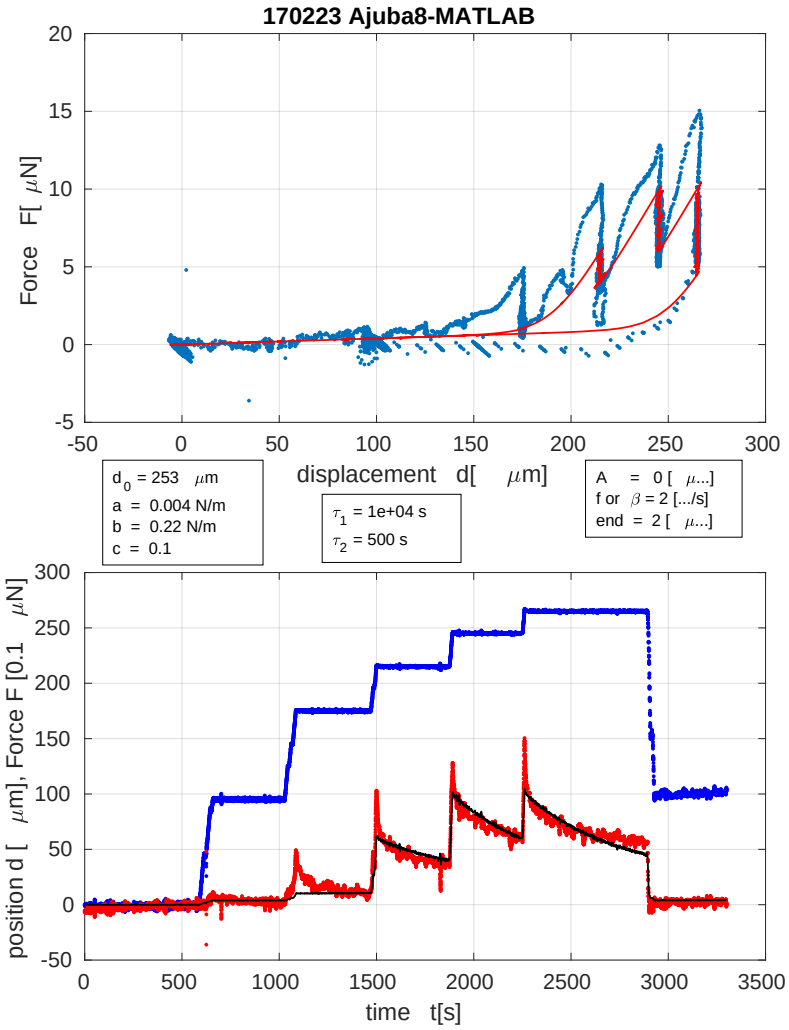
170223 Ajuba8-MATLAB
Force F[μN]
displacement d[μm]
d0 = 253 μm
a = 0.004 N/m
b = 0.22 N/m
c = 0.1
τ1 = 1e+04 s
τ2 = 500 s
A = 0 [μ...]
f or β = 2 [.../s]
end = 2 [μ...]
position d [μm], Force F [0.1 μN]
time t[s]

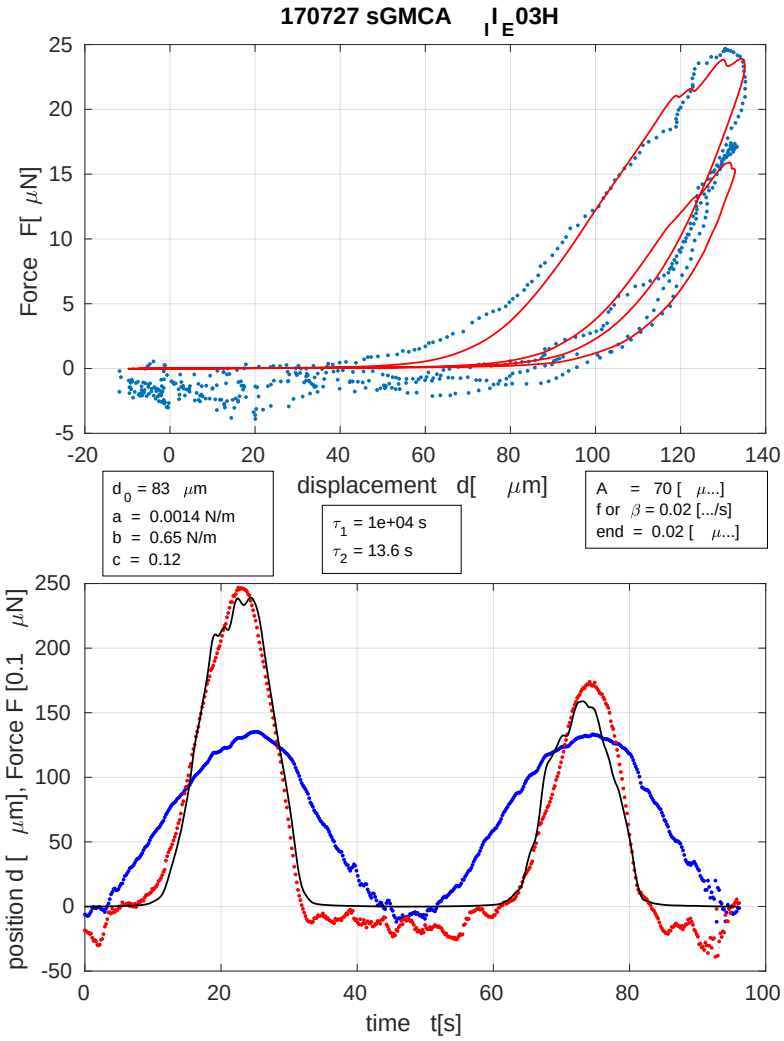
170727 sGMCA I E 03H
Force F[μN]
displacement d[μm]
d 0 = 83 μm
a = 0.0014 N/m
b = 0.65 N/m
c = 0.12
τ 1 = 1e+04 s
τ 2 = 13.6 s
A = 70 [μ...]
f or β = 0.02 [.../s]
end = 0.02 [μ...]
position d [μm], Force F [0.1 μN]
time t[s]

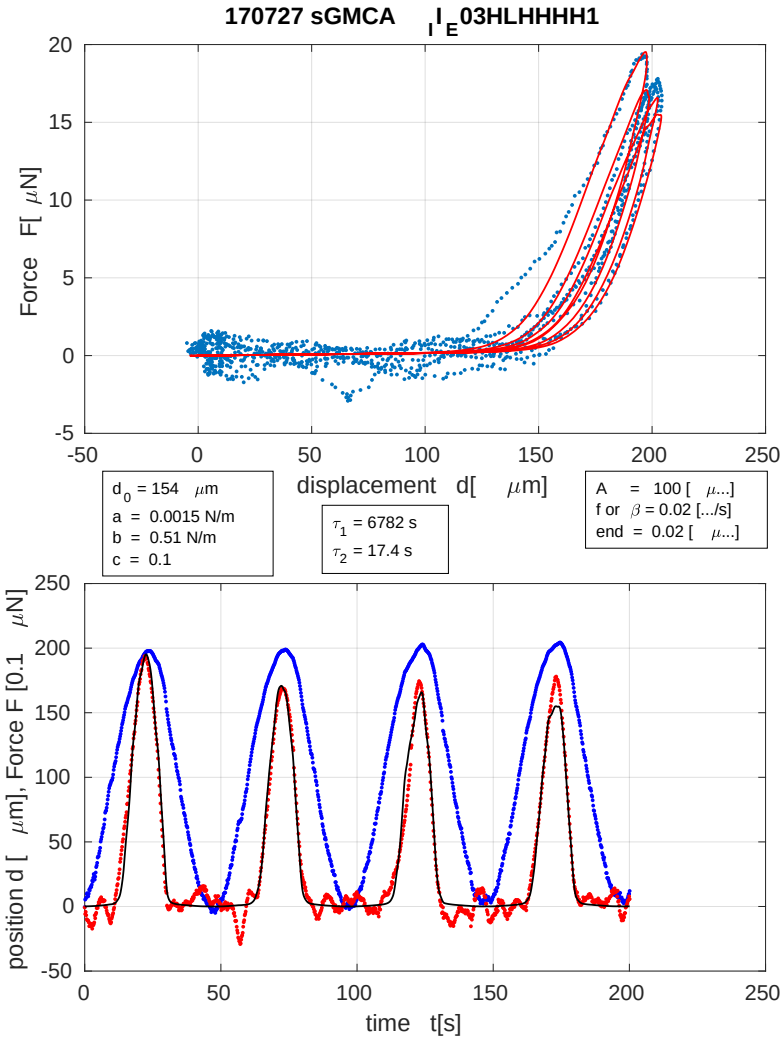
170727 sGMCA I E 03HLHHHH1
Force F[μN]
displacement d[μm]
d 0 = 154 μm
a = 0.0015 N/m
b = 0.51 N/m
c = 0.1
τ 1 = 6782 s
τ 2 = 17.4 s
A = 100 [μ...]
f or β = 0.02 [.../s]
end = 0.02 [μ...]
position d [μm], Force F [0.1 μN]
time t[s]

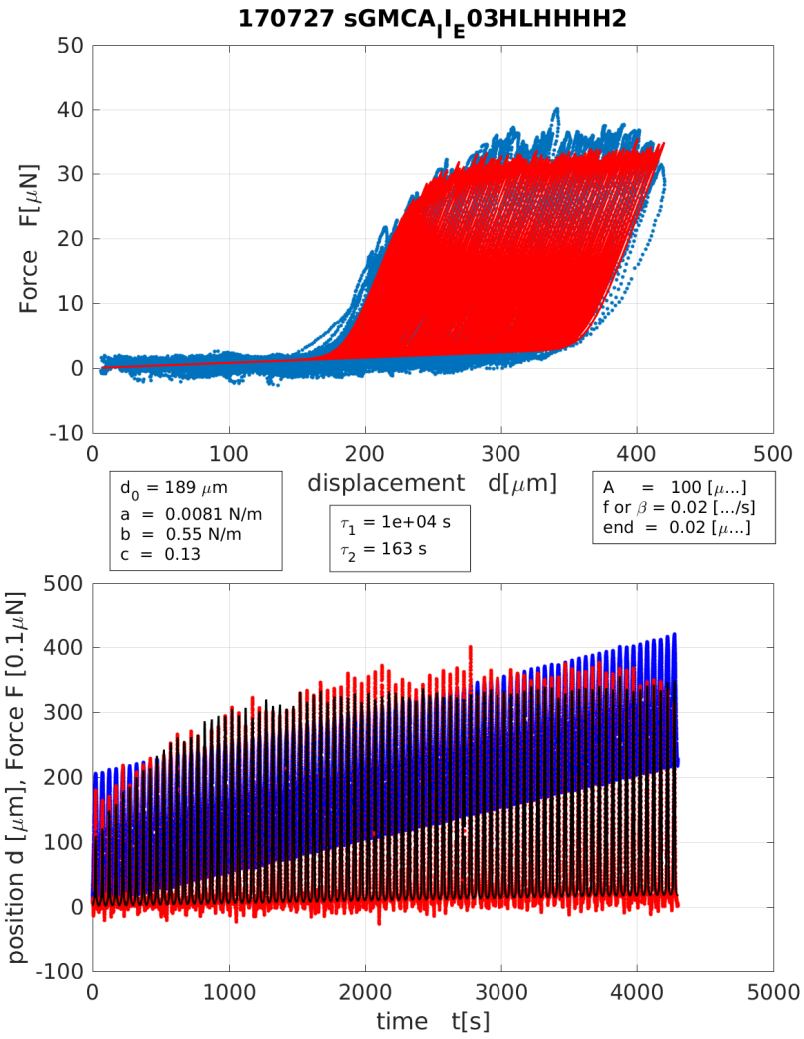
170727 sGMCA_I_E03HLHHHH2
Force F[μN]
displacement d[μm]
d0 = 189 μm
a = 0.0081 N/m
b = 0.55 N/m
c = 0.13
τ1 = 1e+04 s
τ2 = 163 s
A = 100 [μ...]
f or β = 0.02 [.../s]
end = 0.02 [μ...]
position d [μm], Force F [0.1μN]
time t[s]

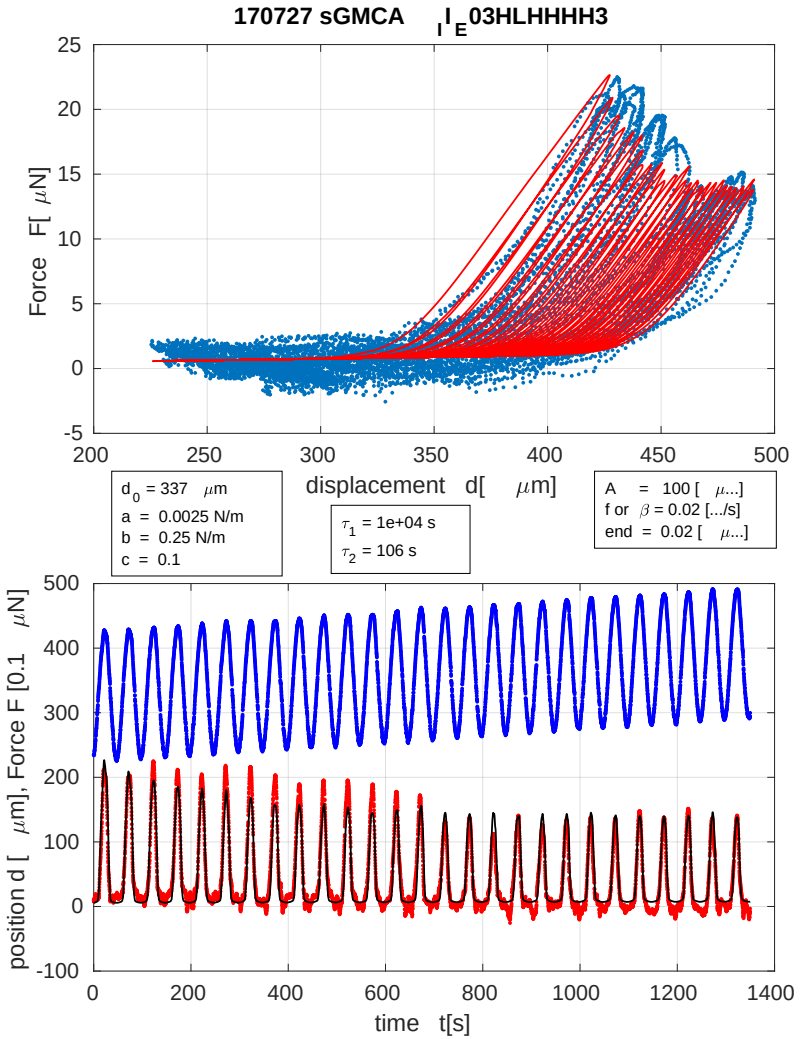
170727 sGMCA _I_E03HLHHHH3
Force F[μN]
displacement d[μm]
d0 = 337 μm
a = 0.0025 N/m
b = 0.25 N/m
c = 0.1
τ1 = 1e+04 s
τ2 = 106 s
A = 100 [μ...]
f or β = 0.02 [.../s]
end = 0.02 [μ...]
position d [μm], Force F [0.1 μN]
time t[s]

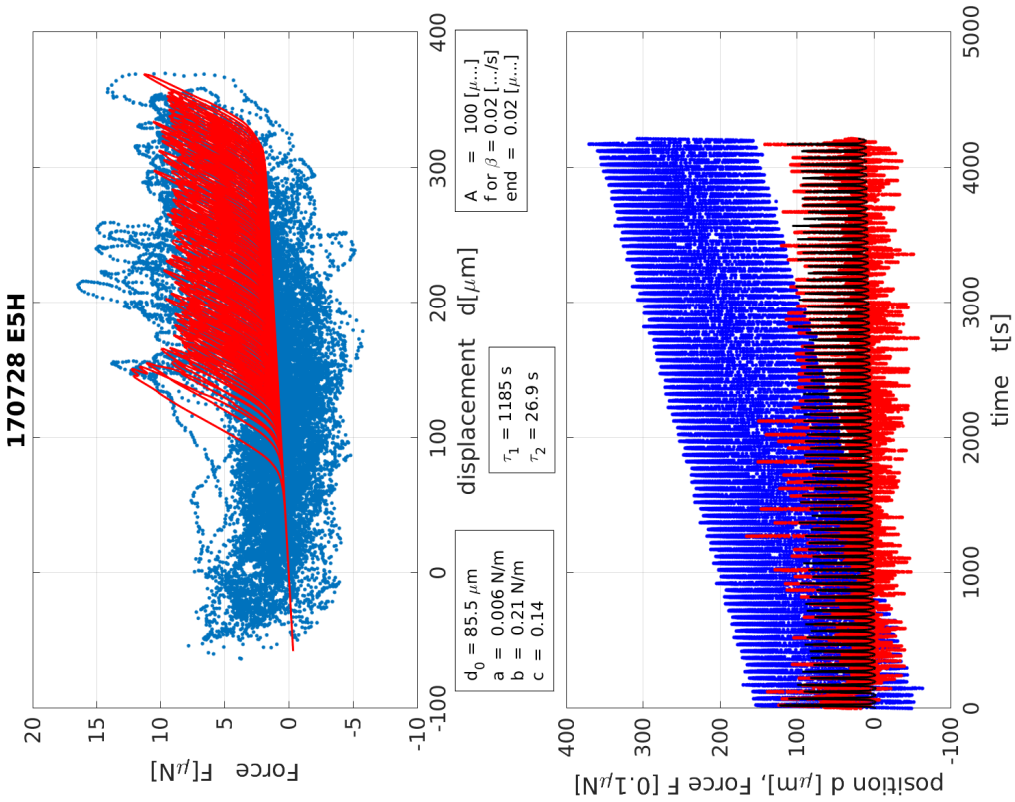
170728 E5H
Force F[μN]
displacement d[μm]
d$_0$ = 85.5 μm
a = 0.006 N/m
b = 0.21 N/m
c = 0.14
τ_1 = 1185 s
τ_2 = 26.9 s
A = 100 [μ...]
f or β = 0.02 [.../s]
end = 0.02 [μ...]
position d [μm], Force F [0.1μN]
time t[s]